Master's Thesis

24 GHz Patch Antenna Array Design for RADAR

Karl Nordin
Sina Shamekhi

Department of Electrical and Information Technology,
Faculty of Engineering, LTH, Lund University, 2016.

24 GHz Patch Antenna Array Design for RADAR

Karl Nordin
Sina Shamekhi

Department of Electrical and Information Technology
Faculty of Engineering, LTH, Lund University
SE-221 00 Lund, Sweden

Advisor:
Buon Kiong Lau

Examiner:
Mats Gustafsson

June 29, 2016

LUND
UNIVERSITY

Printed in Sweden
E-huset, Lund, 2016

Abstract

Radar is a technology that is widely used in many diverse areas; from monitoring space down to ocean surveillance, with many more applications in between. The technology existed before, but was mainly developed in secret by several nations during World War II. Radar technology uses radio waves to detect various kinds of objects and can determine their range, velocity and orientation. It is, therefore, an very attractive technology to be used for surveillance applications.

The main goal with the thesis is to create a non-expensive, fast and efficient people detecting device that can be used for surveillance applications. The device should be able to detect the position of people in the area under surveillance. The motivation for using radar technology is that it is unaffected by poor weather conditions or low visibility, unlike visual based surveillance systems.

Three different configurations of 24 GHz Frequency-Modulated Continuous Wave (FMCW) patch antenna arrays were designed, manufactured and tested with an existing radar. Different signal processing algorithms, so called Direction-of-Arrival (DOA) methods, were also implemented in order to process the data from the radar. The antenna array configurations showed good results, with one of them showing a more robust performance overall.

Keywords:

Direction-of-Arrival (DOA), Frequency-Modulated Continuous Wave (FMCW), Patch Antenna Array, Radar

Acknowledgments

We would like to express our gratitude for all the people that have been involved in helping and supporting us during the work of this thesis:

Our supervisor, Professor Buon Kiong Lau at the Faculty of Enginnering, LTH, for his valuable and wise reflections, which have been very helpful for finishing this work.

Our examiner, Professor Mats Gustafsson at the Faculty of Enginnering, LTH, for all his helpful comments.

Alexander Bondarik, PhD student at the Faculty of Enginnering, LTH, for helping us with the simulation software and the S-parameter measurements.

Our industrial supervisor Carl-Axel Alm for his encouragements throughout the whole project and for giving us valuable and helpful insights, which we needed and appreciate very much.

Johan Wennersten, for helping us implementing the algorithms and providing with valuable knowledge.

Last but not least, the whole PCNI team for making our stay very enjoyable and making us feel welcome. Thank you!

Lund, June 29, 2016
Karl Nordin & Sina Shamekhi

Table of Contents

List of Figures

List of Tables

Chapter 1
Introduction

RAdio **D**etection **A**nd **R**anging (RADAR) [4] is a technology that is used in numerous diverse applications, such as air traffic control, meteorological monitoring, astronomy, ocean surveillance, guided missile target location systems, automotive safety and many more. It is used to detect various kind of objects and has the ability to determine their range, velocity and orientation.

The earliest significant achievements in radar technology were made during World War II along with many other technological advancements. This is also where the term "radar" was coined by two U.S. Navy officers Samuel M. Tucker and F.R. Furth in 1940. Radar technology has since then grown fast and is today not exclusive to the military but also used in commercial applications such as weather monitoring, traffic speed control and air traffic control [4].

The simplest form of a radar system is made of a radio transmitter which sends out electromagnetic pulses that bounce off an object and a receiver which collects and processes the reflected waves. The physical aperture that is able to radiate or receive these pulses is called an antenna (see Ch. 3).

Radars can be divided into two different classes [4]:

- Pulsed radars
- Continuous wave (CW) radars

Pulsed radars, which are the most common, transmit a sequence of pulses at a certain frequency. They can use the same antenna for transmitting and receiving the signal by using a transmit/receive (T/R) switch. This kind of radar setup is called a *monostatic radar*. The CW radars transmit a continuous signal and uses separate transmit and receive antennas. This is due to it being difficult to receive a signal with full sensitivity through an antenna while it is transmitting. A radar system which uses separate antennas that are well separated is called a *bistatic radar* [6].

1.1 Background

There are many different applications where a people detecting device could be of interest. One example is various traffic applications, such as counting and detecting people on railroads. Modern surveillance cameras are widely used to

monitor break-ins and prevent crime. However, under some conditions surveillance cameras can have difficulty distinguishing between different objects. This can happen when there is insufficient lighting, poor weather conditions, low visibility or other factors. This is where radar technology can help the camera in detecting objects. By the use of radar technology, the camera can respond to the signals from the radar and attempt to detect an object where it otherwise would not be able to.

1.2 Thesis Goal

The goal of the thesis is to investigate the opportunity of creating a non-expensive, fast and efficient people detecting device with the help of radar technology. Different designs of state-of-the-art 24 GHz Frequency-Modulated Continuous Wave (FMCW) patch antenna arrays will be designed and thereafter their properties and performance will be investigated. The specific objective is to design the device to simultaneously detect the position of one or more persons.

Can the radar can be precise enough to distinguish between human beings and other objects? What happens if the objects are moving? Which design methods are suitable to build a low cost radar system without sacrificing too much in performance? Can more advanced methods using covariance matrix estimation be used to get higher resolution and robust performance? In this work, we will attempt to answer some of these questions.

1.3 Thesis Work Division

This thesis is written by Karl Nordin and Sina Shamekhi for the Department of Electrical and Information Technology at the Faculty of Engineering, LTH, Lund University.

For this thesis report, most of the work was divided between the two authors as follows:

Karl Nordin worked primarily with implementing the different Direction-of-Arrival (DOA) algorithms and wrote all sections concerning this topic as well as part of the design work in Computer Simulation Technology (CST). Furthermore, he wrote the chapters *Software and Hardware Tools*, *Proposal of Antenna Array Design* and *Further Work* as well as the sections about antenna arrays and MIMO technology.

Sina Shamekhi mainly worked with the simulations and designs in the software program and wrote the *Abstract*, *Introduction* and chapters *Theory of Radar* and *Simulation Results of Antenna Array Element*. Furthermore, he wrote the sections about antenna characteristics and propagation aspects.

The two authors have jointly wrote the *Acknowledgments*, the chapters *Measurement Results*, *Discussion* and *Conclusions*, as well as discussed and worked together to improve the language, the flow and the overall structure of the thesis.

1.4 Outline

In Ch. 2 the general theory of radar is explained. Ch. 3 gives an introduction to the theory of antenna and propagation aspects. Ch. 4 goes through different signal processing methods, specifically Direction-of-Arrival (DOA) methods, that are necessary to calculate the direction of the object(s) to be detected relative to the radar. Ch. 5 describes the software and hardware tools that have been used. Ch. 6 shows the proposed setup of antenna arrays and Ch. 7 goes through the design as well as presents the simulation results. The measurement results are presented in Ch. 8 followed by a discussion of the results in Ch. 9. Final thoughts and conclusions are presented in Ch. 10, followed by several suggestions for further work in Ch. 11.

Chapter 2
Theory of Radar

In this chapter general theory of radar technology is presented as well as some information about the different types of radar systems. Sec. 2.1 gives a short introduction to radar technology with Sec. 2.2 presenting the frequency intervals used for radar systems. The pulsed radar is described in Sec. 2.3 and finally Sec. 2.4 describes the continuous wave (CW) radar system.

2.1 Introduction to Radar Technology

RAdio **D**etection **A**nd **R**anging (RADAR) is a system which uses radio waves to detect various objects such as people, aircrafts, vehicles, ships and missiles. The simplest form of a radar system consists of a radio transmitter and a receiver. The transmitter radiates electromagnetic waves with a specific wavelength which are reflected or scattered of objects and then collected by the receiver. In free space the electromagnetic waves travel at the speed of light and by measuring the round-trip time (the time from when an electromagnetic wave is transmitted, reflected or scattered from an object and received), the range to the target can be obtained [4, 6]. This is illustrated in Fig. 2.1, where it can be understood that the range to target is given by [4]

$$R = \frac{c_0 t}{2} \tag{2.1}$$

where c_0 is the speed of light in free space ($3 \cdot 10^8$ m/s) and t is the round-trip time.

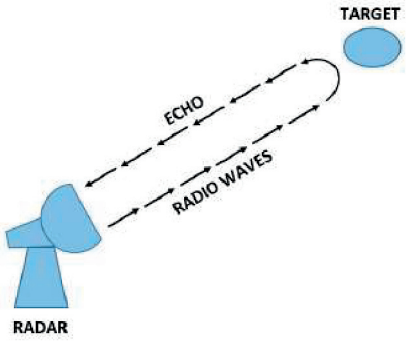

Figure 2.1: The radar transmits radio waves and receives an echo from the target.

2.2 Frequency Bands

Radars operate in a wide interval of frequencies; from 3 MHz up to 300 GHz. The radar frequency interval is usually divided into different sub bands and is presented in Table 2.1

Band	Frequency range	Name
HF	3-30 MHz	High Frequency
VHF	30-300 MHz	Very High Frequency
UHF	300-1000 MHz	Ultra High Frequency
L	1-2 GHz	Long
S	2-4 GHz	Short
C	4-8 GHz	Compromise between X and S bands
X	8-12 GHz	X stands for "cross", as in "crosshairs"
Ku	12-18 GHz	Under K band
K	18-27 GHz	From the German word *Kurz*, which means short
Ka	27-40 GHz	Above K band
V	40-75 GHz	Very short
W	75-110 GHz	W follows V
mm	110-300 GHz	Millimeter wave band

Table 2.1: Radar frequency bands (in some definitions the mm band is classified from 30-300 GHz; therefore, including the V- and W bands and part of the Ka band) [4, 22].

2.3 Pulsed Radar

A pulsed radar system consists of a transmitter T_x that transmits a sequence of pulses, a receiver R_x that amplifies and demodulates the received signals and a duplexer that switches between the transmitter and receiver so that only one antenna is used. The transmitter sends each pulse at the carrier frequency during transmit time, waits for returning echo signals, and then sends out the next pulse. The time from the start of one pulse to the beginning of the next is called the *pulse repetition time PRT*. The number of pulses that are transmitted per second is called the *pulse repetition frequency PRF* and is related to the *PRT* by [4]

$$PRF = \frac{1}{PRT} \tag{2.2}$$

Figure 2.2 shows the transmitted and received pulses. The pulse width is denoted τ_p and the round-trip time t is the time it takes for the pulse to travel the two-way direction between the radar and the target. The distance to target R is then given by (2.1).

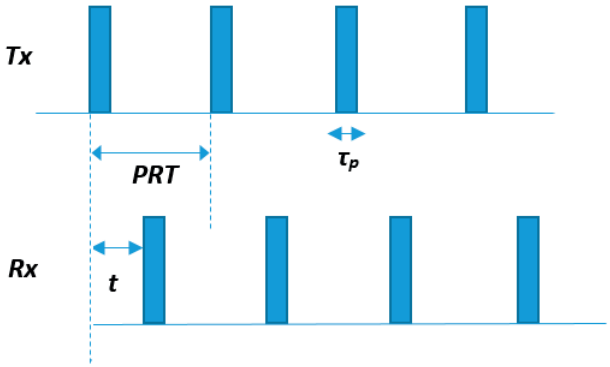

Figure 2.2: Transmit and receive waveform envelopes for a pulsed radar system.

2.3.1 Maximum Unambiguous Range

In pulsed radar systems the echo from a target must be detected before the next transmitted pulse is generated. If the time for the received echo to return from a target is greater than the pulse repetition period *PRT*, then there exists a *range ambiguity* (an uncertainty in measuring range). The *maximum unambiguous range* is defined as [4]

$$R_{amb} = \frac{cPRT}{2} = \frac{c}{2PRF} \tag{2.3}$$

More advanced radar systems can avoid this problem by the use of multiple *PRFs* either on the same single frequency with the *PRT* changing or simultaneously on different frequencies [4].

2.3.2 Range Resolution

The *range resolution* measures how well a pulsed radar distinguishes between two targets, or more, that are close to each other. Two objects close to each other need to be separated with at least half the pulse width in order for the radar to receive two distinct echo signals. The range resolution is given by [22]

$$\Delta R \geq \frac{c\tau_p}{2} \tag{2.4}$$

If the distance between two targets is smaller than the range resolution, then the radar will only see one object [22].

2.3.3 Usable Range

Pulsed radar systems usually use the same antenna for transmitting and receiving signals (for monostatic radar setups). When the system is transmitting a pulse the radar can not receive an echo signal. Therefore, the radar has a *minimal usable range*, blind range, which is the minimum distance the target must have for the radar to be able to detect it. The minimal usable range is given by [22]

$$R_{min} = \frac{c(\tau_p + t_{recovery})}{2} \tag{2.5}$$

where $t_{recovery}$ is the time it takes for the system to switch on the receiver.

If the echo signal from a target arrives at the receiver too close to the next transmit pulse, then it will prevent the entire pulse from entering the receiver before it turns off for the next transmit pulse. The *maximum usable range* at which the target can be located to guarantee that this does not occur is given by (2.6) [4].

$$R_{max} = \frac{c(PRT - \tau_p)}{2} \tag{2.6}$$

2.4 Continuous Wave (CW) Radar

Continuous Wave (CW) radar is a type of radar system where a signal with known frequency is continuously transmitted. It differs from the pulsed radar system by using a continuous signal and separate transmit and receive antennas.

The received echo signal from the object will either have the same frequency as the transmitted signal or be shifted if the object is moving. This change in frequency between the received and transmitted signal is known as the *Doppler effect* [19]. The received frequency f_r is related to the transmitted frequency f_t by [19]

$$f_r = \left(\frac{1 + v/c}{1 - v/c}\right) f_t \tag{2.7}$$

where c is the speed of light and v is the velocity of the moving object (in the direction to or from the transmitter/receiver). The *Doppler frequency* f_d is then given by [19]

$$f_d = f_r - f_t = \frac{2v}{(c-v)} f_t \tag{2.8}$$

Since in most applications $v \ll c$, it is possible to simplify (2.8) to [19]

$$f_d = \frac{2v}{c} f_t = \frac{2v}{\lambda} \tag{2.9}$$

where λ is the wavelength of the signal that is transmitted.

This kind of radars that uses the Doppler effect without any modulation (so called *Doppler radars*) can only detect moving objects, since stationary targets will not cause any Doppler shift. Therefore, it is not possible to determine the range to target; only the velocity of the moving object [19].

2.4.1 Frequency-Modulated Continuous Wave (FMCW) Radar

Frequency-Modulated Continuous Wave (FMCW) radar is a radar system where a transmitted continuous signal with known frequency is varied up and down in frequency over a fixed period of time by a modulating signal. The modulation in frequency will allow for distance measurements along with speed measurements [22].

The difference in frequency between the received and transmitted signal will increase with delay and, therefore, also with distance. The received echo signals from the target are mixed with the transmitted signal, which after demodulation will give the range to target [22]. Figure 2.3 shows a block diagram of a FMCW radar system.

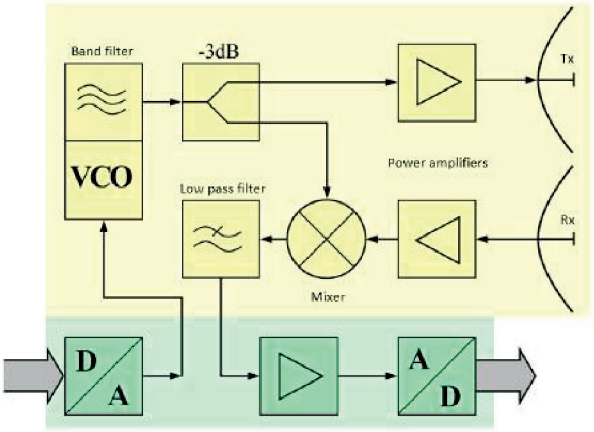

Figure 2.3: Block diagram of a FMCW radar system [22].

The frequency modulation can be achieved with several different modulation patterns, including:

- Triangle wave
- Sawtooth wave
- Square wave
- Sine wave

The basic principle behind the FMCW radar system using a sawtooth modulation is shown in Figure 2.4.

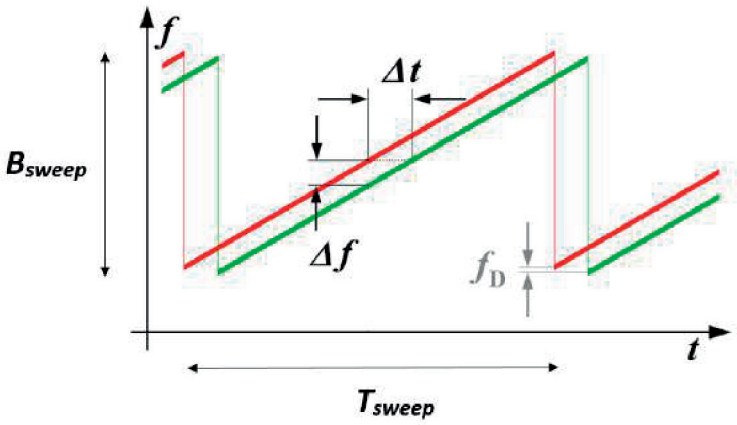

Figure 2.4: FMCW radar ranging with sawtooth modulation [22].

As seen in Figure 2.4, the received signal (the green wave) is a exact copy of the transmitted signal (the red wave) but shifted in time, i.e., to the right in the figure. This results in a frequency difference, called the *beat frequency* Δf, between the two signals which is proportional to the time delay Δt. The time delay is therefore a measure of the range to target. If there is a Doppler frequency f_D present, it will move the entire received signal either up (moving towards the radar) or down (moving away from the radar) in frequency [22].

The distance to target can be obtained from the beat frequency. The slope of the linear ramp in the figure is

$$\frac{df}{dt} = \frac{B_{sweep}}{T_{sweep}} \tag{2.10}$$

where B_{sweep} is the the swept bandwidth and T_{sweep} is the sweep time. Since the beat frequency is proportional to the time delay, the following relation is true

$$\frac{\Delta f}{\Delta t} = \frac{B_{sweep}}{T_{sweep}} \tag{2.11}$$

The time delay is simply $\Delta t = 2R/c$, which gives that the beat frequency is

$$\Delta f = \frac{B_{sweep}}{T_{sweep}} \Delta t = \frac{B_{sweep}}{T_{sweep}} \cdot \frac{2R}{c} \tag{2.12}$$

and the range to target is obtained as [22]

$$R = \frac{cT_{sweep}}{2B_{sweep}} \Delta f \tag{2.13}$$

Using a sawtooth modulation gives the receiver no way of separating between the frequency difference and the Doppler frequency. Therefore, the Doppler frequency will show up as a measurement error in the distance calculation. In many applications this error is negligible [22].

To resolve the Doppler frequency, a modulation pattern with two frequency slopes can be used. The triangle wave modulation is usually a popular choice. The operation of this modulation is shown in Figure 2.5.

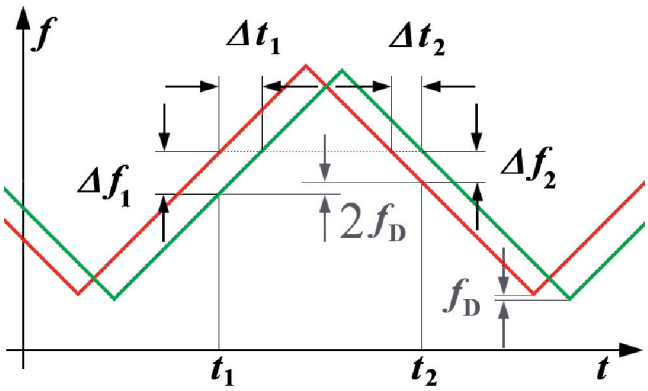

Figure 2.5: FMCW radar ranging with triangular modulation [22].

This modulation pattern gives the possibility of distance measurement on both the rising and on the falling edge of the slope. The radar will measure the Doppler frequency f_D additional to the frequency difference. The frequency difference will provide the distance information, while the Doppler frequency will provide the velocity information. If there would be no Doppler frequency present, the frequency difference during the rising edge Δf_1 would be equal to the frequency difference during the falling edge Δf_2. The radar will either measure the sum or the difference of these two frequencies; depending on the direction of the movement and the direction of the linear modulation [22]. In Figures 2.4 and 2.5, the received echo signal is shifted down in frequency due to a Doppler shift.

The triangular modulation pattern makes it possible to determine the distance more accurately, despite the shift caused by the Doppler frequency. The beat frequency is given by the arithmetic mean of the two frequency differences at the edges of the triangular pattern [22]

$$\Delta f = \frac{\Delta f_1 + \Delta f_2}{2} \tag{2.14}$$

and from Figure 2.5 it is easy to see that the Doppler frequency is [22]

$$f_D = \frac{|\Delta f_1 - \Delta f_2|}{2} \tag{2.15}$$

Using (2.14) in (2.13), the range is obtained as

$$R = \frac{cT_{sweep}}{4B_{sweep}} (\Delta f_1 + \Delta f_2) \tag{2.16}$$

and the velocity of the moving object can be determined from using (2.15) in (2.9)

$$v = \frac{c}{2f_0} f_D = \frac{c}{4f_0} |\Delta f_1 - \Delta f_2| \tag{2.17}$$

where f_0 is the center frequency, i.e., the frequency that lies in the center of the swept bandwidth B_{sweep}.

Another way using only the sawtooth wave is the method of using fast chirps. If the chirps are being sent quick enough, the Doppler frequency will be present as a low frequency on top of each range frequency as described. Since the Doppler frequency is typically much lower than that of the reflected frequency, it will when performing FFT (which is described in Sec. 5.3) stay in the same frequency bin. This can be directly translated as a velocity using (2.17).

Chapter 3

Theory of Antenna and Propagation

This chapter gives an introduction to useful concepts in antenna theory and wave propagation, such as antenna characteristics, radar cross section, antenna arrays, patch antennas and more. The basic characteristics for antennas is described in Sec. 3.1 with Sec. 3.2 describing the propagation aspects. Sec. 3.3 explains how antennas can be coupled together to form antenna arrays, Sec. 3.4 goes through the technique of Multiple-Input Multiple-Output (MIMO) antenna and Sec. 3.5 presents the microstrip patch antenna.

3.1 Antenna Characteristics

An antenna is a device that converts electrical power into electromagnetic waves, and vice versa. They are used to radiate and receive radar signals and come in many different shapes. Figure 3.1 shows one of NASA's big Deep Space Network (DSN) antennas located in Goldstone, California.

Figure 3.1: One of NASA's big Deep Space Network (DSN) antennas located in Goldstone, California [16].

The electromagnetic field around the antenna is generated by connecting an electronic oscillator to the antenna and thereby causing electrons to accelerate. This creates an current that is accelerating back and forth at the frequency of oscillation. Maxwell's equations states that a change in an electric field induces a magnetic field and from this an electromagnetic field is generated [6].

3.1.1 The Far Field and the Near Field

The curvature of the electromagnetic field lines depends on the distance from the antenna. The waves propagate away from the antenna in a spherical shape. The further the waves travel away from the antenna, the more planar they become. The distance R at which the electromagnetic field is considered to be a plane wave is given by [6]

$$R = \frac{2D^2}{\lambda} \tag{3.1}$$

where D is the largest dimension of the antenna and λ is the wavelength of the radio wave. The electromagnetic wave is said to be in the far field when $R \geq 2D^2/\lambda$ and in the near field when $R < 2D^2/\lambda$ [6].

3.1.2 Beamwidth, Gain and Effective Aperture

Antennas can be either directional or omni-directional. For directional antennas, like satellite television dishes, the radiation is focused over a narrow field of view and most of the gain is present in only one direction [6]. Omni-directional antennas radiate in all directions and therefore the gain is not concentrated in one specific direction. Examples of omni-directional antennas are cellular phone antennas, the dipole antenna and AM/FM broadcast antennas [6].

The point at which the main beam gain has dropped 3 dB from maximum gain is called the antenna beamwidth [6]. The half-power beamwidths in the electric and magnetic field planes are denoted Θ_E and Θ_H and the antenna gain for a directional antenna is approximately given by [6]

$$G_{dB} \simeq 10 \log \left(\rho \frac{4\pi}{\Theta_H \Theta_E} \right) \tag{3.2}$$

where ρ is the antenna efficiency and usually $\geq 90\%$.

A cross section of the electromagnetic field is intercepted by the antenna and can be expressed by the effective aperture. The effective aperture is closely related to the antenna gain by [6]

$$A_{eff} = \frac{G\lambda^2}{4\pi} \tag{3.3}$$

where $G = 10^{G_{dB}/10}$. The effective aperture is not a representative of the physical area of an antenna and can be larger in some cases, for example, the dipole antenna [6]. It is often used as a performance parameter for radar systems since it is directly linked to the 3 dB angular resolution $\Delta\theta$ given in (3.4) [6].

$$\Delta\theta = \frac{\lambda}{2A_{eff}} \tag{3.4}$$

3.1.3 Bandwidth and Fractional Bandwidth

The bandwidth of an antenna describes the interval of frequencies over which the antenna radiates or receives energy properly and can be expressed in many different ways.

A very common way to determine if the antenna is *narrowband* or *wideband* is to express the frequency range as a fraction of the center frequency f_c, so called the *fractional bandwidth* FBW and is defined as [3]

$$FBW = \frac{f_h - f_l}{f_c} \tag{3.5}$$

where the center frequency $f_c = (f_l + f_h)/2$ lies between the lower frequency f_l and the higher frequency f_h. The fractional bandwidth is often expressed as a percentage, where the maximum limit is 200 %. Narrowband antennas normally have a FBW of a few percentage, where wideband antennas have a FBW of 20 % or more. Antennas with a FBW higher than 50 % are classified as *ultra-wideband* antennas [3].

3.2 Propagation Aspects

The propagation aspects of the antenna depend on several different factors such as power, gain, efficiency and more. Some of these aspects are described more closely below in the following subsections 3.2.1 - 3.2.4.

3.2.1 Wave Propagation Parameters

The properties of the medium in which the electric and magnetic field lines propagate determines their velocity and the rate at which they form. These properties are determined by the parameters permittivity ϵ, permeability μ and loss tangent σ. Since most radars are used in free space, these parameters become $\epsilon_0 = 8.854 \cdot 10^{-12}$ (F/m), $\mu_0 = 4 \cdot \pi \cdot 10^{-7}$ (H/m) and $\sigma \approx 0$ (S/m). The wave velocity is then given by $1/\sqrt{\epsilon_0\mu_0} \approx c_0$ (m/s) [6].

3.2.2 The Friis Transmission Equation

If the power input for a transmit antenna P_{tx} is known and the distance to a receive antenna is R, then the power transmitted to the receive antenna P_{rx} is given by the Friis transmission equation [6]

$$P_{rx} = P_{tx}G_{tx}G_{rx}\left(\frac{\lambda}{4\pi R}\right)^2 \tag{3.6}$$

where G_{tx} and G_{rx} are the antenna gains for the transmit and receive antennas (assumes matched and polarization matched antennas). The Friis transmission equation can be used to model the performance of radio communication [6].

3.2.3 The Radar Range Equation

The radar range equation is used to measure the performance of a radar system and is given by (3.7) [6]

$$R_{max}^4 = \frac{P_{ave} G_{tx} A_{rx} \rho_{rx} \sigma n E_i(n) e^{(2\alpha R_{max})}}{(4\pi)^2 k T_0 F_n B_n \tau F_r (SNR)_1 L_s} \tag{3.7}$$

where:
R_{max} is the maximum range (m)
P_{ave} is the average transmit power (W)
G_{tx} is the transmit antenna gain
A_{rx} is the receive antenna effective aperture (m^2)
ρ_{rx} is the receive antenna efficiency
σ is the radar cross section of the target (m^2)
n is the number of received pulses integrated
$E_i(n)$ is the integration efficiency
α is the attenuation constant of the propagation medium
k is Boltzmann's constant, $1.38 \cdot 10^{-23}$ J/K
T_0 is the standard temperature, 290 K
F_n is the receiver noise figure
B_n is the system noise bandwidth (Hz)
τ is the pulse width (s)
F_r is the pulse repetition frequency (Hz)
$(SNR)_1$ is the single-pulse signal-to-noise ratio requirement
L_s is the miscellaneous system losses

The average transmit power P_{ave} is related to the duty cycle τF_r of the transmitter by [6]

$$P_{ave} = P_t \tau F_r \tag{3.8}$$

where P_t is the root-mean square power of a single pulse. The receive antenna effective aperture A_{rx} and efficiency ρ_{rx} are related to the receive antenna gain G_{rx} in this equation by [6]

$$A_{rx} \rho_{rx} = \frac{G_{rx} \lambda_0^2}{4\pi} \tag{3.9}$$

where λ_0 is the center wavelength of the system. Impedance mismatch losses, ohmic losses and other losses are all included in the antenna efficiency. For most short-range radar systems used in free space the attenuation constant α is 0, making the term $e^{(2\alpha R_{max})} = 1$ [6].

Two factors determine the single-pulse signal-to-noise ratio $(SNR)_1$: the specified probability of detection P_d and the probability of false alarm P_{fa}. Common values are $P_d = 0.95$ and $P_{fa} = 10^{-6}$, making the $(SNR)_1 = 13.4$ dB [6].

In many cases the gain for the transmit antenna and receive antenna are equal, $G_{tx} = G_{rx} = G$ [6]. Assuming $e^{(2\alpha R_{max})} = 1$ and substituting (3.8) and (3.9) into (3.7), the radar range equation is simplified into

$$R_{max}^4 = \frac{P_t G^2 \lambda_0^2 \sigma n E_i(n)}{(4\pi)^3 k T_0 F_n B_n (SNR)_1 L_s} \tag{3.10}$$

3.2.4 Radar Cross-Section

Radar Cross-Section (RCS), denoted σ, is a measure of how detectable an object is with radar [22]. A large RCS is an indication that the target is easily detectable and a low value makes it more hard to detect. The radar cross-section is defined as [22]

$$\sigma = 4\pi r^2 \left(\frac{S_r}{S_t} \right) \tag{3.11}$$

where S_r is the scattered power density seen at a distance r away from the target and S_t is the power density intercepted by the target. The RCS has the unit of m^2 and is therefore an area. The maximum RCS for a perfectly spherical shape is $\sigma_{max} = \pi r^2$, where r is the radius of the sphere. This shows that the RCS is not equal to the geometric area of the object [22].

There are several variables that affects the RCS but the main two are:

- Size and geometry
- Material

As a general rule, the larger an object is the greater is its RCS. A typical shape with a low RCS is a flat surface or a geometry which minimizes the reflected energy back to the transmitter. For materials, it depends on how much of the received power that is reflected and how much that is absorbed by the target. If a target has a metal surface, it usually has a very high reflection compared to other dielectric materials. Metal objects can also work as mirrors, creating false targets and giving several peak reflections from the signal originating from the same object.

3.3 Antenna Array

Antennas can be coupled together to form an array which can be used to enhance the directional gain. The phase and amplitude can be modulated so that the direction of the resulting beam can be controlled [17]. This means that controlling the amplitude and phase of each element in the array can be equivalent of a mechanically rotating antenna but without the need of moving parts, which can be of benefit and important in our design. Depending on the configuration of the arrays, different characteristics are set. The most common is the Uniform Linear Array (ULA) that has a equidistant grid of antenna elements along a line [17]. This array can also be expanded to a two-dimensional structure with equidistant length, which is called a Uniform Rectangular Array (URA). The URA has one more degree of freedom which makes it possible to control the ϕ- and θ-directions,

compared to the ULA which can only control the θ-direction. Other common configurations use circular/spherical symmetry, but they are disregarded since they are inefficient in using space, which in our case is limited.

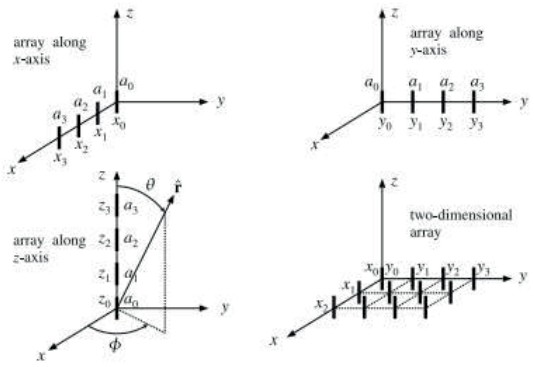

Figure 3.2: Different arrangements of an antenna array [17].

Electronically steering of the array is achieved by proper phase shifts of the signals transmitted by different antennas. In certain directions the phases will add constructively and in other they will add destructively. This is an effect of the Fourier transform; a translation in space corresponds to a rotation of the phase in the frequency domain. The radiation vector $\mathbf{F}$ describes the power density of the radiated far field in the θ- and ϕ-directions for an individual antenna. The total radiation vector containing all contributions for each antenna $\mathbf{F}_{tot}$, can be written as $\mathbf{F}_{tot} = A(\mathbf{k})\mathbf{F}(\mathbf{k})$, where $\mathbf{F}(\mathbf{k})$ is the radiation vector and $A(\mathbf{k})$ is the array factor and is expressed as following in a n-length linear array [17]

$$A(\mathbf{k}) = a_0 e^{j\mathbf{k}\cdot\mathbf{d}_0} + a_1 e^{j\mathbf{k}\cdot\mathbf{d}_1} + a_2 e^{j\mathbf{k}\cdot\mathbf{d}_2} + a_3 e^{j\mathbf{k}\cdot\mathbf{d}_3} + \cdots + a_n e^{j\mathbf{k}\cdot\mathbf{d}_n} \tag{3.12}$$

where $\mathbf{k}$ is the wave number, a_n are the weights for the corresponding element and $\mathbf{d}_n$ is the position of the element. To avoid grating lobes, the distance between the element should be set to be smaller or greater than $\lambda/2$. The pattern of the antenna array factor is only correct when the radiating element is isotropic, which is not the case in real antennas. The total radiation pattern and the total power gain is given by [17]

$$\begin{aligned} U_{tot}(\theta,\phi) &= |A(\theta,\phi)|^2 U(\theta,\phi) \\ G_{tot}(\theta,\phi) &= |A(\theta,\phi)|^2 G(\theta,\phi) \end{aligned} \tag{3.13}$$

where $U(\theta,\phi)$ and $G(\theta,\phi)$ are the radiation pattern and power gain of the radiating element.

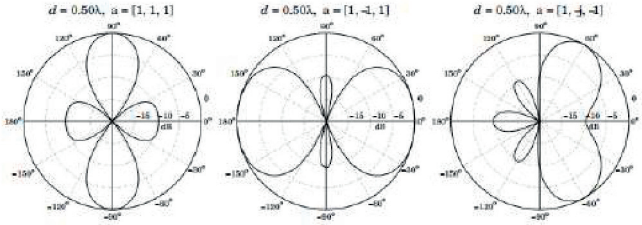

Figure 3.3: Radiation patterns of $\lambda/2$ with different weights a. The radiation that is not in the main lobe is called sides lobes. Broadside corresponds to $90°$ [17].

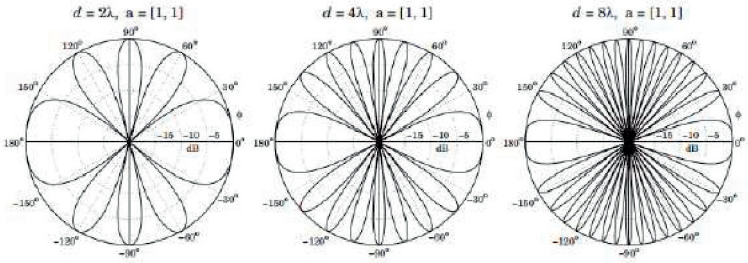

Figure 3.4: Radiation pattern when **d** exceeds the $\lambda/2$ criterion. As expected, several maxima is present in different angels. These maximas are called grating lobes. Broadside corresponds to $90°$ [17].

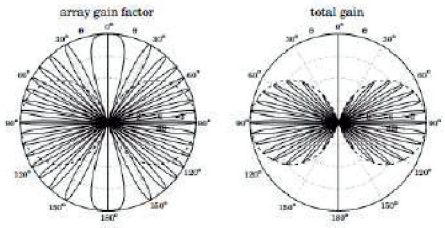

Figure 3.5: This figure shows the implication of the radiating properties of the element to an array factor gain, the dotted line is the gain of a element. This effect can be used to counter the high gain in the grating lobes if a narrow-beam element is used [17].

For ULAs, the array factor in (3.12) has the form of a sinc-function [17]

$$A(\psi) = \frac{\sin\left(\frac{N\psi}{2}\right)}{N\sin\left(\frac{\psi}{2}\right)} \tag{3.14}$$

where $\psi = kd\cos(\phi)$. This array factor is the spatial analog of a low-pass FIR filter in discrete time with a rectangular window function. This is only true if the weights are equal on each element [17].

3.3.1 Antenna Array Synthesis and Design Methods

As described in Sec. 3.3, the amplitude and phase difference between antenna elements give different radiation patterns. As mentioned in the previous section, the method of synthesising the patterns is equivalent to designing FIR filters. It is optimal to have the main beam in the broadside direction to maximize the effective angular resolution given in (3.3). This implies that the phases are the same on each element if a ULA with spacing of $\lambda/2$ is used. The first side lobe levels from (3.14) reach a constant level approximately -13 dB of the main lobe, independent of the number of elements in the ULA. In many applications these gain levels of the side lobes are not acceptable. Since this problem is similar to a rectangular window function, this function can be modified by the use of different weight functions. There exist many different narrow beam low-sidelobe design methods.

The three standard methods other than the uniform weighting is Dolph-Chebyshev, Taylor-one-parameter and binomial distribution [17]. Since the contribution of any other weight will smear out the main lobe, thus making it to become wider. Dolph-Chebyshev weights were chosen since that method will for a given side lobe level create the narrowest main lobe, which is desirable to reduce the range of the radiation in elevation and to be maximized between $-20°$ to $20°$. This method is constructed using Chebyshev polynomials. The mth Chebyshev polynomial is [17]

$$T_m(x) = \cos(m\arccos(x)) \tag{3.15}$$

The Dolph-Chebyshev array factor is then created by [17]

$$W(\psi) = T_{N=1}(x),\ x = x_0\cos\left(\frac{\psi}{2}\right) \tag{3.16}$$

The level of the side lobes which will be created depends on x_0 and can be determined by [17]

$$x_0 = \cosh\left(\frac{\operatorname{arccosh}(R_a)}{N-1}\right) \tag{3.17}$$

where $R_a = W_{main}/W_{sidelobe}$ is the ratio between the height of the main lobe relative to the side lobes in absolute value. The broadening of the main beam can be expressed as [17]

$$\Delta\phi_{3dB} = \frac{50.76°\lambda}{\sin\phi_0 Nd}b,\ 0° < \phi_0 < 180° \tag{3.18}$$

where b is the broadening factor, which is 1 for a uniform weight array and for a Dolph-Chebyshev array it is expressed as [17]

$$b = \frac{6(R+12)}{155} \tag{3.19}$$

where $R = 20log_{10}(R_a)$.

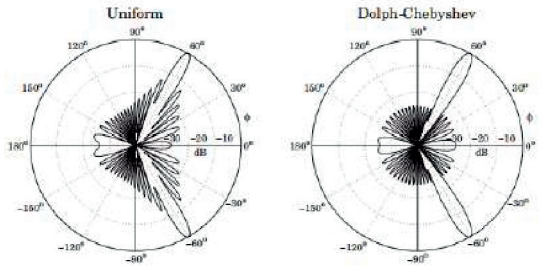

Figure 3.6: This figure shows the difference between uniform and Dolph-Chebyshev weights in a 21 element linear array. The acceptable side lobe level is set to -30dB. The difference between the nearest sidelobe is clearly visible [17].

3.4 MIMO

Multiple-Input Multiple-Output (MIMO) is a new technique of using antennas where there are more than one antenna used simultaneously at both the transmitter and receiver, and where the transmit antennas can radiate independent signals [15]. The main use of MIMO today is in wireless communication where it has been an essential element in, e.g., 802.11ac (WiFi-standard), HSPA+ (3G), WiMAX (4G) and the more commonly used Long Term Evolution (LTE) (4G) [15]. MIMO is an attractive method in wireless communications because it enhances the system performance by allowing the achievable data rate to grow linear with the number of antennas used. One challenge with using MIMO is to be able to distinguish signals between the different Tx-signals. There are several methods that can be used to implement MIMO such as Space Division Multiple Access (SDMA), Time Division Multiple Access (TDMA) and Code Division Multiple Access (CDMA). Since the frontend used only had support for TDMA, which is the simplest method, this is the one that was used in this thesis work.

These advantages of MIMO can also be exploited in the radar case where more than one transmit and one receive antenna is used; each transmit antenna radiates an arbitrary waveform which is independent of the other transmit antennas [15]. The receiving signal can receive the waveforms and because of the independence of the signal, several output signals can be distinguished from each receive antenna. This means that if the number of transmitting antennas is M and the number of receiving antennas is N, the total number of signals is $M \times N$. This will create what is called a *Virtual array*, which will be further discussed in the next section.

The MIMO setting can be used to increase the spatial resolution by the creation of the virtual array that has a larger aperture than the non-virtual array. The main improvement is the enhanced signal quality, which can be described as an improvement in the signal to interference plus noise (SINR). MIMO radar systems are divided into two different subcategories, bi-static and mono-static, which have been mentioned briefly. In the mono-static case the radar antennas are collocated and thus see the same RCS of the target. For the bi-static case the RCS is not equal from every transmit antenna, which means that they are distributed in a certain pattern. This setup requires more complex data processing as each transmit antenna looks at the target from a different perspective.

The transmitted signal is assumed to be narrowband, i.e., $f_0 \gg BW$ and that the propagation is non-dispersive. Under these conditions, the baseband signal is described by [15]

$$\sum_{m=1}^{M_t} e^{-j2\pi f_0 \tau_m(\theta)} x_m(n) = \mathbf{a}(\theta)^* \mathbf{x}(n), \qquad n = 1, \ldots, N \tag{3.20}$$

where f_0 is the carrier frequency and $\tau_m(\theta)$ is the time needed by the signal emitted via the mth transmit antenna to arrive at the target. *-operator means the conjugate transpose. $\mathbf{a}(\theta)$ denotes the target location parameter for each element and is given by [15]

$$\mathbf{a}(\theta) = [e^{j2\pi f_0 \tau_1(\theta)} \quad e^{j2\pi f_0 \tau_2(\theta)} \quad \cdots \quad e^{j2\pi f_0 \tau_{M_t}(\theta)}]^T \tag{3.21}$$

and

$$\mathbf{x}(n) = [x_1(n) \quad x_2(n) \quad \cdots \quad x_{M_t}(n)]^T \tag{3.22}$$

For the received signal at the mth antenna let [15]

$$\mathbf{y}(n) = [y_1(n) \quad y_2(n) \quad \cdots \quad y_{M_r}(n)]^T, \quad n = 1, \ldots, N \tag{3.23}$$

and let

$$\mathbf{b}(\theta) = [e^{j2\pi f_0 \tilde{\tau_1}(\theta)} \quad e^{j2\pi f_0 \tilde{\tau_2}(\theta)} \quad \cdots \quad e^{j2\pi f_0 \tilde{\tau M_t}(\theta)}]^T \tag{3.24}$$

where $\tilde{\tau_m}(\theta)$ describes the time needed by the reflected signal at θ to arrive at the mth receive antenna.

The received data vector can then be described by the following equation [15]

$$\mathbf{y}(n) = \sum_{k=1}^{K} \beta_k \mathbf{b}^c(\theta_k) \mathbf{a}^*(\theta_k) \mathbf{x}(n) \quad + \quad \epsilon(n), \qquad n = 1, \ldots, N \tag{3.25}$$

where K is the number of targets that reflect the signals back to the radar receiver, β_k are complex amplitudes proportional to the RCS of the targets and θ_k are the location parameters of the target. $\epsilon(n)$ is the interference plus noise term and $(.)^c$ denotes the complex conjugate. The interesting information in the received data vector is the β_k and θ_k for each target k. In simpler words, each target's RCS and its relative orientation in space.

As often described in array signal processing, the assumption that the target is described as a point is in our scenario not a fully valid approximation; each human can provide several points and a walking human is not a uniform moving point object since different body parts such as arms, torso and legs have different relative speeds, which can induce errors in a simplistic target model. The characteristic signature of a walking human could also be exploited to confirm that a target is human by analyzing the Doppler spectrum to identify these different speeds, which are characteristics of a walking human [15].

3.4.1 Virtual Array

The MIMO concept says that a received data vector is $M_T \times M_R$ large. This data matrix can be interpreted, as mentioned before, as a virtual array. This virtual array is created by a convolution between the receiving antenna arrays and the transmitting array. The received signal can be expressed as following for each sampling point

$$\mathbf{z}(t) = \sum_{\delta} \mathbf{H}(\delta)\mathbf{s}(t-\delta) \quad + \quad \epsilon(n) \tag{3.26}$$

where $\mathbf{H}(\delta)$ is the delay for each antenna element, The summation in (3.26) is over the delays δ, which correspond to different range cells. In the far field the delay has the following structure

$$\mathbf{H}_{m,n} \propto e^{i\mathbf{k}\cdot(\mathbf{y}_n+\mathbf{x}_m)} \tag{3.27}$$

where $\mathbf{k}$ is the wave vector and $\mathbf{y}_n, \mathbf{x}_m$ are the positions of the transmitters and receivers phase centers, respectively. The structure of $\mathbf{H}$ gives more spatial separation than the size of the actual array, the effective aperture is increased which is described by the virtual array. For a ULA the virtual array phase centers can be constructed by convoluting the location of the real transmitter and receiver location. This can be described by the following equation

$$\begin{aligned} \mathbf{vec}(\mathbf{H}) &= \mathbf{a}_R(\mathbf{k}) \otimes \mathbf{a}_T^T(\mathbf{k}) \\ (\mathbf{a}_R)_n &= e^{i\mathbf{k}\mathbf{y}_n} \\ (\mathbf{a}_T)_m &= e^{i\mathbf{k}\mathbf{x}_m} \end{aligned} \tag{3.28}$$

$\mathbf{H}$ represents the antenna aperture and the number of elements is thus increased in size to $M_T \times M_R$ number of elements. The vec()-operator converts the matrix arguments into a vector by stacking rows together, which then can be used by beamformers [15].

An example can easily be constructed, for instance, given by the following linear array when the antennas are using both receive and transmit mode

$$\begin{aligned} Tx \quad array \quad &= \quad \{1 \quad 1 \quad 1 \quad 1\} \\ Rx \quad array \quad &= \quad \{1 \quad 1 \quad 1 \quad 1\} \\ \text{gives} \quad &\text{the} \quad \text{virtual} \quad \text{array} \\ \{1 \quad 2 \quad 3 \quad 4 \quad 3 \quad 2 \quad 1\} \end{aligned} \tag{3.29}$$

This means that the spatial sampling is more than one on several locations and the overall aperture has been increased by 75 %. Since the received data matrix has more than one vector that has the same time delay, this is not optimal in angular resolution which is proportional to the spatial sampling points. The array can easily be changed so that the virtual array is at different spatial locations. A 3 Tx and 3 Rx array could be placed in the following manner to achieve this

$$\begin{array}{rrcl} Tx & array & = & \{1 \quad 1 \quad 1 \quad 0 \quad 0 \quad 0 \quad 0 \quad 0 \quad 0\} \\ Rx & array & = & \{1 \quad 0 \quad 0 \quad 1 \quad 0 \quad 0 \quad 1 \quad 0 \quad 0\} \\ & & & \quad \text{gives} \quad \text{the} \quad \text{virtual} \quad \text{array} \\ & & & \{1 \quad 1 \quad 1 \quad 1 \quad 1 \quad 1 \quad 1 \quad 1 \quad 1\} \end{array} \tag{3.30}$$

This will give a total of $M_T \; x \; M_R \; = \; 9$ element array, which is an increase of the aperture by 300 %. This gives a significant reduction of the beamwidth and greatly enhances the angular resolution. This can easily be converted to an rectangular array by doing the convolution in two directions [15].

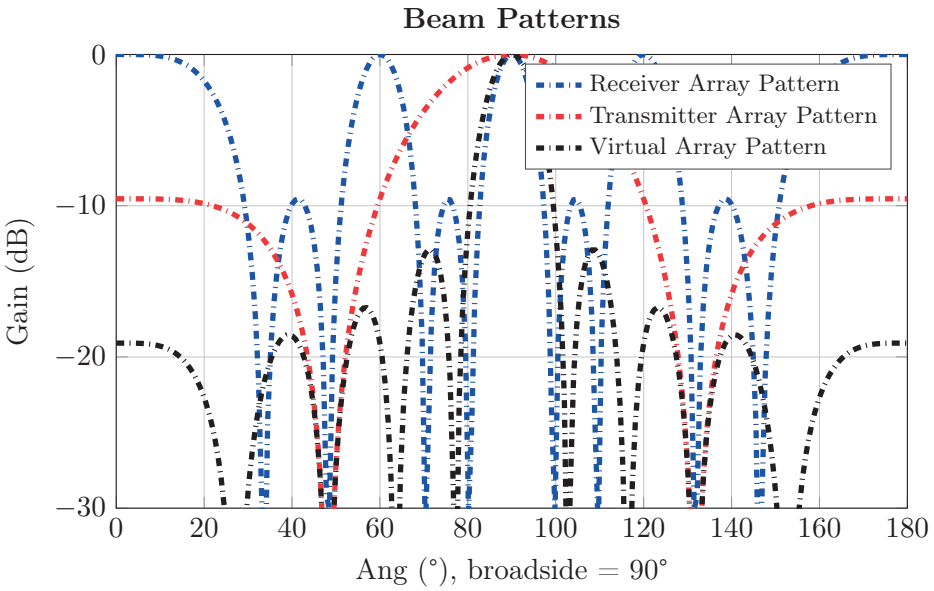

Figure 3.7: The beam pattern of the receiving array, the transmitting array and the virtual array.

3.5 Microstrip Patch Antennas

The most attractive variation of the microstrip antenna is the patch antenna. It consists of an antenna element pattern in metal trace, a "patch" of metal, mounted on top of a dielectric substrate, with a metal layer on the opposite side of the substrate forming the ground plane.

Figure 3.8 shows a rectangular patch antenna with the width W, the length L and the thickness t. The patch lies on top of a substrate with a dielectric constant of ϵ_r and height h. The rectangular geometry is the most common shape used for patch antennas.

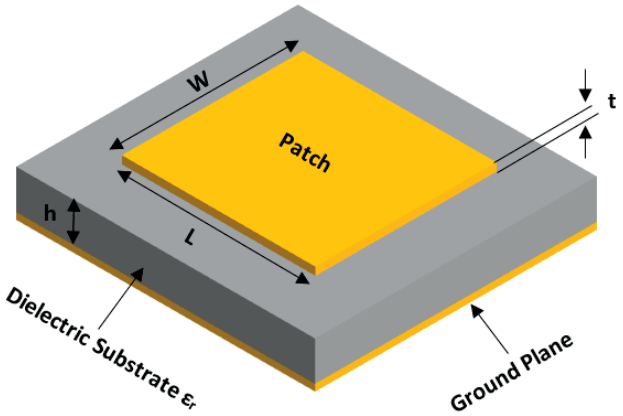

Figure 3.8: A rectangular patch antenna.

The patch antenna is inexpensive to manufacture and its simple physical dimensions makes it easily implementable on a PCB using lithographic manufacturing methods. It is mainly used in the Ultra High Frequency (UHF) band since the size of the patch is directly related to the wavelength. The shape of the patch is very flexible and common ones are square, rectangular, circular and elliptical. These have the advantage of the ability to have polarization diversity, which can be realized by designing the feed structure and patch geometry in different ways. The drawbacks of the patch antenna is low bandwidth, not very good radiation efficiency, low power handling and relatively low gain. However, large arrays of patch antennas can be formed to compensate for the relatively low gain.

There are two approaches for modeling and analyzing the patch antenna:

- Transmission line model
- Cavity model

The interesting region is the one between the patch and the ground plane, which is filled by the dielectric material. This is valid as long as the thickness of the patch is $t \ll \lambda$. This section describes the cavity model for the patch antenna and Maxwell's equation takes this form in the region [9]

$$\begin{aligned} \nabla \times \mathbf{E} &= -j\omega\mu_0\mathbf{H} & \nabla \times \mathbf{H} &= \mathbf{J} + j\omega\epsilon\mathbf{E} \\ \nabla \cdot \mathbf{E} &= 0 & \nabla \cdot \mathbf{H} &= 0 \end{aligned} \tag{3.31}$$

The boundary conditions can be simplified to Perfect Electric Conductor (PEC) on the conductor surfaces and Perfect Magnetic Conductor (PMC) on the four sides of the approximate cavity. The mode responsible for the radiation is the TM^z_{010} [9]. The magnetic currents along the x-axis at $y = 0$ and $y = b$ is responsible for the radiation. The radiation is equivalent as from two magnetic current slots in both the cavity model and the transmission line model. With this model, the total radiation pattern is derived from multiplying the array factor with the electric field.

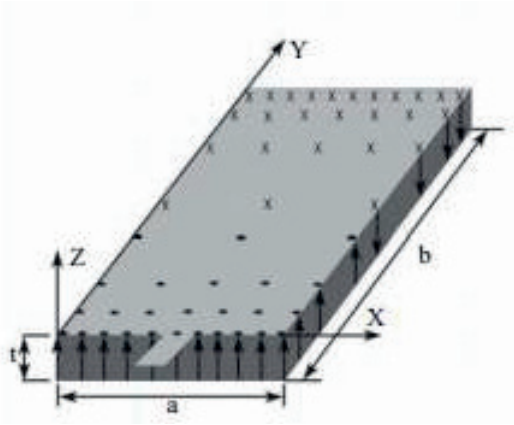

Figure 3.9: This shows the configuration of the electric field in the active TM^z_{010}-mode. a is the width of the patch and b is the length [9].

The EM-field of the resonant TM^z_{010} mode in the cavity is described by [9]

$$\begin{aligned} E_z(x) &= E_0 \sin\left(\frac{\pi x}{L}\right) \\ H_y(x) &= \frac{jE_0}{\eta} \cos\left(\frac{\pi x}{L}\right) \end{aligned} \tag{3.32}$$

where η is the free space impedance.

3.5.1 Input Resistance

Input resistance R_{in} of a patch antenna is estimated from the following at resonance frequency [2]

$$R_{in}(y = y_0) = R_{in}(y = 0) \cos^2\left(\frac{\pi y_0}{L}\right) \tag{3.33}$$

where y_0 is the inset feed distance and $R_{in}(y = 0)$ is the resistance at the edge of the patch.

This is important in the design of the feed network to the patch since to obtain an optimal antenna good matching is required. The resistance in the center, where there is a node in the E-field, is zero and the maximum is at the edge where the theoretical model predicts a resistance going to infinity but in realistic cases the resistance is between $200\ \Omega - 400\ \Omega$. There are several methods of feeding a patch antenna. The simplest are the direct coupled such as microstrip feed and coaxial feeding, which are simple to design. There are also indirect coupling techniques such as proximity or aperture coupled which are exploiting different layers in the PCB [9]. These methods were not considered since they are more difficult to implement.

The normalized input resistance can be plotted as a function of y, as shown in Figure 3.10.

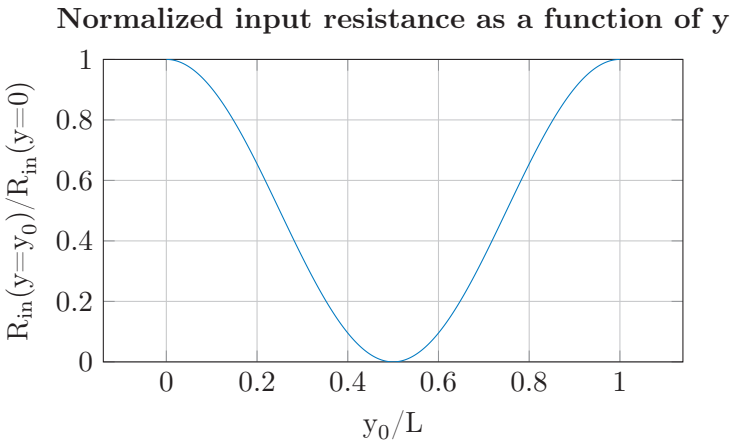

Figure 3.10: Resistance normalized at different y-positions.

Quarter-Wave Impedance Transformer

The impedance of the feed to the patch is usually 50 Ω and since the patch has much higher impedance (if microstrip feed line is used), there is a mismatch in impedance. A very common way to resolve this mismatch is the use of the quarter-wave impedance transformer, which is a component that is exactly one quarter of a wavelength long. It can be a transmission line or a waveguide and is terminated in some known impedance. Figure 3.11 shows a transmission line used as a quarter wave transformer.

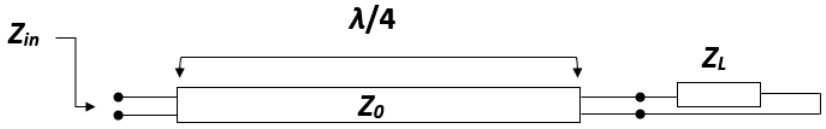

Figure 3.11: A transmission line used as a quarter-wave impedance transformer.

The relation between the input impedance Z_{in}, the characteristic impedance Z_0 and the load impedance Z_L is

$$Z_{in} = \frac{Z_0^2}{Z_L} \tag{3.34}$$

For instance, if the load is 100 Ω and it needs to be matched to a 50 Ω input, then a transmission line with the characteristic impedance of

$$50 = \frac{Z_0^2}{100} \rightarrow Z_0 = \sqrt{50 \cdot 100} \approx 70.71\Omega \tag{3.35}$$

should be used to achieve impedance matching [9].

3.5.2 Guide to Design a Microstrip Fed Patch Antenna

Start by approximating the length of the patch, when using a substrate with the dielectric constant ϵ_r and free space wavelength λ_0, by using the following formula [9]

$$L = \frac{\lambda_0}{\epsilon_r + 1} \tag{3.36}$$

This is a good first guess as long as a thin substrate is used ($d < 0.015\lambda$). A thicker substrate will degrade the efficiency of the patch. There are more complex formulas which are in most cases not necessary since fine tuning is still needed, which is easiest to achieve in a simulation tool. Width can be tapered to suit different needs, but to achieve maximum bandwidth, the width should be approximate 1.5 times the length, W = 1.5L. The thickness of the ground plane and the patch is usually not critically important. Input resistance is affected by changes in width; the impedance increases when the width is decreasing [9].

The other important thing is the impedance matching, which is done by inserting the microstrip on the width of the patch. The closer to the center the patch is fed, the lower impedance is seen, as described in (3.33). This is easiest done in simulations to ensure that good matching has been achieved. An attractive alternative is to use the quarter-wave impedance transformer at the input to decrease the resistance without having to cut too far into the patch [9].

Chapter 4

Range and Direction-of-Arrival Estimation Algorithms

This chapter goes through the different signal processing algorithms, called Direction-of-Arrival (DOA) algorithms, used for calculating the direction of the targets (sources of reflected waves for the transmitted radar signal) relative to where the radar is located. Sec. 4.1 gives an introduction to the Fourier Transform, which is used to obtain information about range and speed from the radar system. Sec. 4.2 presents the concept of the DOA algorithms with Sec. 4.3-4.6 going into further details.

4.1 The Fourier Transform

Fourier transform is one of the fundamental tools of signal processing and is very useful, especially in FMCW-radars where the information about range and speed are obtained from the frequency response. The estimation of target range and speed, and even direction of arrival, can be achieved by performing different Fourier transforms, though other methods are also available. A simple version of baseband data is described by the following model derived from (2.13) and (4.2)

$$s(n) = Ae^{j\left(2\pi\left(\frac{Bn}{N}\right)\frac{2R}{c}\right)} \tag{4.1}$$

where B is the bandwidth, N is the number of samples, R is the range to target and c is the speed of light.

To get the received power from the range R, the Discrete Fourier Transform (DFT) is used since it gives the range and corresponding magnitude directly. The definition of DFT is the following when there are N samples in a sequence of complex numbers [21]

$$X_k = \sum_{n=0}^{N-1} x_n e^{\frac{-2\pi jkn}{N}} \tag{4.2}$$

The algorithm used for the Fourier transform is the Fast Fourier Transform (FFT). The main reason is that it reduces the complexity of DFT from $O(N^2)$ to $O(N\log(N))$, where N is the data size. It is considered by many as one of the most important numerical algorithms [21]. When performing FFT, one will get N

data points (in frequency domain) that are uniformly distributed between 0 and $Fs/2$, where Fs is the sample rate.

The range resolution is given by the relation $c/2B$, where B is the bandwidth that can at maximum be 250 MHz by legal reasons [13] for the center frequency of 24 GHz and this corresponds to a resolution in range of 0.6 meters. This is a fundamental limit as long as no more bandwidth can be used. Several techniques can be applied to improve the performance of the FFT. The ones that are used include the addition of a window function and zero padding the data.

Window functions are frequently used when using DFT. Since the sampled data in time has to be of finite length, the abrupt edges gives rise to leakage to neighboring frequencies. The rectangular window, which is basically the same as using no window, gives the smallest mainlobe, but at the expense of introducing noise in the neighboring frequency channels. Since the dynamic range of radar is large, the presence of a strong signal will make signals with less power, especially those from farther away, to be appear below the noise level of the strong signal. This trade off is very similar to the one experienced when synthesizing antenna array patterns since the basic mathematics is the same. For high attenuation of spectral leakage to the neighboring frequency bins, the trick is to shape the time samples with non-rectangular windows, as can be seen in Figures 4.2 and 4.3. This is necessary to detect weak radar hits in the presence of, e.g., a jammer or a interferer [21].

The windows which have good sidelobe level attenuation are the Hanning or Chebyshev windows [11]. Chebyshev, gives as mentioned in Sec. 3.3.1, the lowest closest sidelobe level. Hanning gives not as good attenuation to the closest sidelobe but has the advantage that the sidelobe level will attenuate monotonically away from the mainlobe, which is not the case for the Chebyshev window. Figures 4.1-4.3 show the effect of the windows on a sinusoidal signal.

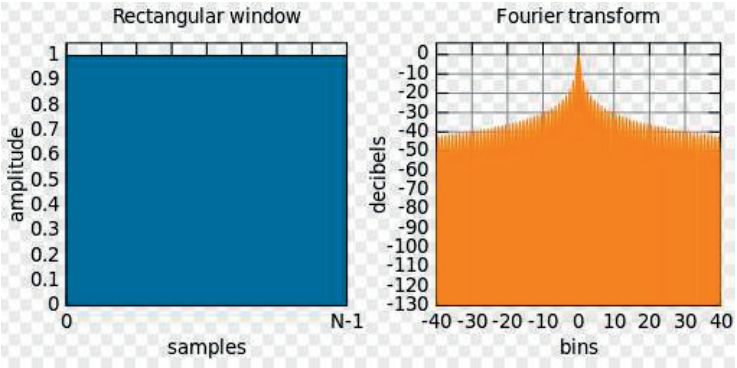

Figure 4.1: The frequency spectrum of a rectangular window [11].

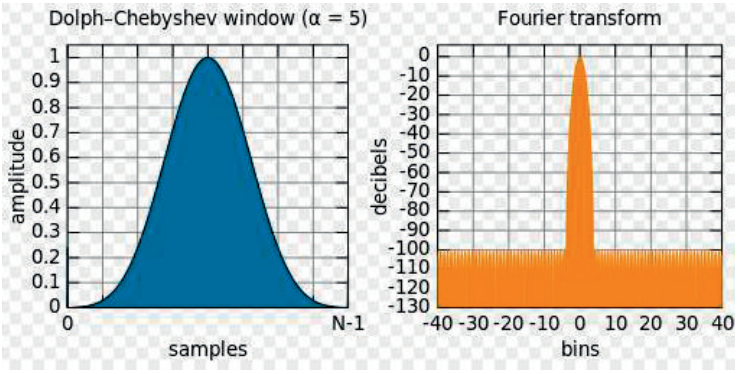

Figure 4.2: The frequency spectrum of a Chebyshev window, side lobe attenuation is set to 100 dB [11].

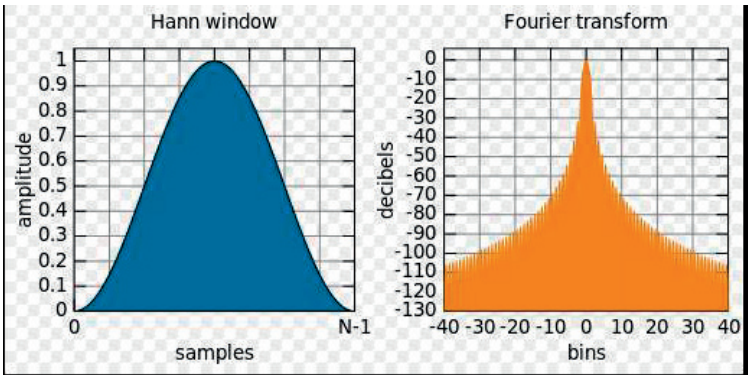

Figure 4.3: The frequency spectrum of the Hanning window [11].

Another important method when performing FFT is zero-padding. This is to add a long series of samples with zero after the received signal. This results in an increase in the amount of frequency bins produced by the FFT. The sinc-interpolation on the signal will give higher accuracy, but the resolution of the FFT is unchanged, as the frequencies between the bins cannot be distinguished. The peak frequency of the signal is more likely to get into the right bin. It often also makes the FFT more efficient because of performing FFT on a sequence with 2^n points will speed up FFT computation, since efficient FFT algorithms for those lengths exist.

4.2 Introduction to Direction-of-Arrival Algorithms

The antenna array receives signals from all directions, but a signal from a given direction will arrive at each array element at a different time, which depends on the element positions. Conventional phased arrays process most of the directional information in radiofrequency (RF) using different amplitude and phase weighting

components such as MEMS phase shifters which are complex to implement. The focus of this thesis work is to implement a simple solution in the RF part of the circuitry in favor of exploiting the digital part. This approach could result in cheaper future systems since the rate of development in the digital domain is much higher than the RF counterpart. Moreover, doing the Direction-of-Arrival processing in the digital domain gives a lot of flexibility, which is not possible in the RF domain, as it is able to suit different needs such as operating in different environments by adapting the algorithms for maximum performance for each environment with the same hardware.

Signal processing has an entire field dedicated to this kind of work, array processing. An array can be defined as a set of sensors, usually sound or electromagnetic, that are spatially separated. The main goals of array processing are to [21]:

- Determine the number and locations of sources (emitters)
- Enhance the SNR
- Track the sources

All of these goals are highly relevant to radar systems since an object is considered an emitter since it reflects the signal that is transmitted by the radar. There is a gap between the idealized mathematical and the physical world and there are five assumptions which are essential for many array processing models, but are hard to achieve [21]:

- Uniform propagation and non-dispersive medium
- Radius of the propagation is much greater that the array size, i.e., plane wave (far field) propagation assumption
- Presence of zero mean white noise and zero signal correlation
- Perfect calibration and no coupling between the sensors
- Narrowband signal assumption

The signal model is usually expressed as (which is identical to (3.25) shown for MIMO-antennas)

$$\mathbf{X} = \mathbf{A}(\theta)\mathbf{S} + \mathbf{N} \tag{4.3}$$

Where:

- $\mathbf{X}$ is the vector of signals received by the array sensors
- $\mathbf{A}$ is the steering vector for each angle of arrival θ
- $\mathbf{S}$ is the signal vector
- $\mathbf{N}$ is the vector containing all the noise

for M snapshots [21].

The simplest case of beamforming uses the same methodology of antenna array design and applies the complex weights as described by (3.12). The basic idea is to create a matrix which sweeps the angle θ in M directions which can be formulated as [7]

$$\mathbf{F} = (\mathbf{F}(\omega_1 \cdots F(\omega_M)) = \begin{pmatrix} 1 & \cdots & 1 \\ e^{j\omega_1} & & e^{j\omega_M} \\ \vdots & \ddots & \vdots \\ e^{j(M-1)\omega_1} & \cdots & e^{j(M-1)\omega_M} \end{pmatrix} \tag{4.4}$$

where ω_n denotes the phase-delay for element M when scanning in the direction θ.

To perform a scan in an arbitrary direction, a steering weight can be multiplied to each antenna element to change the scan direction. The scan direction can be expanded to both azimuth ϕ and elevation θ. Such a scan is equal to how a phased array is steered, but done in the digital domain with the sampled baseband data, both azimuth ϕ and elevation θ. The steering vector is a change of phase of the signal to each element, which is shown in (3.12). For a planar array with elements positioned in the xy-plane, the weight vector w_{nd} can be expressed in terms of the steering vector as [21]

$$w_{nd} = e^{j\mathbf{k}_d \cdot \mathbf{r}_n} = e^{j\frac{2\pi}{\lambda}\sin(\theta_d)(\cos\phi_d x_n + \sin\phi_d y_n)} \tag{4.5}$$

4.3 Array Synthesis Beamformers

The same array design methods and concepts can be used on the digital domain as if it would be implemented in the analog realm using RF components. To look in the angular direction θ, a vector of phase shifts is multiplied to the signal of each individual antenna element which will steer the beam. As the case of designing a phased array, different weight functions can be added to each element as a window function to improve certain aspects.

There are several beamforming methods described in Sec. 3.3.1 and their pros and cons are described. In more general terms, there are two aspects that are in most cases a trade-off one has to choose:

- Mainlobe beamwidth
- Sidelobe levels

For maximum resolution in the mainlobe direction, uniform weights should be used. Uniform weights has its first sidelobe at only -13 dB, which is far too big in most radar scenarios since the dynamic range can be as high as 50 dB [21]. Any change of the amplitude will cause widening of the main beam, but the dynamic range can be increased.

The three synthesis methods which reduces sidelobes, Dolph-Chebyshev, Taylor one-parameter and binomial distributions are briefly described in the following.

Binominal has no sidelobes but a huge main lobe which probably deteriorates the resolution too much with respect to what one can gain. The Taylor one-parameter method is desirable in radar applications due to its decaying sidelobes, because it can be easier to detect signals which can be determined to be false targets appearing in the sidelobes [2]. The difference between Dolph-Chebyshev and Taylor one-parameter is that there is a slightly larger mainlobe beamwidth in the Taylor case with the same level on the closest sidelobe, this effect is shown in Figure 4.4.

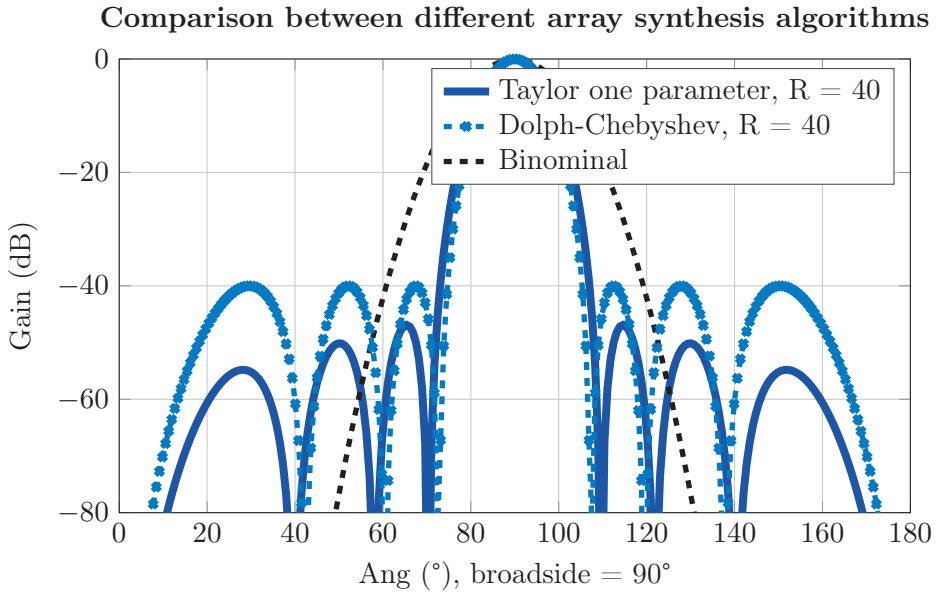

Figure 4.4: Different antenna synthesis filters with a linear array of 8 antennas.

The angular resolution deteriorates the farther the angle is from broadside and above 60° the resolution is restricted. This resolution limit is set by the number of antennas used. By increasing the number of elements in the array, the maximum angle resolvable from the broadside is increased, as described by [2].

4.4 Adaptive Direction-of-Arrival Algorithms

The algorithms described are functions implemented by using techniques from array pattern synthesis. These methods are crude since they do not adapt to the current environment. The main problem that arises is the sidelobes, which will give rise to false targets and create noise in different scan angles that severely degrades the resolution capability in that direction. Array processing has developed methods which adapt the beampattern to the current environment by using the raw data to compute optimal weights for that data. These methods can improve performance and suppress noise that occurs. The different methods can be explained in two major categories [14]:

- Spectral-based techniques
  - Beamforming technique
  - Subspace methods
- Parametric-based techniques
  - Stochastic approach
  - Deterministic approach

Spectral-based techniques use modified spectrum functions of the parameters of interest. The location of the highest separable peaks are noted as the directions of arrival (DOAs). Parametric techniques uses a simultaneous search of all the parameters of interest. This method is usually more accurate but at the expense of an increased computational complexity. This work will only focus on spectral-based techniques since they are easier to implement. The parametric solutions can be simplified if a ULA/URA is used and for these arrays it is possible to create an efficient parametric search [14].

The beamforming techniques discussed in the last section can be expanded to cover adaptive methods, where one of the simplest is Minimum Variance Distortionless Response (MVDR) algorithm, also known as Capon beamformer after its inventor J. Capon. There are several subspace methods such as MUSIC (MUltiple SIgnal Classifaction) and ESPRIT (Estimation of Signal Parameters via Rotational Invariance Techniques). Due to time limitation, only the MUSIC algorithm is evaluated in this work [14].

4.5 Capon/MVDR Beamformer

The conventional beamformer works well when pointing the main beam in the signal direction, which yields the highest peak power in that specific direction. It does not work equally well when having more than one signal, which is almost always the case in radar application due to clutter and several targets. It will find well separated targets with high RCS. Capon beamformer overcomes this by using the available degrees of freedom (DOF) to look a target in the direction and at the same time steer nulls to directions of other targets and clutter. Since the environment to be optimized changes with different scan angles, this method is adaptive. In particular, all the DOFs except one is used to minimize the output power while at the same time the magnitude of the beampattern at the scan angle is maintained. Mathematically, this is expressed as [7]

$$minimize \quad P(\mathbf{w}) \quad subject \quad to \quad \mathbf{w}^H \mathbf{a}(\theta) = 1 \tag{4.6}$$

where $P(\mathbf{w})$ is the output power at the beamformer. Capon beamformer weights are calculated based on the spatial covariance matrix, which is estimated from multiple time samples of the array signal outputs. More details of this matrix is given in the following. The signal model (4.3) contains signal as well as noise. The noise received is in many cases uncorrelated with each other and with this signal,

however, the signals that originate from the same source are correlated. This property can be used to efficiently extract the DOA information. This is done by the concept of cross-covariance information, which is stored in the spatial covariance matrix. The spatial covariance matrix is defined as (4.7), where replacing $\mathbf{x}(t)$ with (4.3) yields the expression on the right hand side of (4.7) [7]

$$\mathbf{R}_{xx} = E\{\mathbf{x}(t)\mathbf{x}^H(t)\} = \mathbf{A}\mathbf{R}_{\mathbf{xx}}\mathbf{A}^H + \sigma_N^2\mathbf{I}_{\mathbf{M}} \tag{4.7}$$

where σ_N^2 is the common variance of the noise. In practice, the exact covariance matrix is hard to estimate, since it has to be estimated with a finite number of data points. The most common estimator of the covariance matrix is the following [7]

$$\mathbf{R}_{xx} \approx \hat{\mathbf{R}} = \frac{1}{N}\sum_{n=1}^{N}\mathbf{x}(t_n)\mathbf{x}^H(t_n) = \frac{1}{N}\mathbf{X}^H\mathbf{X} \tag{4.8}$$

The covariance matrix is fundamental to many DOA-algorithms that are used; the difference is how they extract information from the estimated covariance matrix.

The weight vector for the Capon beamformer is expressed as [7]

$$\mathbf{w}_{Capon} = \frac{\hat{\mathbf{R}}_{xx}^{-1}\mathbf{a}(\theta)}{\mathbf{a}^H(\theta)\hat{\mathbf{R}}_{xx}^{-1}\mathbf{a}(\theta)} \tag{4.9}$$

The term $\mathbf{a}^H(\theta)\hat{\mathbf{R}}_{xx}^{-1}\mathbf{a}(\theta)$ is known as the power spectrum of the Capon beamformer, which is the normalization constant to get the correct power spectrum.

The Capon weights should give an increase in resolution compared with the weights for conventional beamformers. The price to pay is that the inverse of the estimated correlation matrix needs to be calculated [5].

4.6 Subspace Methods

Subspace-based techniques are based on certain properties of the matrix space of $\mathbf{R}_{xx}$ [21]:

- The space, spanned by its eigenvectors, can be divided into two orthogonal subspaces: the signal subspace and the noise subspace
- The steering vectors correspond to the signal subspace
- The noise subspace is spanned by the eigenvectors connected with the smaller eigenvalues of the correlation matrix
- The signal subspace is spanned by the eigenvectors connected with the larger eigenvalues

4.6.1 MUSIC Algorithm

MUSIC is one of the first proposed methods whose sole use is for DOA-estimation, which was discovered by P.O. Schmidt in 1977 [20]. It uses eigenvalue decomposition of the correlation matrix $\mathbf{R}_{xx}$, which assumes the following data model, the same as (4.7), [7]

$$\mathbf{R}_{xx} = \mathbf{A}\mathbf{R}_{xx}\mathbf{A}^H + \sigma_N^2\mathbf{I}_M \tag{4.10}$$

where σ_N^2 is the common variance of the noise and $\mathbf{I}_M$ is the identity matrix of rank M. The assumption is made that the eigenvalues of the correlation matrix satisfies the following relation [7]

$$|\mathbf{R}_{xx} - \lambda_i\mathbf{I}_M| = 0 \tag{4.11}$$

Combining (4.10) and (4.11) gives the following relation, if $\mathbf{A}\mathbf{R}_{xx}\mathbf{A}^H$ has eigenvalues e_i, then they can be expressed as $e_i = \lambda_i - \sigma^2$. The eigenvalues of $\mathbf{A}\mathbf{R}_{xx}\mathbf{A}^H$ have the properties that they are positive semidefinite with rank d (number of signals with the derivation given in [21]). This implies that $M - d$ of the eigenvalues are in the proximity of 0. That means that the $M - d$ of the eigenvalues of $\mathbf{R}_{xx}$ are equal to the noise common variance, which will be the smallest when doing the eigenvalue decomposition. This leads to that the array steering vector $a(\theta)$ is perpendicular to the eigenvectors of the noise subspace. An effect of this is that $\mathbf{a}^H(\theta)\mathbf{V}_n\mathbf{V}_n^H\mathbf{a}(\theta) = 0$, where $\mathbf{V}_n$ contains the $M - d$ noise eigenvectors, arbitrary steering angle θ to the DOA of the incoming signal [7].

The MUSIC spectrum is defined by [7]

$$P_{MUSIC}(\theta) = \frac{1}{\mathbf{a}^H\mathbf{V}_n\mathbf{V}_n^H\mathbf{a}(\theta)} \tag{4.12}$$

The MUSIC algorithm steps can be roughly described as follows [7]:

- Calculate the estimated covariance matrix using (4.8)
- Perform eigendecomposition on $\hat{\mathbf{R}}_{xx}$
- Estimate the multiplicity k of the smallest eigenvalue λ_{min}, then estimate the number of signals as $d = M - k$, where M is the number of eigenvalues found in the estimated covariance matrix $\hat{\mathbf{R}}_{xx}$
- Compute $P_{MUSIC}(\theta)$ using the approximated noise corresponding eigenvectors as $\mathbf{V}_n$
- The d largest peaks in the $P_{MUSIC}(\theta)$ is the DOA estimates of the d incoming signals, since these peaks indicates that these scanned directions are orthogonal to the noise.

Chapter 5
Software and Hardware Tools

In this chapter, the software and hardware tools used in this thesis are described. The chapter begins with Sec. 5.1 giving a short introduction to the software program Computer Simulation Technology Studio Suite (CST Studio Suite), that is used for antenna design and simulations. Thereafter, the frontend used for the radar system, the INRAS Radarbook, is described in Sec. 5.2. The verification of the DOA-Algorithms, mentioned in the previous chapter, is given in Sec. 5.3.

5.1 Computer Simulation Technology (CST)

Computer Simulation Technology Studio Suite (CST Studio Suite) is a high performance software program that offers a wide variety of tools designed for the simulation of 3D electromagnetic fields. It consists of several modules aimed at different areas of applications, including [8]:

- CST MICROWAVE STUDIO (3D EM simulation for high frequency components)
- CST EM STUDIO (simulation of static and low frequency components)
- CST PCB STUDIO (PCBs and packages)
- CST CABLE STUDIO (analysis of cable harnesses)
- CST MPHYSICS STUDIO (thermal and mechanical stress analysis)
- CST PARTICLE STUDIO (simulation of charged particles)
- CST DESIGN STUDIO (system and circuit simulator)

To design and simulate the antennas, CST MICROWAVE STUDIO was used. Firstly, one single patch antenna was designed and it was then used to form a linear array consisting of four patch antennas. Finally, the patch antenna arrays were put together in different configurations to obtain the final design.

5.2 INRAS Radarbook Description

The frontend used for our MIMO radar design is the INRAS Radarbook. It is designed to be a highly flexible and a low cost signal processing and RF product. Its indented primary use is CW radar with the frontend included. The frontend consists of a digital and RF part.

The RF FMCW frontend that operates with the Radarbook consists of two transmit (Tx) and eight receive (Rx) antennas. It can be seen in Figure 5.1, where it is connected to the Radarbook.

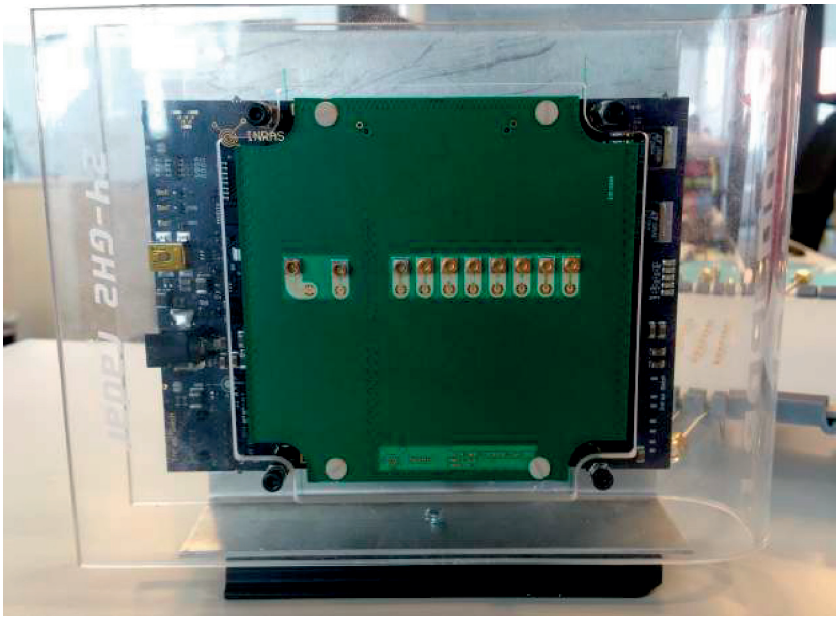

Figure 5.1: The INRAS frontend connected to the Radarbook.

Figure 5.2 shows a block diagram of the overall frontend architecture. The Analog Devices ADF5901 is a 24 GHz Tx Monolithic Microwave Integrated Circuit (MMIC) that consists of a Voltage Controlled Oscillator (VCO) and a 2-channel Power Amplifier (PA) output. The MMIC is connected to the ADF4159, which is a fractional-N frequency synthesizer used to generate the FMCW signal for the transmitter. The Rx channel is provided by ADF5904 combined with an additional Wilkinson divider. The Rx architecture is a 4-channel down-converter. Note that no I-Q channel down-conversion is performed.

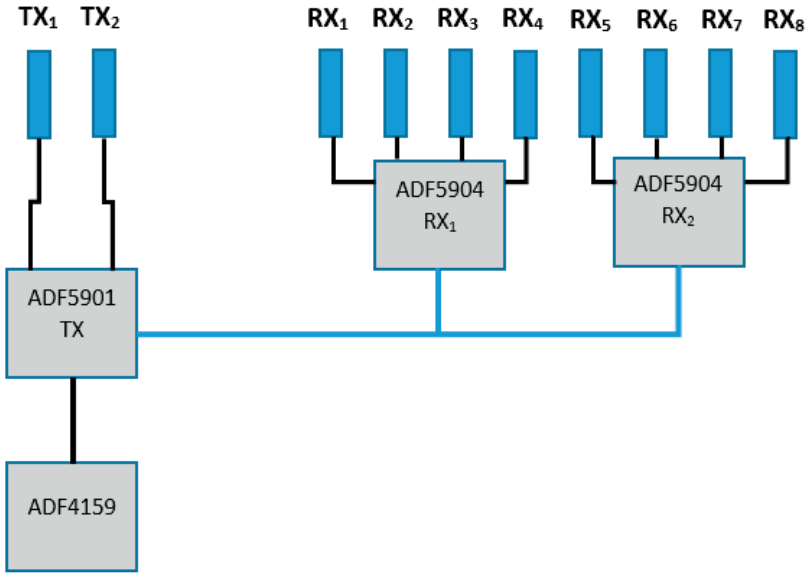

Figure 5.2: Overall frontend architecture.

The baseband block is built with a Cyclone III and a ARM Tegra 2 processor module. The design is made to provide a powerful processing unit suited for the high bandwidth data streams for real-time radar data signal processing. The computer interface is either Ethernet or USB version 3.0. It is connected using Matlab interface and the timing unit is fully programmable [12].

The frequency can be set to sweep between 23.7 GHz and 24.3 GHz. The ramp up time can be set and the number of chirps for range-Doppler processing can be controlled as well. This gives a big degree of freedom to try different configurations. The analog signal processing composes of a 12-bit ADC. The ADC has a maximum sample rate of 80 MSPS and samples the channels sequentially, thus giving each channel a maximum of 20 MSPS for each receive channel. An AAF (Anti-Aliasing Filter) is used before sampling to avoid aliasing frequencies [12].

The FMCW radar can be configured into mainly two setups, depending on if range-Doppler is needed or not. It is programmed for a precise timing between the chirps on each Tx antenna, to ensure no phase differences between each chirp measurement, so that a virtual array can be constructed. The requirement is the same when using the range-Doppler configuration, as precise timing between each chirp is crucial.

5.3 Verification of the Signal Processing Algorithms

The Radarbook receives the data from the Analog-Digital Converter (ADC), which gives the time domain baseband data. Since the ADC is sampling the antennas in a serial format the phase needs to be calibrated to give the correct data. The Radarbook has already been calibrated by INRAS when using their antennas, which fixes the errors that have occurred in the device. The calibrated data contains all the information which is needed to get a picture of the environment. The implementation is described by Figure 5.3 and a flow chart of the data processing is shown in Figure 5.4. Figures 5.5-5.6 show an example of the sampled data in time and frequency domain to give a grasp of the form of the incoming data.

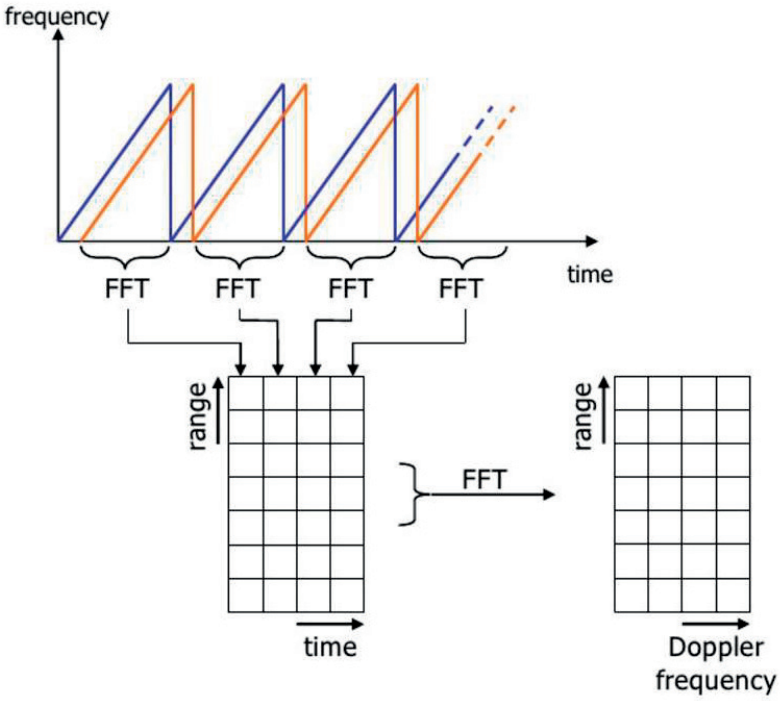

Figure 5.3: A scheme explaining how the Fourier transformers are conducted to get the range and Doppler frequency. These are performed individually by each antenna [18].

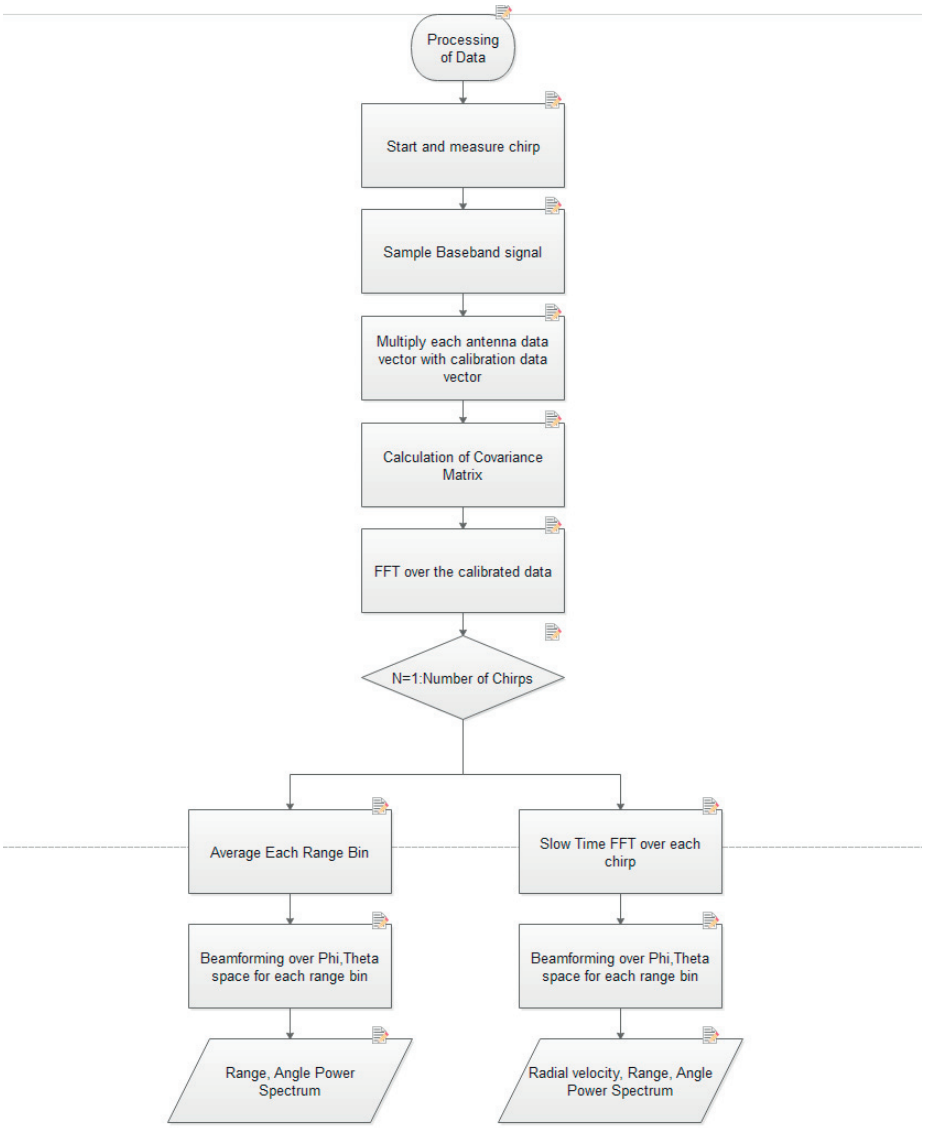

Figure 5.4: Flow chart explaining how the data processing is performed. Reflectivity is calculated by averaging all fast chirps instead of a single slow one.

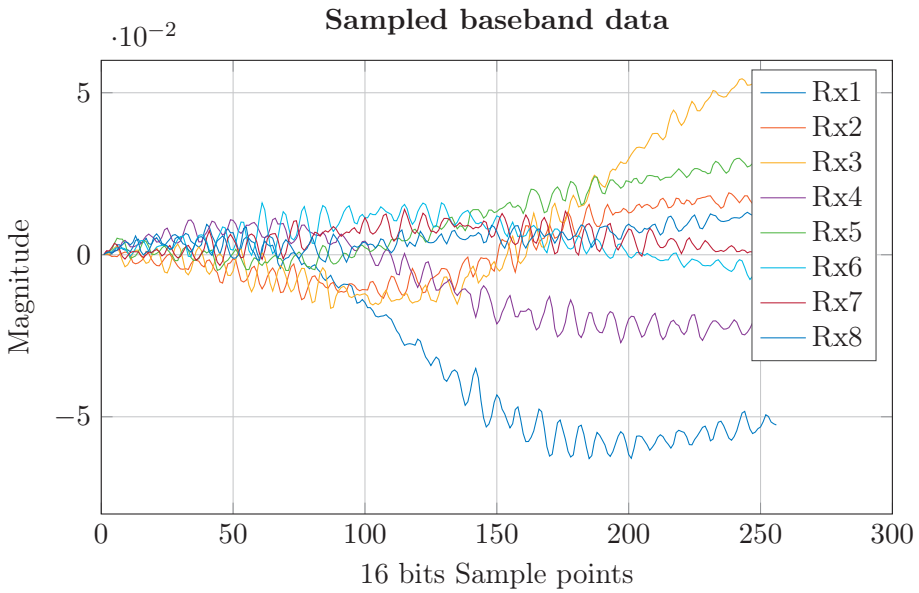

Figure 5.5: The downcoverted baseband signal received by the Radarbook, sampling rate is set to 0.5 MS/s.

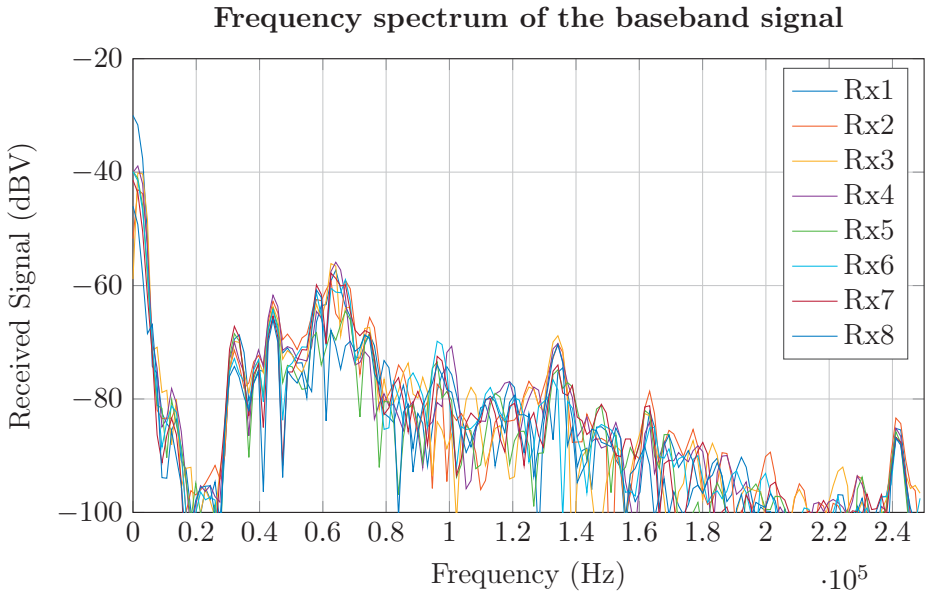

Figure 5.6: The frequency response of the received data using Chebyshev window with 100 dB sidelobe suppression.

As can be seen in Figures 5.5-5.6, the signal has a strong low frequency component, which likely comes from noise generated in the device, i.e., crosstalk and self-mixing. This causes a problem in the estimation of the covariance matrix, which will be biased by this noise component. This low frequency part needs to be filtered out to get a good estimation. However, since the information is processed in the frequency domain, the low frequency component can be easily filtered out.

The frequency of the received signal is directly proportional to the distance, as discussed in the Sec. 2.4.1. The received data is Δf in (2.13). The received power corresponds to the RCS of that particular frequency. A peak in the received signals means that there is a strong reflection at the distance corresponding to that frequency.

To get the angle information of the hit, a DOA-algorithm needs to be implemented at the corresponding frequency. The angular information is stored in the phase difference between the Rx-antennas at the same frequency when applying DOA-algorithms.

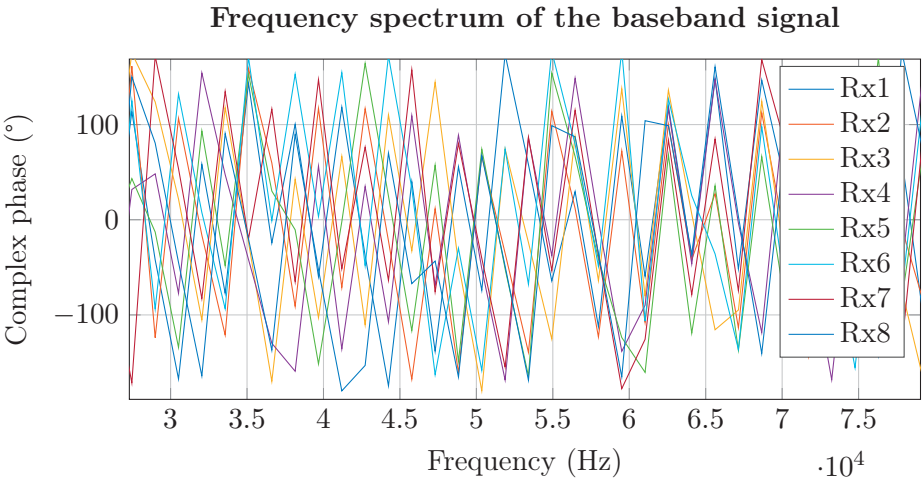

Figure 5.7: The phase of the frequency spectrum.

To get the velocity map of the target, a sample of chirps needs to be compared, the Doppler frequency can be seen as an added frequency on top of the bins. The resolution depends on the amount of chirps processed and the respective timing between the chirps. A big number of chirps will take time to process and during the sampling time, the velocity could have changed or it could have moved to the adjacent frequency bin, which will give wrong results. In practise this gives a trade-off between resolution and the possibility to detect fast moving targets. Since the goal is to measure people, a high resolution of low velocities is preferable since the speed of a walking human is around 1.5 meters per second, which according to (2.17), corresponds to a Doppler frequency of 120 Hz at the center frequency 24 GHz. That means that choosing the correct weight function for the FFT is critical in order to achieve good resolution between slow movements and stationary targets. Doppler shifts of a stationary scene with a Chebyshev 100 dB side lobe level is

shown in Figure 5.8.

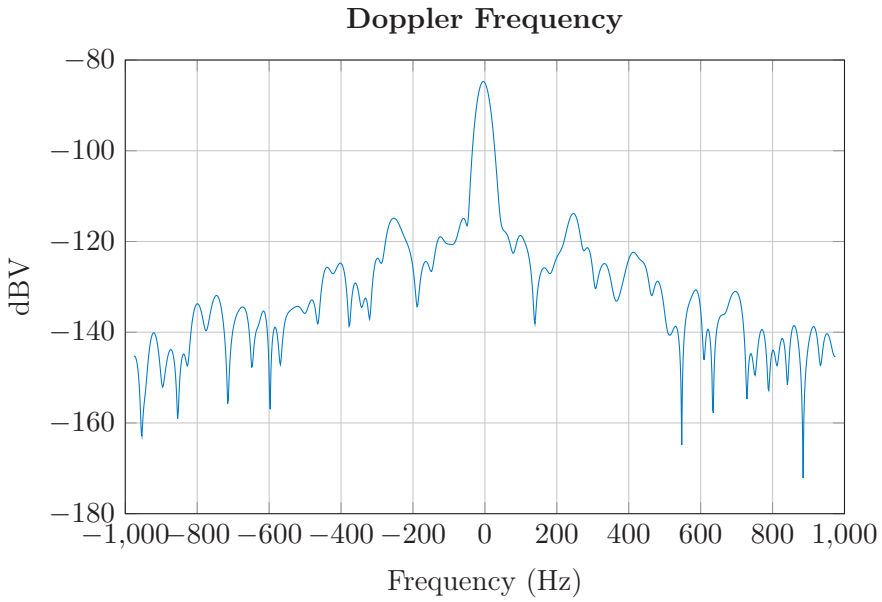

Figure 5.8: The Doppler frequency of a stationary range bin, chirp repetition rate is set to 512 µs and a total of 128 chirps is measured.

5.3.1 Implementation of Direction-of-Arrival Algorithms

The beamformers are implemented in the frequency domain by sweeping the scan direction in the desired (ϕ, θ) angles and creating a grid for each frequency bin. Each grid point represents the total power after the signal from each antenna has been multiplied by a complex delay, described by (4.5), and summed. This is done for each frequency bin to calculate the angular power distribution of that bin. To calculate the range information, the total power of the different range bins needs to be compared. Note that the subspace methods are not considered as beamforming since they calculate the power spectrum based on orthogonality of subspaces and do not provide beamforming weights. The 2D angular grid for a given range bin is shown in Figure 5.9.

Since the interest in this thesis work is to be able to only have a limited scan range in the θ (elevation) direction, the angles of interest are defined to be from approximately -20 to 20 degrees in elevation and 30 to 150 degrees in azimuth. This limitation is imposed as a recommendation as the resolution of the considered arrays outside this 2D angular sector is poor, especially in elevation. This limitation is even worse when it comes to the 4×4 array, since the antenna element spacing is larger and the grating lobes also exist in the azimuth plane. For unambiguous direction estimation in the azimuth, the maximum range is thus limited to 60-120 degrees.

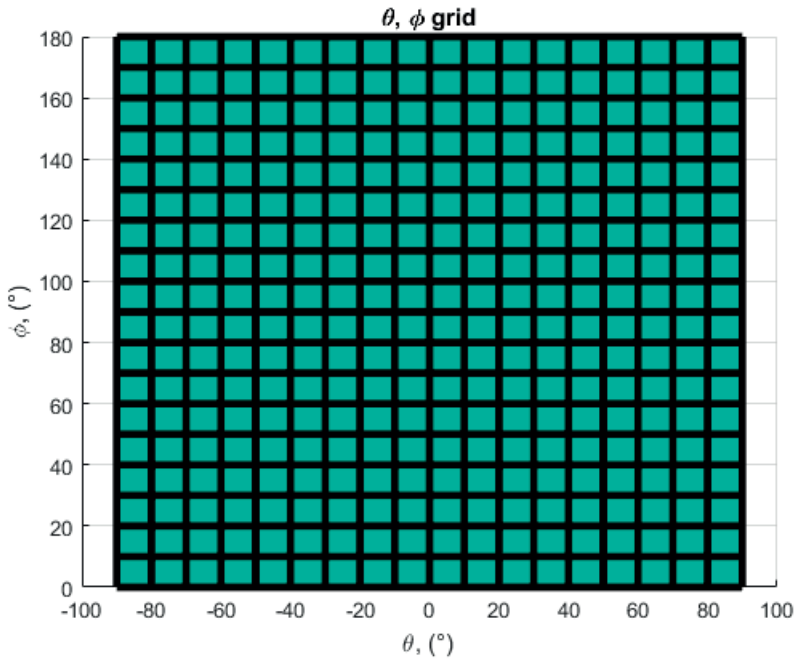

Figure 5.9: Grid representation of the beamforming conducted on the range bin.

5.3.2 Verification of Direction-of-Arrival Algorithms Using INRAS Frontend

To verify the algorithms, tests were conducted on the original INRAS antennas (from Analog Devices). The antenna parameters are shown in Table 5.1 and an illustration of the antennas is shown in Figure 5.10. The INRAS antennas follow an amplitude tapered patch antenna array design which lowers the level of the side lobes in the elevation plane. There is a $\lambda/2$ spacing between the two Tx antenna elements. It was not designed to benefit from MIMO virtual array since the virtual array is not used to create a larger effective aperture, thus only Single-Input Multiple-Output (SIMO) measurements were conducted. Since it is a ULA design, only azimuth DOA could be measured.

A simple case where a reflector was measured in a stationary scene is shown in Figure 5.11. The target is a reflector located 10 meter from the radar with open terrain and a parking lot behind. The azimuth angle of the target is $\phi = 0°$ (broadside direction for the INRAS antenna configuration).

Parameter	Name	Value
G	Realized gain	15.8 dBi
ΔS	Sidelobe suppression	-18 dB
$\Delta\Theta_H$	Horizontal 3 dB beamwidth	76.5°
$\Delta\Theta_V$	Vertical 3 dB beamwidth	12.8°

Table 5.1: INRAS antenna parameters [12].

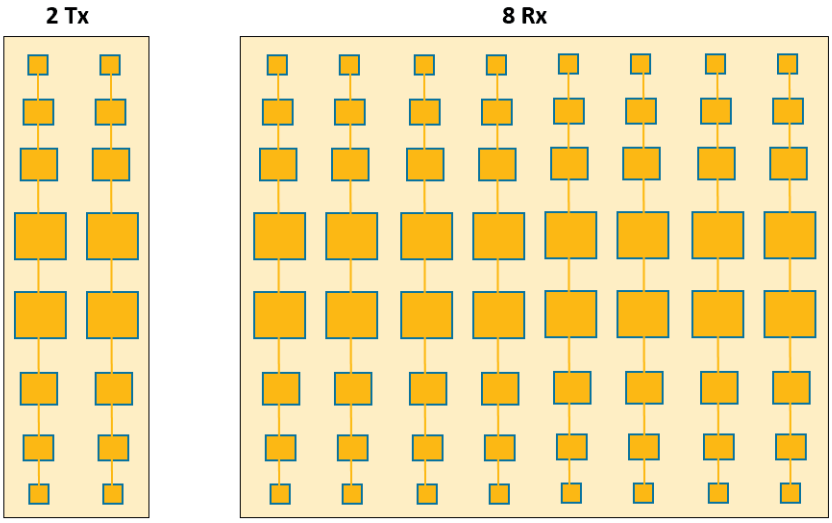

Figure 5.10: Illustration of the INRAS antennas with 2 Tx arrays and 8 Rx arrays. During testing only 1 Tx array element was used.

Figure 5.11: Picture of the area tested with the INRAS antennas. The person in the picture is holding up an octahedral radar reflector.

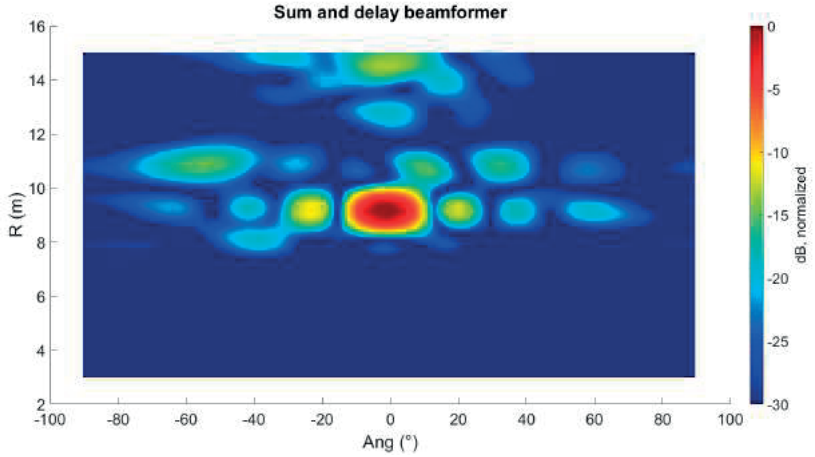

Figure 5.12: Target map with the reflections shown, the received power (in dB scale) is normalized by the strongest hit.

To get a good overview over the performance of the different DOA-algorithms, the range bin that contains the most power was extracted and the power distribution in azimuth angle is plotted for the different methods. The results are summarized in Figures 5.13-5.15. As can be seen in Figure 5.6 and discussed earlier, to get a good estimate of the covariance matrix, the received signal should be filtered by a Butterworth high-pass filter with a cut-off frequency of 50 kHz to suppress the low frequency noise. Based on the number of larger eigenvalues in the covariance matrices, the first 5 eigenvalues were assumed to represent the signal subspace in the MUSIC algorithm.

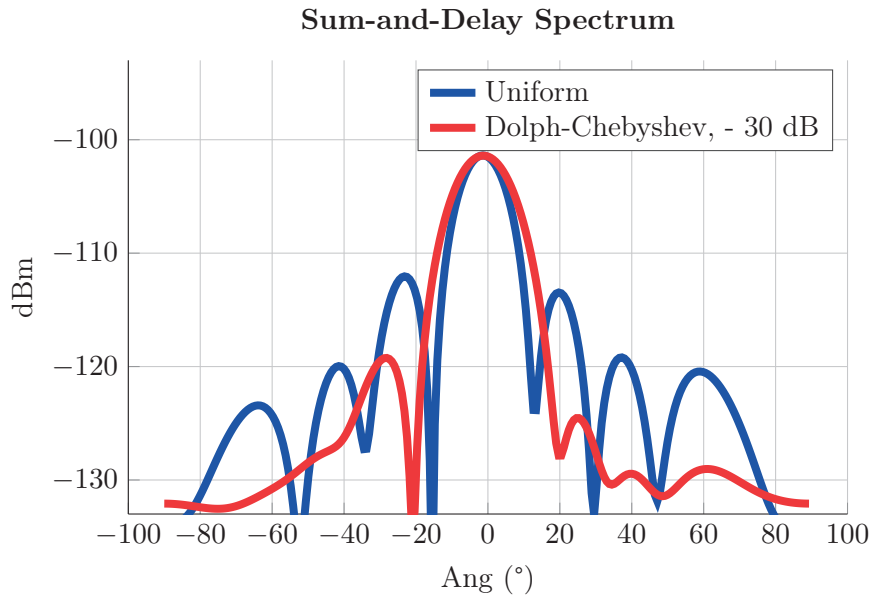

Figure 5.13: The power spectrum for the Sum-and-Delay algorithm.

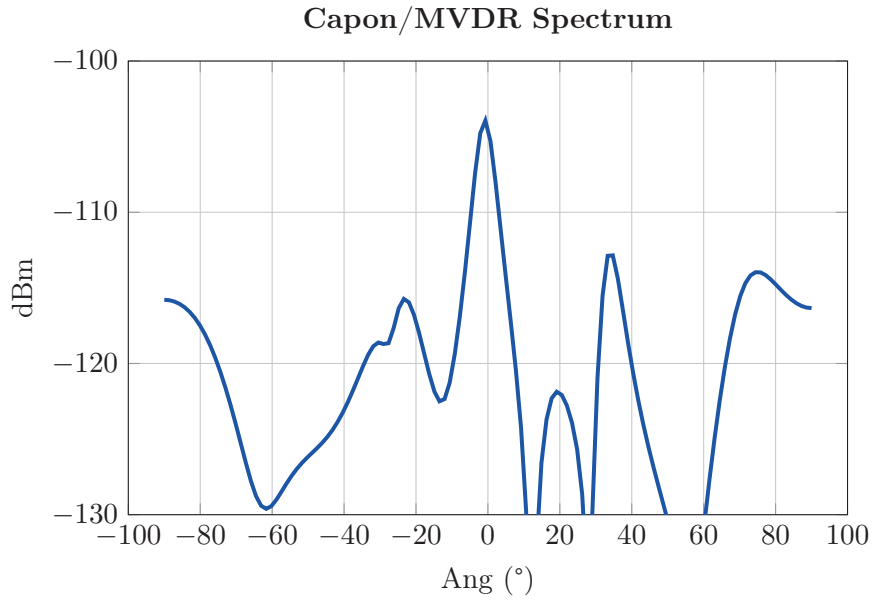

Figure 5.14: The power spectrum for the Capon/MVDR algorithm.

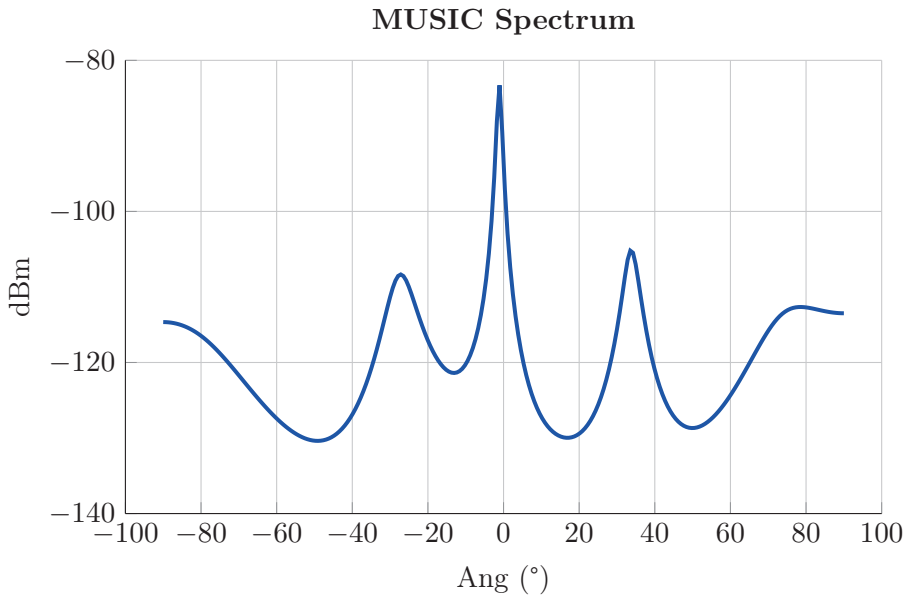

Figure 5.15: The power spectrum for the MUSIC algorithm.

It can be seen from Figures 5.13-5.15 that the algorithms seem to work properly, especially the Sum-and-Delay as it is performing exactly according to theory. The methods using the covariance matrix are harder to verify but they seem to be correctly implemented. There are several correlated signals in the received spectrum, which is one of the reasons that only three of the eight eigenvectors is assumed to be the noise subspace. The Capon beamformer is a more robust method and seems to be working well. These methods are seen to have a narrower 3 dB beamwidth compared to the conventional Sum-and-Delay. For more accurate resolution measurements two targets of similar RCS should be conducted, and this will be studied when testing the patch antenna array designed in this work The fundamental problem for the adaptive methods using the covariance matrix is that the signals from all frequency bins are being combined and evaluated at the same time, which can cause phantom target originating from reflections occurring only in some bins to appear. Moreover, the filtering of the baseband signal may need to be improved beyond a simple high pass filter.

Chapter 6
Proposal of Antenna Array Design

This chapter explains the different setups of antenna array placements with Sec. 6.1 showing the array factor pattern and the total gain for the different setups and Sec. 6.2 describing the proposed design with its corresponding virtual array.

6.1 Azimuth-Elevation Visualization

The goal of this thesis is, as formulated in the introduction, to investigate an already existing 1D array design (i.e. INRAS antennas) to try to get a good idea of how to create the new design of the 2D array. The INRAS frontend card, which supports 2 Tx and 8 Rx antennas, is used for MIMO by using TDMA. Since a uniform rectangular 2D array will require the use of single patch antenna elements, which have too low gain and too wide main beam in the elevation plane, problems with ground reflections can be expected. The array factor can be used to calculate the array pattern for an arbitrarily arranged array and to analyze which weight function would be optimal for Delay-and-Sum beam-steering. The resolution of the beam-steering is given by the effective aperture, which is described by (3.4). The resolution requirement becomes more difficult when both azimuth and elevation DOAs need to be distinguished. Since the pattern will be non-symmetrical, the angular resolution will change depending on the direction of the plane that is separating the objects. This is the case since a Uniform Rectangular Array (URA) or arrays of similar shapes are not symmetric along an arbitrary line crossing the array center, unlike a circular symmetric array.

In the linear case, the beamwidth is easily calculated by the length of the array projected in a certain direction. The effective aperture is $d(M_e - 1)\cos(\theta)$, where M_e is the number of elements in the virtual array, d is the distance between adjacent elements and θ is the projection angle. This is true for a URA aligned on the x-y plane as well as when looking along the x-z or y-z plane.

It is not possible for the antenna implementation in this thesis to use a URA-design, due to physical restrictions in the placement of the array antenna element. Therefore, inspired by designs given in [10], a rhomboid shape is proposed because of its similar performance to a URA and that it is possible to circumvent the physical restrictions in the element placement. Since the resolution in the azimuthal direction is more important and the limitation of the maximum use of 2 Tx and 8 Rx, the two following array geometries are proposed. Since the number of vir-

tual array elements is 16, a smart design would be to have a symmetric number of elements in both dimensions for the different designs. The array elements are placed in the y-z plane (vertical plane), consistent to the expected orientation of the array in the intended radar application. It should be noted that at this point, the array elements are assumed to be single-patch elements. The first two arrays use $\lambda/2$ element spacing in both y- and z-directions for a total of 2×8 element patterns (with the top row of elements in the second arrays shifted to the right by one element), while the second group of two arrays use $\lambda/2$ or λ spacing in the y-direction and λ in z-direction for a total of 4×4 elements (with the fourth array having shifted rows of elements). These arrays are visualized in the left subplots of Figures 6.1-6.4. The array factors (assuming isotropic elements) for the broadside scan angle are provided in the right subplots of Figures 6.1-6.4. Since the scan angle is limited in the elevation, a design with grating lobes present is proposed. By using the patch antenna array design, effects of the grating lobes giving false detections is reduced since the array element has a narrow main beam in the elevation plane, which is effectively multiplied to the array factor to obtain the actual array pattern.

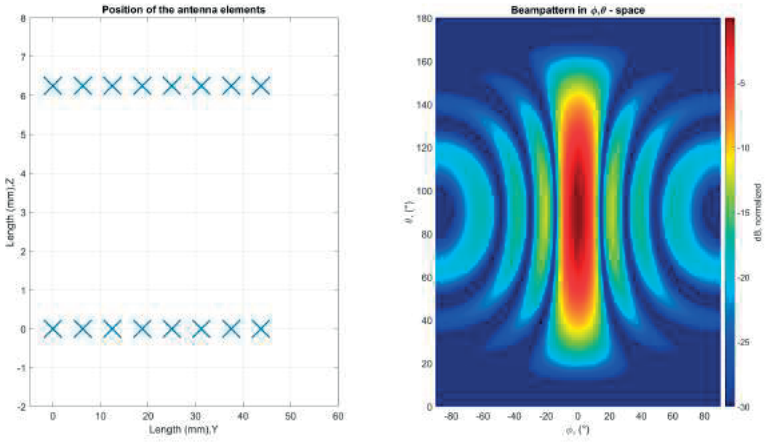

Figure 6.1: Array Factor pattern for 2×8 rectangular array.

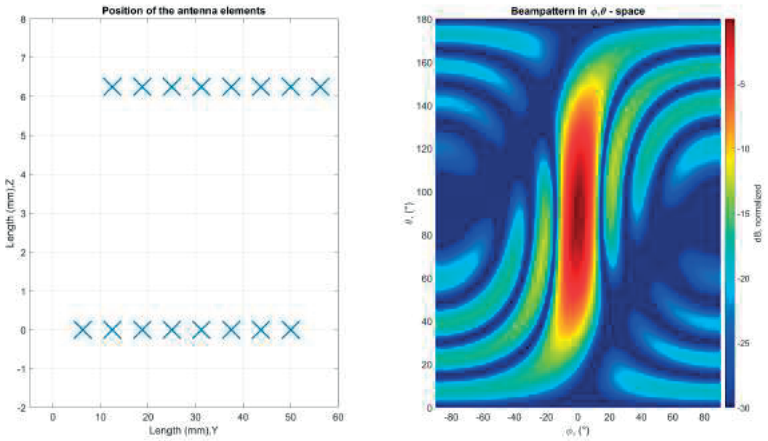

Figure 6.2: Array Factor pattern for 2×8 rhomboid array.

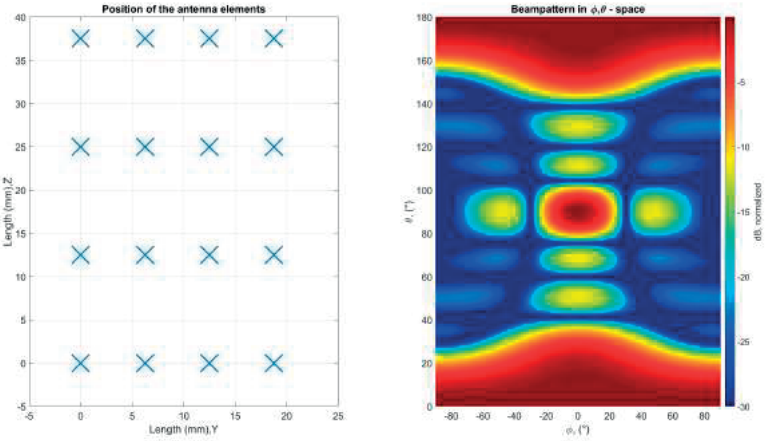

Figure 6.3: Array Factor pattern for 4×4 rectangular array.

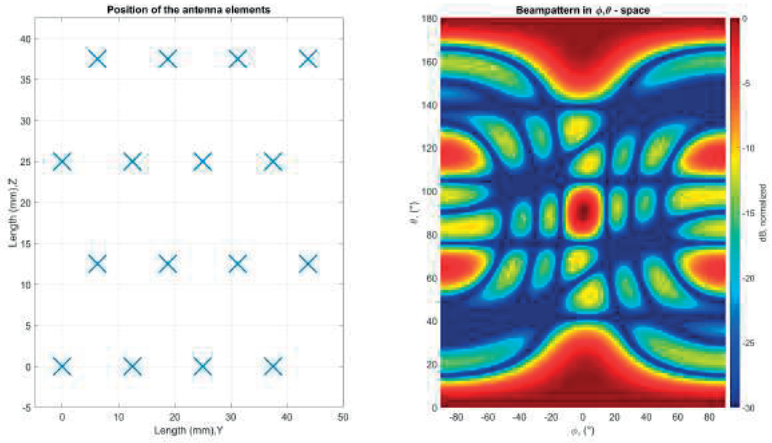

Figure 6.4: Array Factor pattern for 4×4 rhomboid array.

To get the full picture of the radiation pattern, one need to look at the actual array pattern given by (3.13). To get a good picture of how this affects the array factor that assumes isotropic element patterns, the total gain of the actual array pattern is shown in Figures 6.5-6.8. The case with λ-spacing in the array setups are given to visualize that the dampening of the grating lobes may not be sufficient, since a target with high RCS will cause false detections if located in the grating lobes. Chebyshev array pattern can be implemented to decrease the sidelobes, which is more useful for the 2×8 arrays, since it does not affect the grating lobes in the 4×4 configurations.

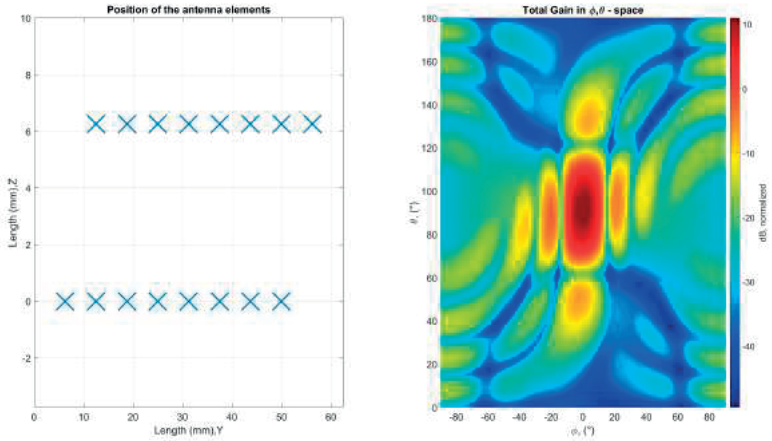

Figure 6.5: Total gain for the 2×8 rhomboid broadside array.

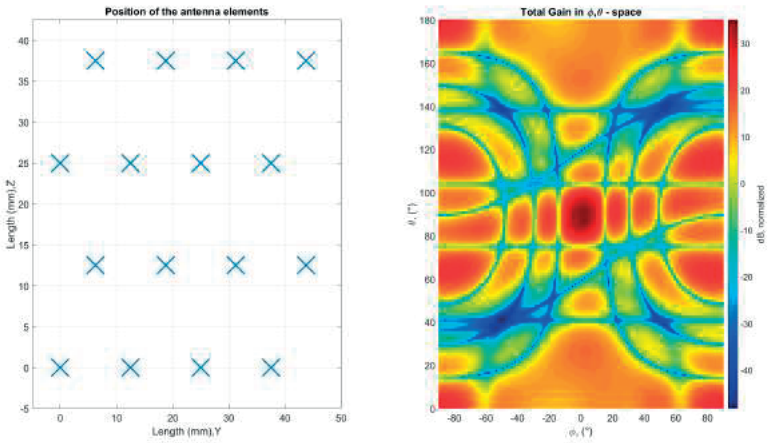

Figure 6.6: Total gain for the 4×4 rhomboid broadside array.

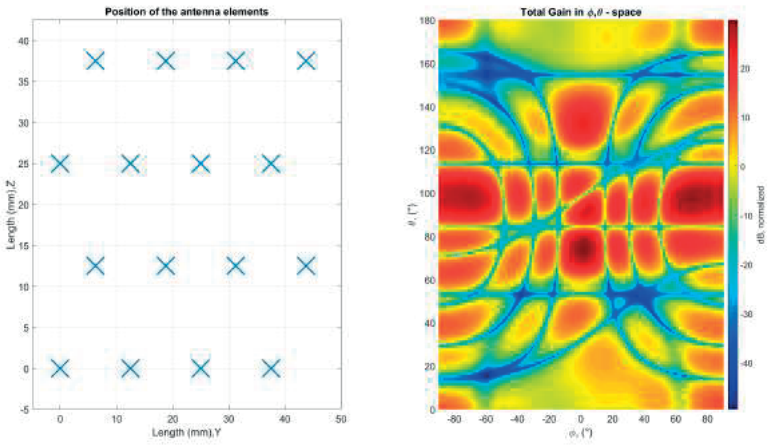

Figure 6.7: Total gain for the 4x4 rhomboid array. Beam steered in the direction $\phi = 0°$, $\theta = 70°$.

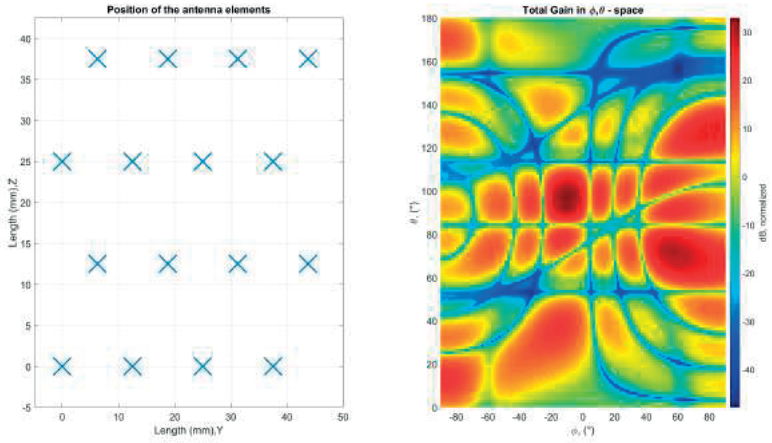

Figure 6.8: Total gain for the 4×4 rhomboid array. Beam steered in the direction $\phi = 60°$, $\theta = 70°$.

6.2 Proposed Design

The two proposed designs are shown in Figure 6.2 and Figure 6.4. The virtual array needs to be formed using equation (3.28). The proposed designs that include virtual array elements are shown in Figure 6.9, where the dots represent the actual antenna array elements and the crosses represent the convoluted virtual arrays, where the left Tx-antenna array is used to synthesize the virtual arrays. In Figure 6.9, the first configuration shows the 4×4 rhomboid design and the second one shows the 2×8 rhomboid design.

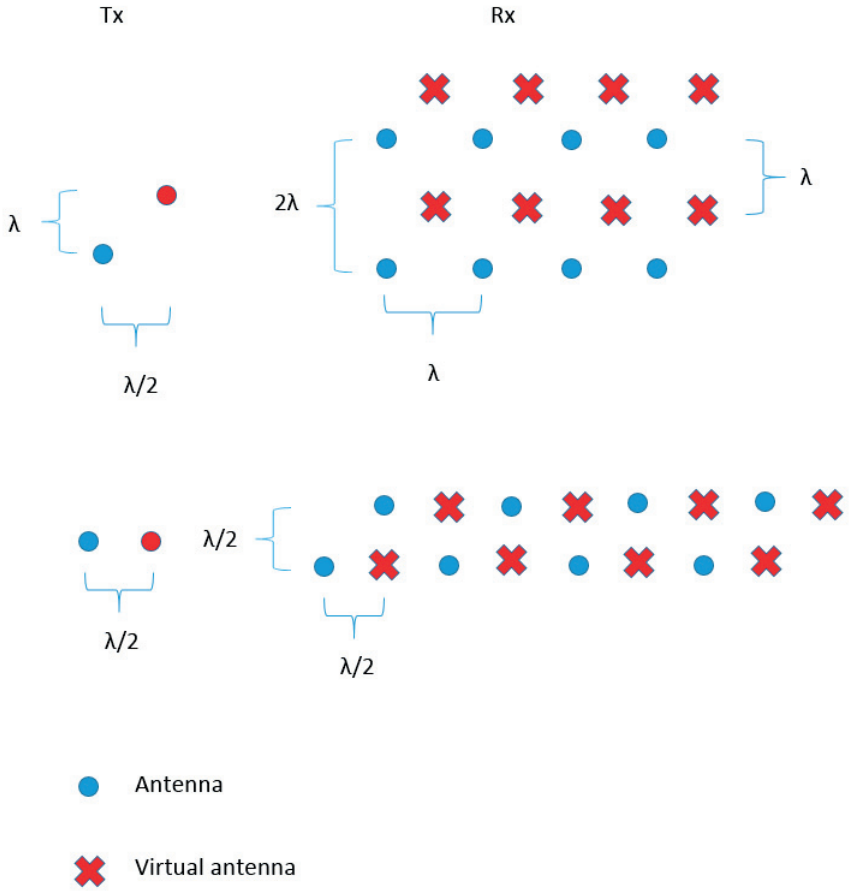

Figure 6.9: The proposed designs and how the virtual arrays are created.

The distance between the Tx and Rx arrays is not relevant when calculating the virtual array. As seen in Figure 5.10, the Tx and Rx arrays are not well separated in the original INRAS arrays and this is probably one of the reasons why a strong low frequency signal component was seen in the verification test of

the INRAS Radarbook system. In Figure 5.6 it is obvious that the low frequency component magnitude is a function of the distance from the transmitting antenna, since Tx 1 is positioned closest and Tx 8 is positioned furthest away. Rx to Tx isolation is thus important with regard to several factors such as to get a good covariance matrix estimation and not to saturate the Low Noise Amplifier (LNA) in the input stage of the Rx array, causing non-linear effects to distort the received signal that is of interest or even causing stability issues in the input stage.

The design is then realized using CST and the final design is shown in Figure 7.12 in Ch. 7.

Chapter 7

Simulation Results of Antenna Array Element

This chapter goes through the process of designing the antenna array elements and the simulations of these. Firstly, the process of designing the 24 GHz single patch antenna is described in Sec. 7.1. Thereafter, in Sec. 7.2, using the single patch antenna, the 4×1 linear patch antenna array is designed. Finally, multiple antenna arrays are put together to obtain the final design in Sec. 7.3. After the design process is described, the simulation results are presented in Sec. 7.4-7.5. The software program that was used for this design process is Computer Simulation Technology Studio Suite (CST Studio Suite), which is described in Sec. 5.1. All the simulations were made with the frequency domain solver in CST.

7.1 Design of 24 GHz Single Patch Antenna

The rectangular patch antenna was designed with the help from a CST tutorial [1]. The patch antenna that was designed is shown in Figure 7.1 with the dimensions W and L. The ground plane and substrate were defined to be twice as large as the patch antenna, i.e. 2W and 2L. The dimensions of the patch antenna were calculated according to the guide described in Sec. 3.5.2 as a first approach. The antenna is fed with a microstrip line where W_f and L_f are the dimensions of the microstrip line, g is the gap distance between the microstrip line and the patch antenna and d is the inset feed distance. These dimensions, including those of the patch antenna, were not finally determined at this point, but subject to change during the simulations to obtain the best performance.

The ground plane was defined as annealed copper with a thickness of 12 µm and is shown in Figure 7.2. The substrate chosen was Rogers RO4350B with the dielectric constant of $\epsilon_r = 3.48$, since its material properties are suitable for high frequency applications such as 24 GHz patch antennas. The substrate was located on top of the ground plane with a height of 0.25 mm and can be seen in Figure 7.3.

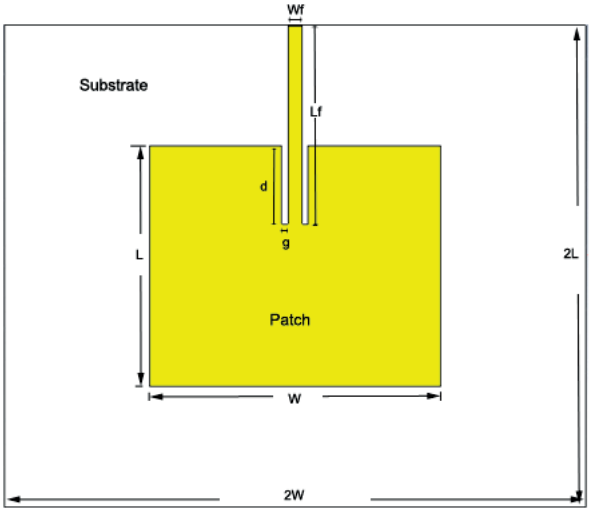

Figure 7.1: Single patch antenna with microstrip feed line [1].

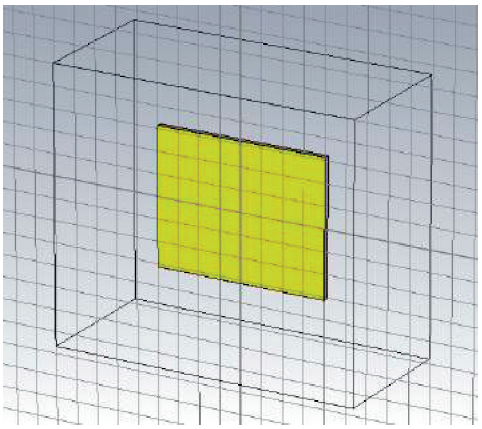

Figure 7.2: Ground plane consisting of 12 µm thick annealed copper.

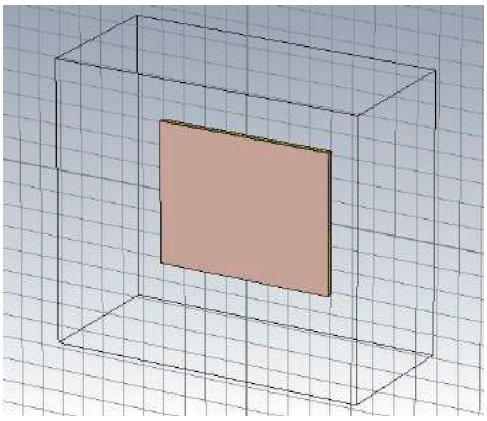

Figure 7.3: Substrate consisting of 0.25 mm RO4350B with the dielectric constant $\epsilon_r = 3.48$.

Thereafter, the patch was created on top of the substrate with the same material and thickness as the ground plane. Figure 7.4 shows the patch added on top of the substrate.

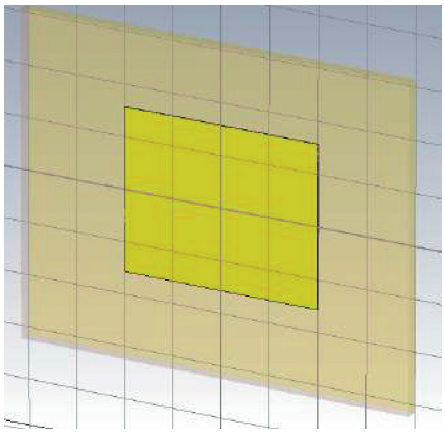

Figure 7.4: The patch consisting of 12 µm annealed copper added on top of the substrate.

After the patch was defined, the microstrip feed line needed to be created. To do this, first an empty space was created (see Figure 7.5a) and then the microstrip feed line was added as shown in Figure 7.5b. This created a gap between the antenna and the microstrip line. The final designed patch antenna with the microstrip feed line is shown in Figure 7.6.

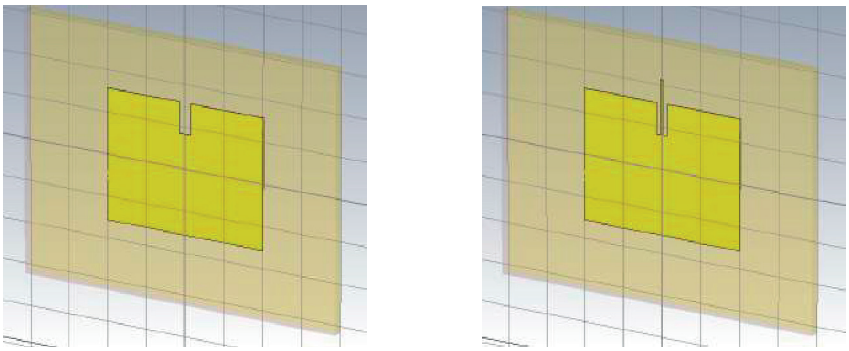

(a) Empty space created on the patch. **(b)** Microstrip line added to the patch.

Figure 7.5: First the empty space is created and then the microstrip line is added to the patch.

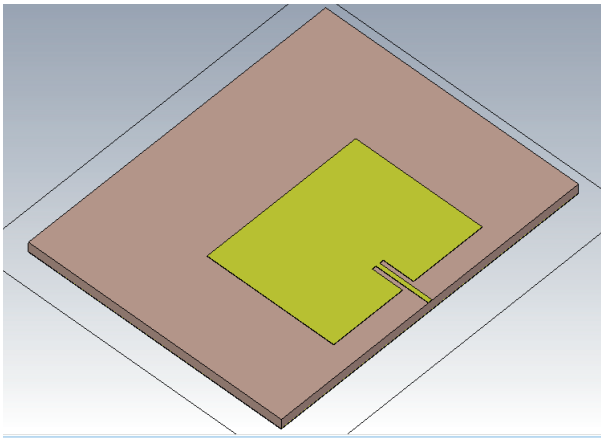

Figure 7.6: The final design of the 24 GHz patch antenna.

The dimensions of the final patch antenna design were:

- Width of the patch, W = 4.5 mm
- Length of the patch, L = 3.13 mm
- Width of the microstrip line, W_f = 0.1 mm
- Length of the microstrip line, L_f = 1.81 mm
- Distance of gap, g = 0.1 mm
- Inset feed distance, d = 0.75 mm
- Height of substrate, h = 0.25 mm
- Thickness of patch, t = 12 µm

7.2 Design of 4x1 Linear Patch Antenna Array

Continuing with the work on the single patch antenna, a 4×1 linear antenna array was created and is shown in Figure 7.7. The dimensions of the two inner patch antennas differ from the two outer ones. The inner patch antennas are slightly wider and shorter due to it being desirable to have larger radiated power in the center of the array. The inner patches have exactly the same dimensions as described in the previous section, while the outer ones have the length L = 3.17 mm and the width W = 4 mm. The size of the ground plane and the substrate is 10 mm x 32 mm and the distance between each patch is $\lambda/2 = 6.25$ mm.

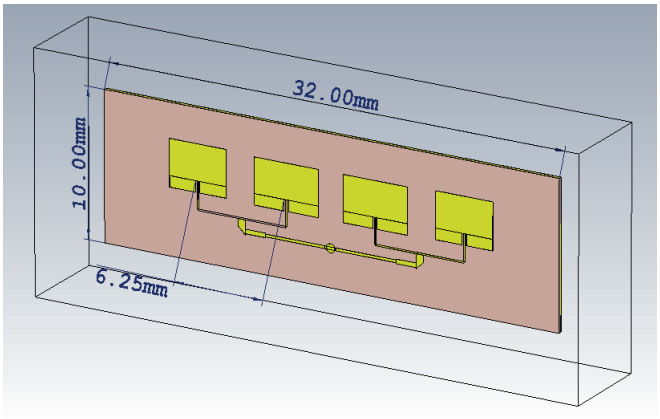

Figure 7.7: 4x1 linear patch antenna array.

7.2.1 Feeding Network

The patch antennas are fed through a feeding network where the power is divided between two patch antennas, as seen in Figure 7.8. Due to impedance mismatch between the patch antenna and the transmission line, a quarter-wave impedance transformer is used. Typically the patch antenna has an impedance of 200 Ω or more and the transmission line 50 Ω. The use of the quarter-wave impedance transformer, as described in Sec. 3.5.1, is necessary in order to ensure there is good impedance matching between the patch antennas and the transmission lines.

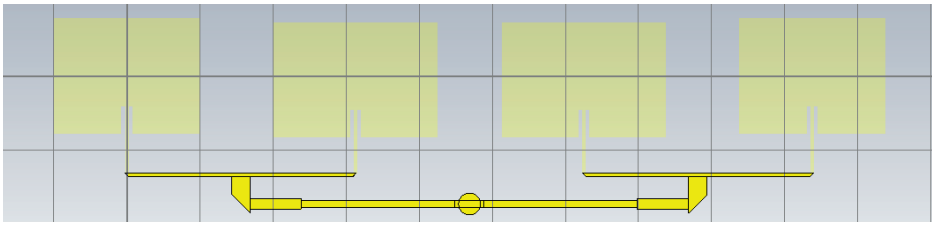

Figure 7.8: The feeding network for the 4x1 linear patch antenna array.

7.3 Final Design

After the 4×1 linear patch antenna array had been designed, multiple arrays were put together in different configurations of 2-element Tx arrays and 8-element Rx arrays to obtain the final design. These configurations were chosen based on the theory of virtual array, as described in Sec. 3.4.1, in order to achieve good performance. The corresponding virtual arrays are shown in Figure 6.9 in Ch. 6.

7.3.1 First Design Configuration

Figure 7.9 shows the first design configuration, where the horizontal element separation distance for the 2-element Tx arrays is $\lambda/2 = 6.25$ mm and the vertical element separation distance is $\lambda = 12.5$ mm. The horizontal distance between the 8 Rx arrays is λ and the vertical distance is 2λ. The separation distance between the Tx array and the Rx array is (Tx array center to Rx array center) 4λ, but this distance is of no great importance to the performance.

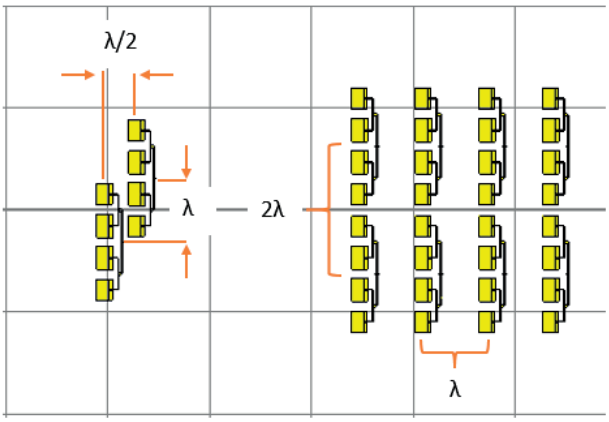

Figure 7.9: First design configuration.

7.3.2 Second Design Configuration

The second configuration is shown in Figure 7.10, where the horizontal element separation distance between the 2-element Tx array is $\lambda/2 = 6.25$ mm. There is no vertical element separation in this case. The horizontal element separation distance for the 8-element Rx array is $\lambda/2$ and the vertical element separation distance is $\lambda/2$.

7.3.3 Third Design Configuration

The last configuration is a mix of the two first configurations. It consists of the same Tx array placement as the second configuration and the same Rx array placement as the first configuration. Figure 7.11 shows this configuration.

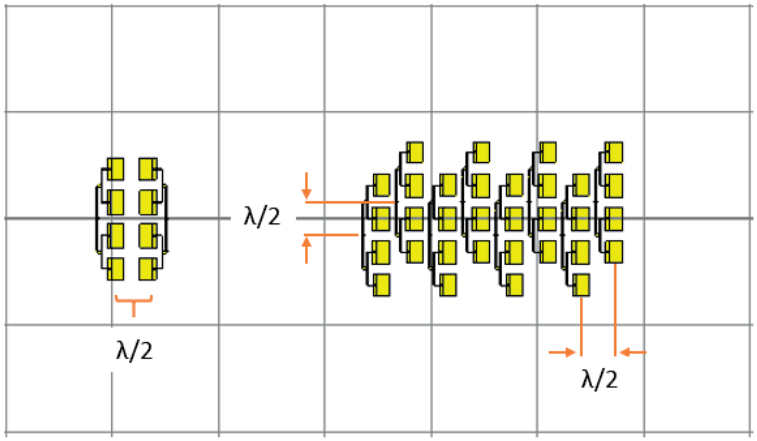

Figure 7.10: Second design configuration.

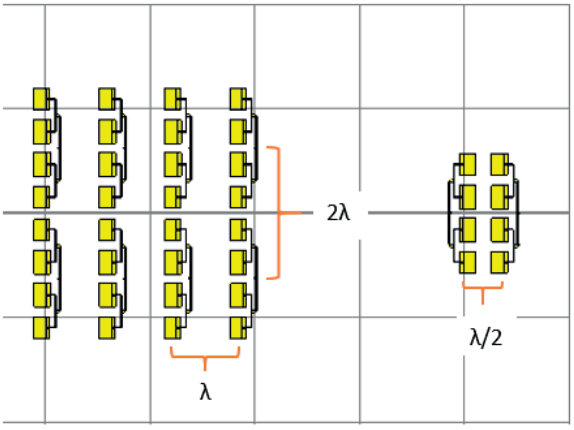

Figure 7.11: Third design configuration.

7.3.4 Final Design Configuration

Putting the three above configurations together, the final design is obtained and shown in Figure 7.12.

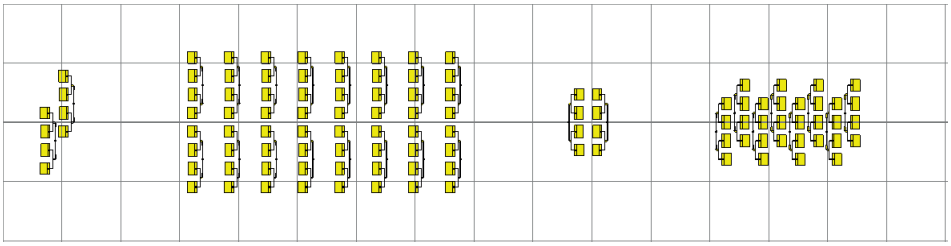

Figure 7.12: Final design configuration.

Final Design Configuration with Two Extra Antenna Arrays

Two more antenna arrays were added to the final design configuration, as shown in Figure 7.13. The first extra antenna is located $\lambda/2$ in horizontal distance and λ in vertical distance from its closest neighbour antenna. The second extra antenna is located $\lambda/2$ in horizontal distance from its closest neighbour antenna. The use of the extra antennas is desirable if the application of Time Division Multiple Access (TDMA) is problematic; these extra antennas can be used to create multiple virtual array elements on the same spatial location.

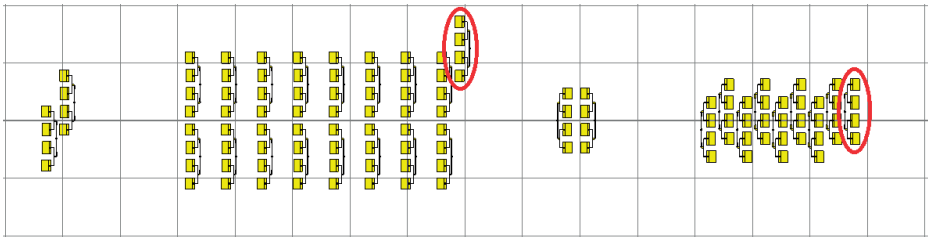

Figure 7.13: Final design configuration with two extra antenna arrays used for TDMA application.

7.4 Simulation of 24 GHz Single Patch Antenna

Figure 7.14 shows the S_{11} scattering parameter, also known as the reflection coefficient, for the 24 GHz single patch antenna. The S_{11} parameter shows how much power that is reflected from the antenna and it can be seen from the figure that the antenna reflects the least around $f \approx 24.1$ GHz, with the $S_{11} \approx$ -40.6 dB.

The impedance bandwidth, B, is the frequency interval where the patch antenna has a reflection coefficient below a certain dB value. A very common value

is -10 dB; using this and Figure 7.14, the bandwidth is obtained as $B \approx 700$ MHz. Using (3.5), the fractional bandwidth is $FBW \approx 2.90$ %.

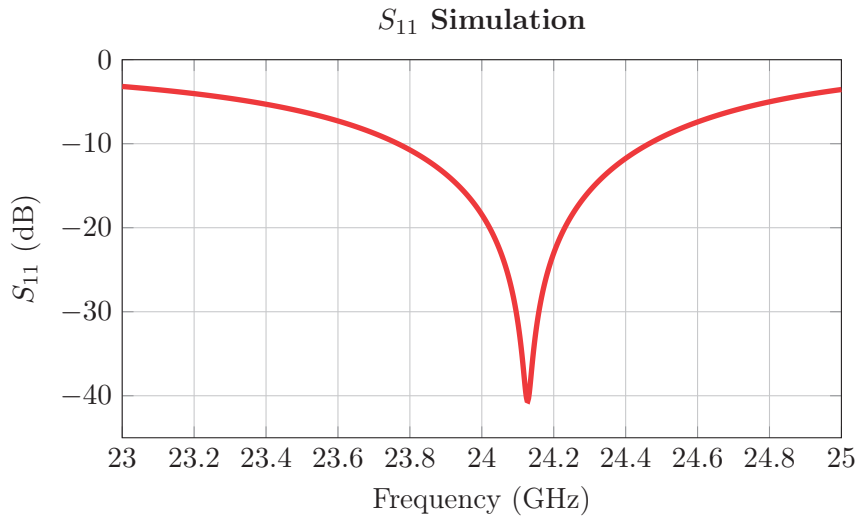

Figure 7.14: S_{11} of the 24 GHz single patch antenna.

Figure 7.15 shows the Z_{11} impedance parameter, which describes the open circuit input impedance of the system. The real part of this parameter is $\mathrm{Re}(Z_{11}) \approx 105\ \Omega$ and the imaginary part is $\mathrm{Im}(Z_{11}) \approx$ -0.661 Ω for the operating frequency $f = 24.1$ GHz.

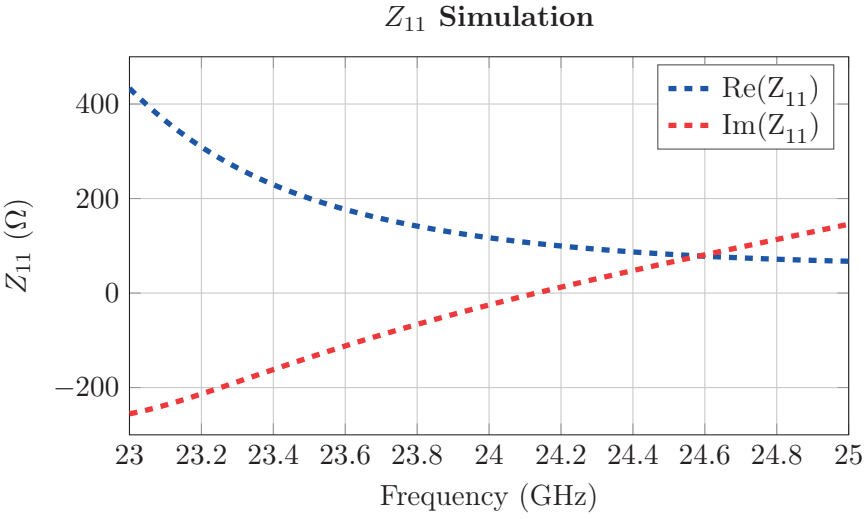

Figure 7.15: Z_{11} of the 24 GHz single patch antenna.

The 3D simulation plot of the far field radiation pattern for the patch antenna is shown in Figure 7.16. The directivity for the antenna is 7.14 dBi.

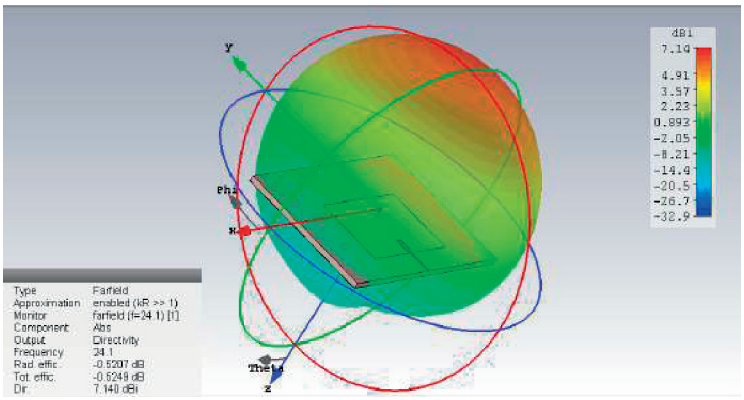

Figure 7.16: Directivity of the 24 GHz single patch antenna. The dBi range is -32.9 dBi - 7.14 dBi.

7.5 Simulation of 4x1 Linear Patch Antenna Array

Figure 7.17 shows the S_{11} parameter for the 4×1 linear patch antenna array. From the figure it can be seen that the patch antenna array reflects the least around the frequency $f \approx 24.2$ GHz, with the $S_{11} \approx$ -22.6 dB.

The bandwidth for the patch antenna array can be obtained from Figure 7.17 and is around $B \approx 1$ GHz. Using (3.5), the fractional bandwidth is obtained as $FBW \approx 4.13$ %.

Figure 7.18 shows the Z_{11} impedance parameter for the 4×1 linear patch antenna array. The figure shows that the real part of this parameter is $\mathrm{Re}(Z_{11}) \approx 58.8\ \Omega$ and the imaginary part is $\mathrm{Im}(Z_{11}) \approx$ -3.21 Ω for the operating frequency $f = 24.2$ GHz.

The crosstalk (or coupling coefficient) between two $\lambda/2$-spaced patch antenna array elements is shown in Figure 7.19. It is around -29.2 dB at the operating frequency for antennas 1 and 2. The S_{12} parameter shows how much power is coupled into antenna 1 relative to the power input at antenna 2.

Figure 7.20 shows a 2D plot of the directivity for the 4×1 linear patch antenna array and Figure 7.21 shows the corresponding 3D plot. The directivity for the antenna array is 11.8 dBi.

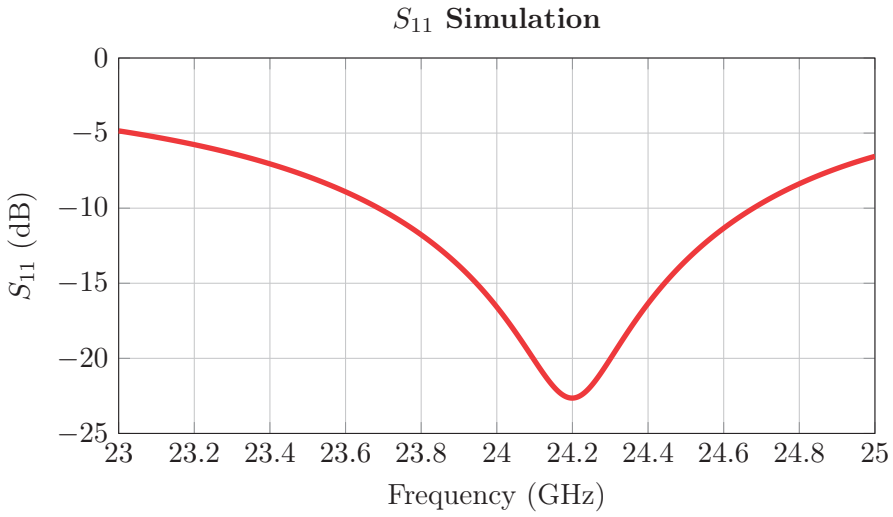

Figure 7.17: S_{11} of the 4x1 linear patch antenna array.

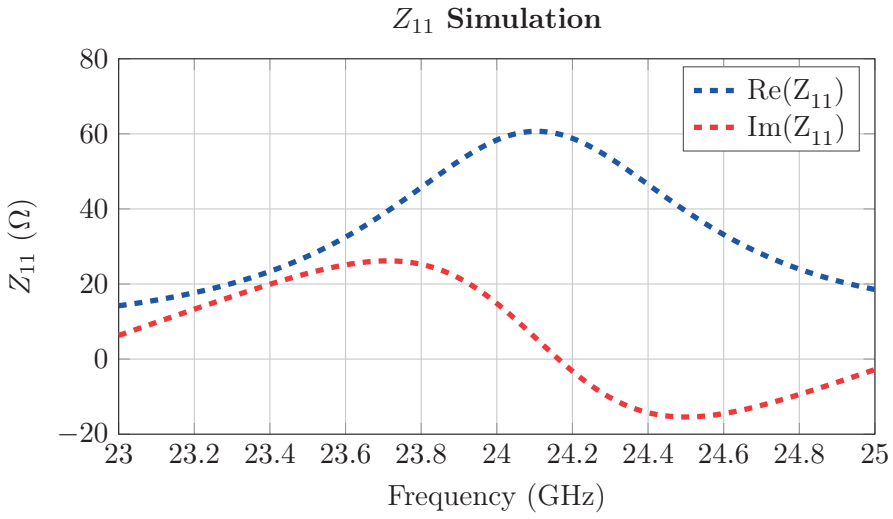

Figure 7.18: Z_{11} of the 4x1 linear patch antenna array.

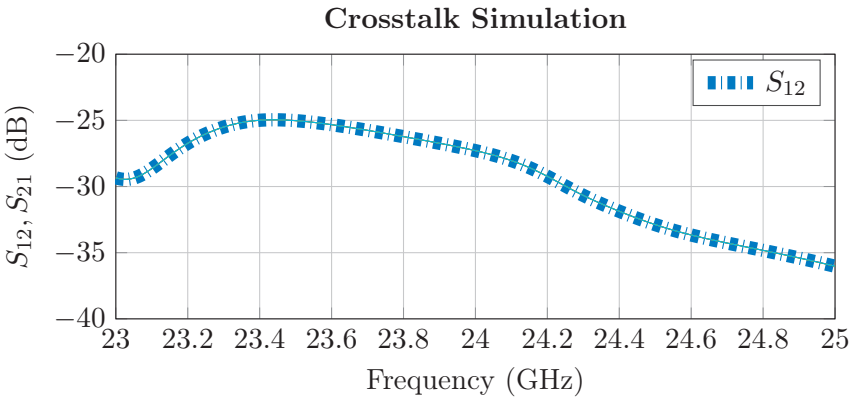

Figure 7.19: Crosstalk of two $\lambda/2$-spaced antenna array elements.

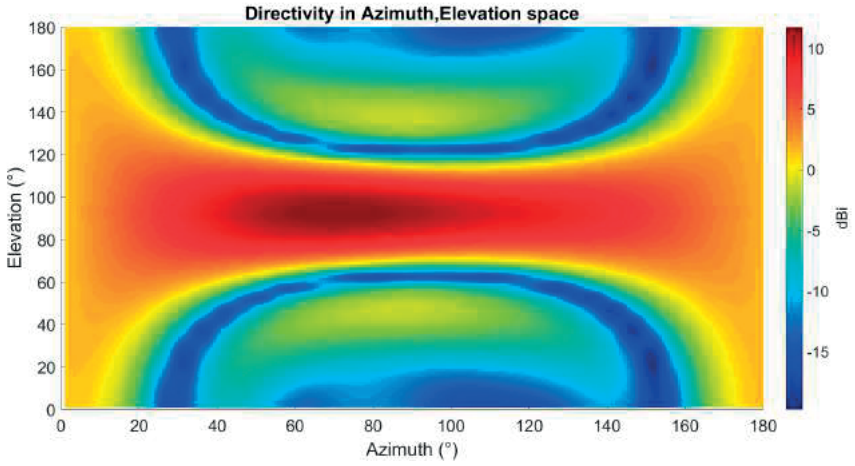

Figure 7.20: Directivity of the 4x1 linear patch antenna array in the azimuth-elevation plane.

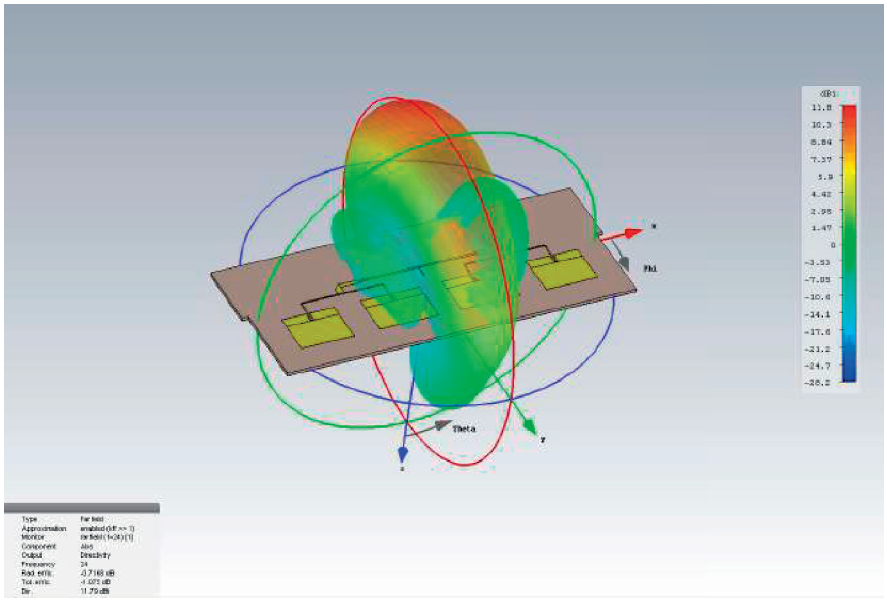

Figure 7.21: Directivity of the 4x1 linear patch antenna array. The dBi range is -28.2 dBi - 11.8 dBi.

Chapter 8
Measurement Results

This chapter presents the manufactured final antenna array design and the measurement results. Sec. 8.1 shows the manufactured antenna arrays, Sec. 8.2 describes the calibration of this design, Sec. 8.3 goes through the S-parameter measurements, and Sec. 8.4 presents the results obtained with the different Direction-of-Arrival (DOA) methods.

8.1 Manufactured Patch Antenna Arrays

The design was manufactured by Malmö Mönsterkort and the final manufactured design is shown in Figure 8.1. This is the same design in CST, showed in Figure 7.12, that has been realized. Initially there were some problems regarding the dimensions of the PCB (Printed Circuit Board) which did not meet the Design Rule Check (DRC), but this problem was solved by increasing the size of the mitered bends.

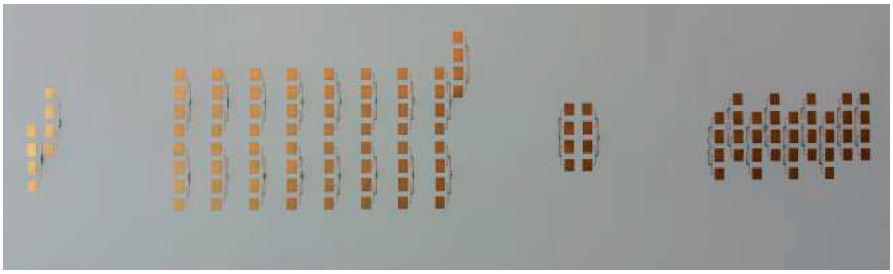

Figure 8.1: Picture of the manufactured antenna arrays.

A small miscalculation was that the microstrip line did not end in the via and the last 0.1 millimeters had to be connected by soldering, which is not optimal with regard to the feeding network design. The connectors used were ordinary SMA connectors. Figure 8.2 shows the backside of the PCB, together with the feed cables and SMA connectors.

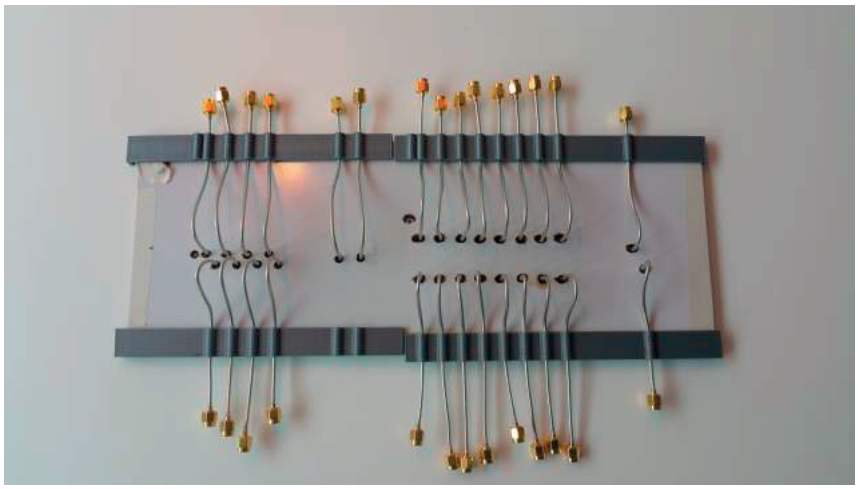

Figure 8.2: Picture of the backside with soldered rigid flex cables.

8.2 Calibration

Calibration of the arrays is done by the same method as calibrating the INRAS frontend. The calibration data is derived for a single angle of incidence and the mutual coupling between the elements is neglected. The simplest form is to put an object at the broadside direction. Since the distance is roughly the same to each element the phase should be equal. This means that the range, phase and magnitude profile should be identical for each antenna. One of the Tx-antennas was used as a reference.

This rudimentary procedure was performed for each Tx antenna in the 2×8 and 4×4 rhomboid array configurations with a reflector placed $R = 5$ m in the direction $\phi = 0°, \theta = 90°$, i.e., straight in front of the radar. As a reference, antenna 4 was chosen in both configurations. The calibration coefficients are shown in Table 8.1 and Table 8.2.

Antenna	Real Part	Imaginary Part	Tx Antenna
1	-1.7561	-0.0458	1
2	0.8424	-0.5451	1
3	0.2781	0.9942	1
4	1.0000	0.0000	1
5	-1.0386	0.0267	1
6	0.2948	0.9090	1
7	0.0331	-1.1729	1
8	-0.4858	1.5525	1
Antenna	Real Part	Imaginary Part	Tx Antenna
1	1.6286	-0.1086	2
2	0.8533	-0.5546	2
3	0.2832	0.09463	2
4	1.0000	0.0000	2
5	1.0084	0.0364	2
6	0.2356	0.9561	2
7	0.0141	-1.1229	2
8	-0.5467	-1.6575	2

Table 8.1: Calibration coefficients calculated for 2×8 rhomboid configuration.

Antenna	Real Part	Imaginary Part	Tx Antenna
1	0.9679	-1.7614	1
2	0.8072	-0.5671	1
3	0.1602	1.0437	1
4	1.0000	0.0000	1
5	-1.0119	0.5703	1
6	0.1754	1.0123	1
7	0.7355	-0.6136	1
8	-0.7489	0.4835	1
Antenna	Real Part	Imaginary Part	Tx Antenna
1	0.2038	-1.6471	2
2	0.4538	-0.7345	2
3	0.5107	0.7576	2
4	1.0000	0.0000	2
5	-0.6410	1.0024	2
6	0.0870	0.0997	2
7	0.7427	-0.4602	2
8	-0.6882	0.3591	2

Table 8.2: Calibration coefficients calculated for 4×4 rhomboid configuration.

8.3 Measurement of S-Parameters

To measure the S-parameters of the manufactured antenna arrays, a network analyzer was used. The network analyzer was the E8361A PNA Series Network Analyzer by Agilent Technologies. The mutual coupling between two adjacent elements in each antenna array was measured by connecting one antenna to port 1 of the analyzer and the other antenna to port 2, as seen in Figure 8.3.

Figure 8.4 shows the measured S_{11} parameter of the 4×1 linear patch antenna array. There are three resonances where the antennas have a reflection coefficient of below -10 dB, their center frequencies are $f_1 \approx 23.5$ GHz with a reflection coefficient of $S_{11}(f_1) \approx$ -21.5 Ω, $f_2 \approx 24.1$ GHz with a reflection coefficient of $S_{11}(f_2) \approx$ -24.7 Ω, and $f_3 \approx 24.7$ GHz with a reflection coefficient of $S_{11}(f_3) \approx$ -12.4 Ω.

The measured crosstalk between two $\lambda/2$-spaced patch antenna arrays is shown in Figure 8.5. The crosstalk is around -27.7 dB at the smallest reflecting frequency $f = 24.1$ GHz.

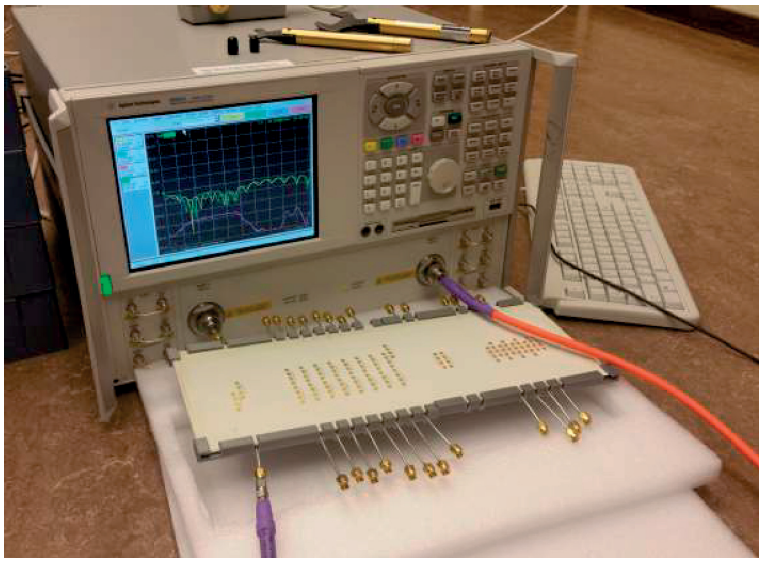

Figure 8.3: Measurement of S-parameters using the network analyzer.

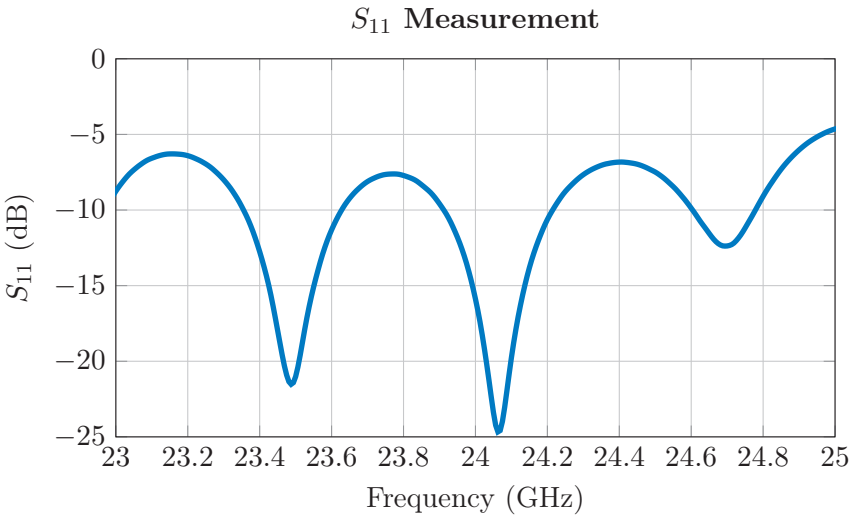

Figure 8.4: S_{11} measurement of the 4x1 linear patch antenna array.

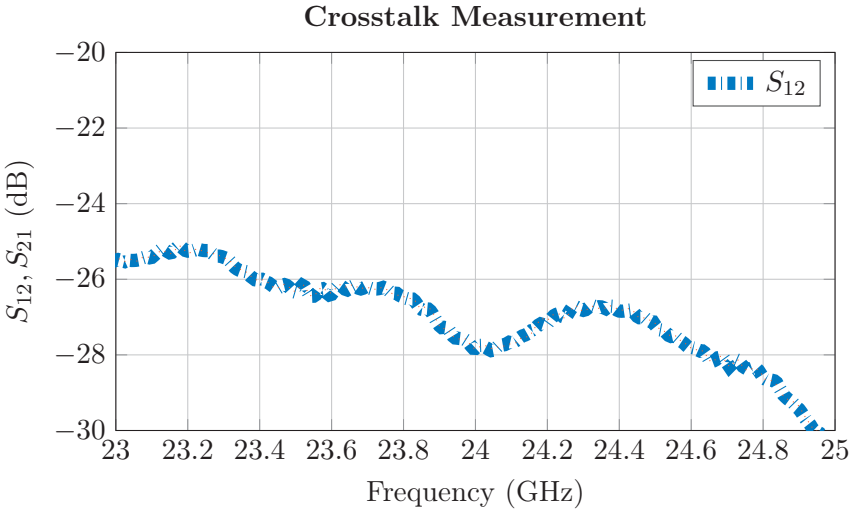

Figure 8.5: Crosstalk measurement of two $\lambda/2$-spaced antenna array elements.

8.4 Tests with Direction-of-Arrival Algorithms

Two different tests were conducted to verify and measure the performance of the manufactured arrays. The algorithms that were verified in Sec. 5.3 were tested in both azimuth and elevation. This was conducted in an environment that was clutter-free enough to get accurate measurements.

A target scene containing two stationary targets were measured and the different algorithms were implemented to see how well they could resolve the targets with an angular separation. The first test scenario contained only one target and the second test scenario contained two targets located at different azimuth and elevation angles. Three different DOA methods were tested to evaluate their performance: Sum-and-Delay, Capon/MVDR and MUSIC. The power of the range bin was then plotted in (ϕ, θ) space. The power spectrum of the Capon/MVDR algorithm was not normalized to show the correct power. This is due to the used butterworth bandpass filter, which was implemented to filter out the low frequency signals that were not from the range bin of interest. In these methods the locations of the spectrum peaks, which corresponds to incoming signals, are of interest.

Figure 8.6 shows the test setup with the INRAS Radarbook and frontend connected to the antenna board via mini-SMP to SMA connectors.

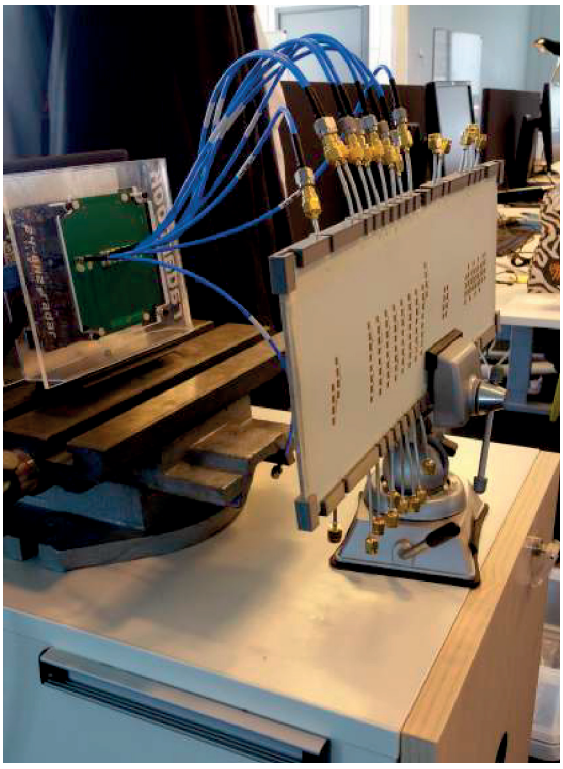

Figure 8.6: The INRAS Radarbook with the frontend connected to the antenna board.

During the measurement tests, the bandwidth was increased to use the band 23.7 GHz - 24.3 GHz in order to ensure that performance of the antennas were equivalent. This is due to the fact that not all of the antennas had a bandwidth in the desired range 24 GHz - 24.25 GHz due to mismatches, but all of the tested antennas had a bandwidth which was included the 23.7 GHz - 24.3 GHz range. Due to lack of time, the intended (narrower) frequency range of 24 GHz - 24.25 GHz was not tested.

8.4.1 Test Scenario One

The first test scenario contained a reflector located $R = 5.5$ m from the radar with an azimuth angle of $\phi = -43°$ relative to the radar, as shown in Figure 8.7. The radar is located around 1 m above the ground and using simple algebra, the elevation angle of the target relative to the radar is $\theta = \arctan(1/5.5) + 90° \approx 100°$.

Figure 8.7: The reflector located $R = 5.5$ m from the radar with an azimuth angle of $\phi = -43°$ and an elevation angle of $\theta = 100°$ relative to the radar.

Results with the 2×8 Rhomboid Array Configuration

Figures 8.8-8.10 show the results obtained with the 2×8 rhomboid configuration for test scenario one, where the position of the reflector is marked with a red circle. The range bin corresponding to the distance to the reflector was used to conduct the DOA-algorithms in (ϕ, θ) space. The MUSIC algorithm assumed 7 impinging signals corresponding to the seven highest eigenvalues of the estimated covariance matrix.

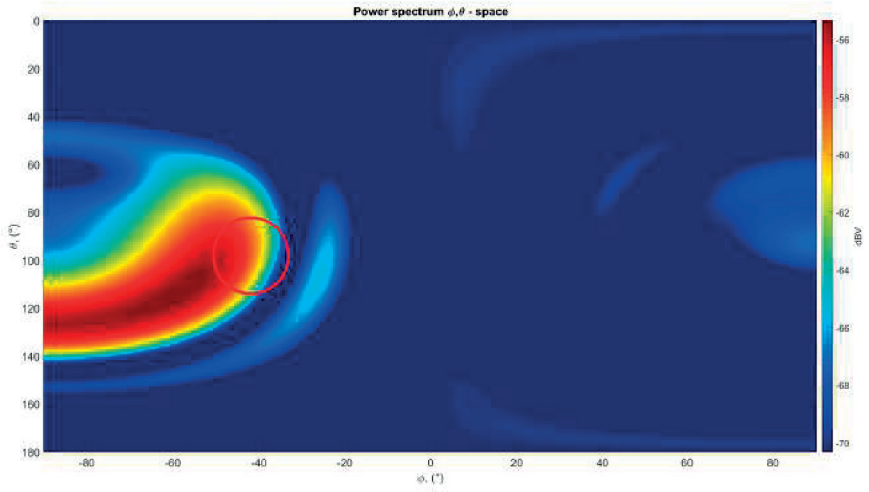

Figure 8.8: Power spectrum of the Sum-and-Delay beamformer.

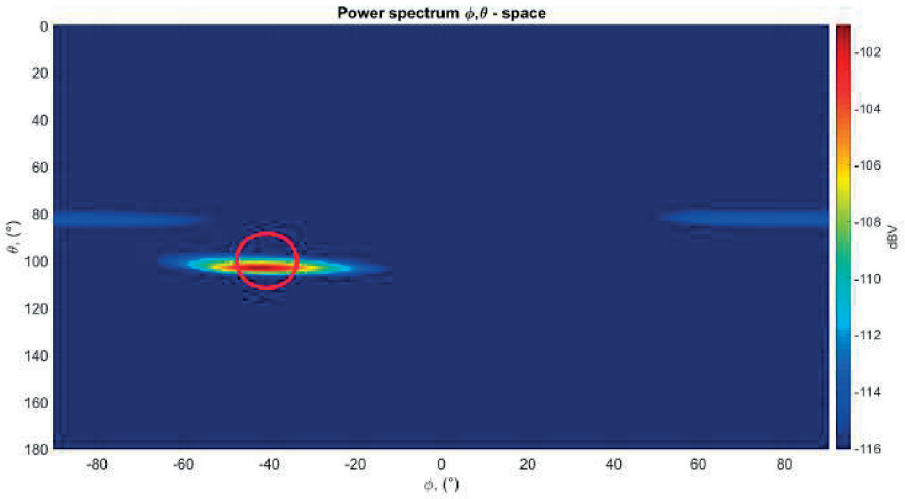

Figure 8.9: Pseudo power spectrum of the Capon/MVDR algorithm.

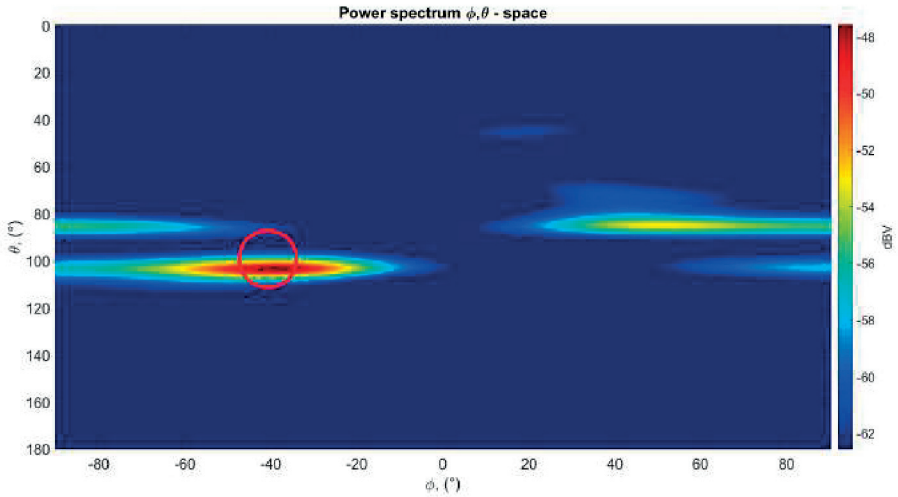

Figure 8.10: Pseudo power spectrum of the MUSIC algorithm.

Results with the 4×4 Rhomboid Array Configuration

Figures 8.11-8.13 shows the results obtained with 4×4 rhomboid configuration for test scenario one. The location of the reflector is marked in the figures with a red circle.

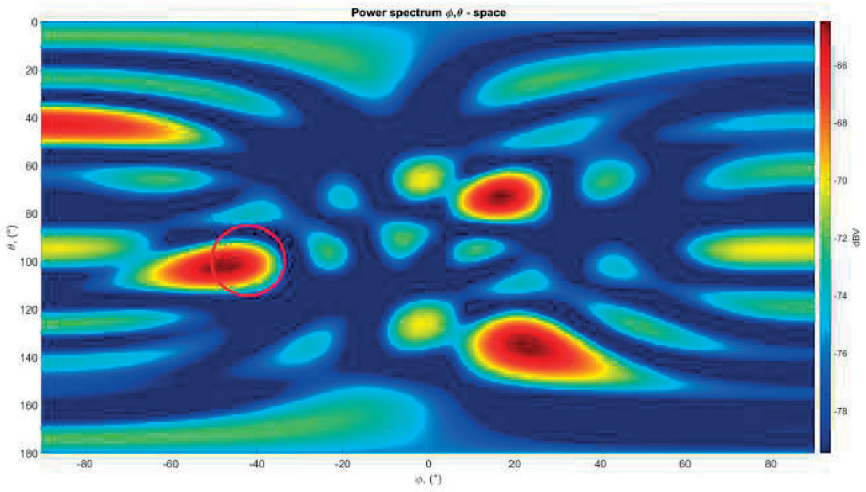

Figure 8.11: Power spectrum of the Sum-and-Delay beamformer.

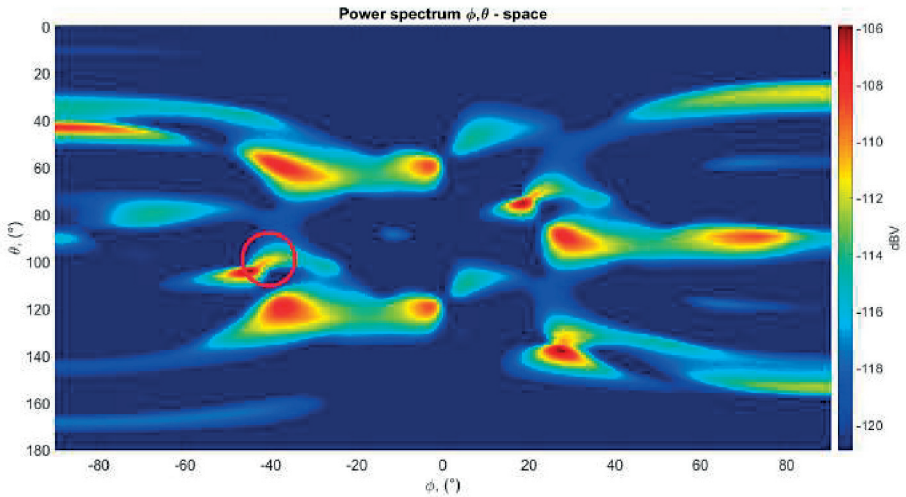

Figure 8.12: Pseudo power spectrum of the Capon/MVDR algorithm.

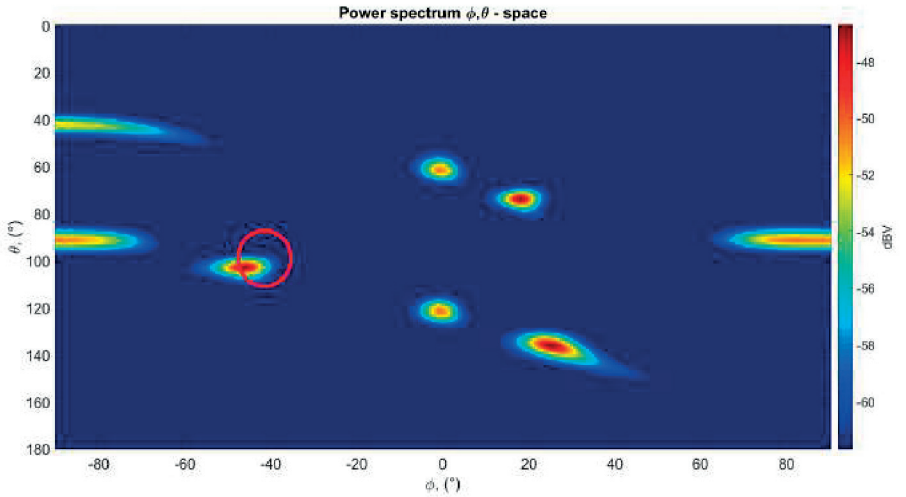

Figure 8.13: Pseudo power spectrum of the MUSIC algorithm.

8.4.2 Test Scenario Two

This scenario is similar to the first one, but in this case an additional reflector was added and its azimuth angle was slightly decreased (relative to the array broadside). The test scenario is shown in Figure 8.14, where the second reflector is located $R = 5.3$ m from the radar with an azimuth angle of $\phi = 22^\circ$ relative to the radar. The elevation angle is $\theta = \arctan(1/5.3) + 90^\circ \approx 101^\circ$, which is around the same as for the first reflector.

This scenario did not just test the accuracy of the algoritms as was the case for scenario one, but it also tested the resolution as well as the possible presence of fake targets due to the grating and/or sidelobe effects from the targets interacting with each other. The Capon/MVDR and MUSIC methods for the 2×8 array seem to fail and gives large errors in the DOA-estimations.

Figure 8.14: The second reflector located $R = 5.3$ m from the radar with an azimuth angle of $\phi = 22^\circ$ and an elevation angle of $\theta = 101^\circ$ relative to the radar.

Results with the 2×8 Rhomboid Array Configuration

Figures 8.15-8.17 shows the results obtained with the 2×8 rhomboid configuration for test scenario two. The position of the first reflector is marked with a red circle and the position of the second reflector is marked with a blue circle.

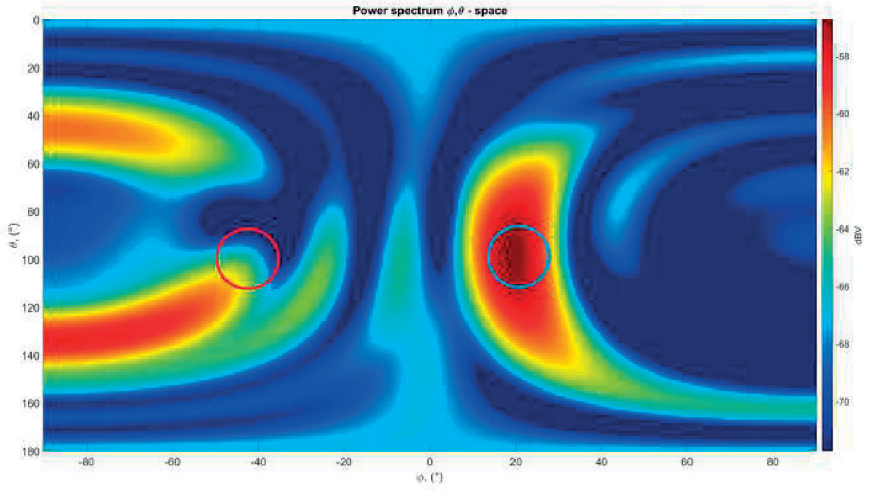

Figure 8.15: Power spectrum of the Sum-and-Delay beamformer.

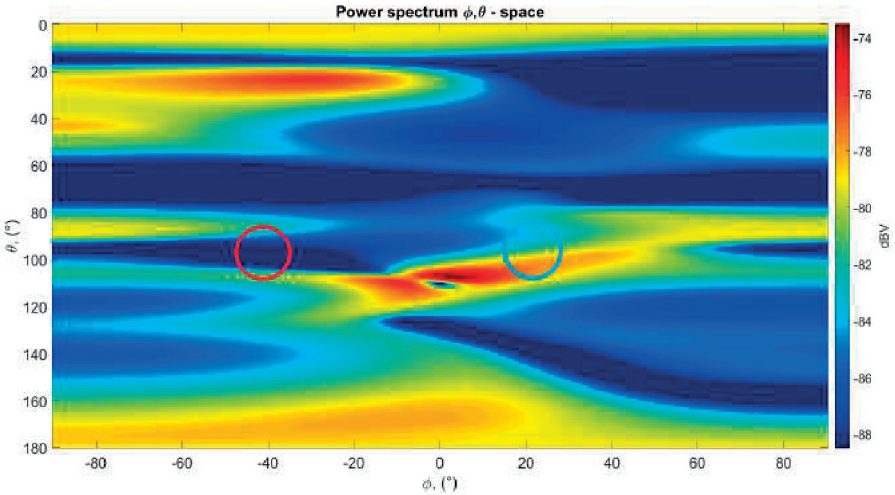

Figure 8.16: Pseudo power spectrum of the Capon/MVDR algorithm.

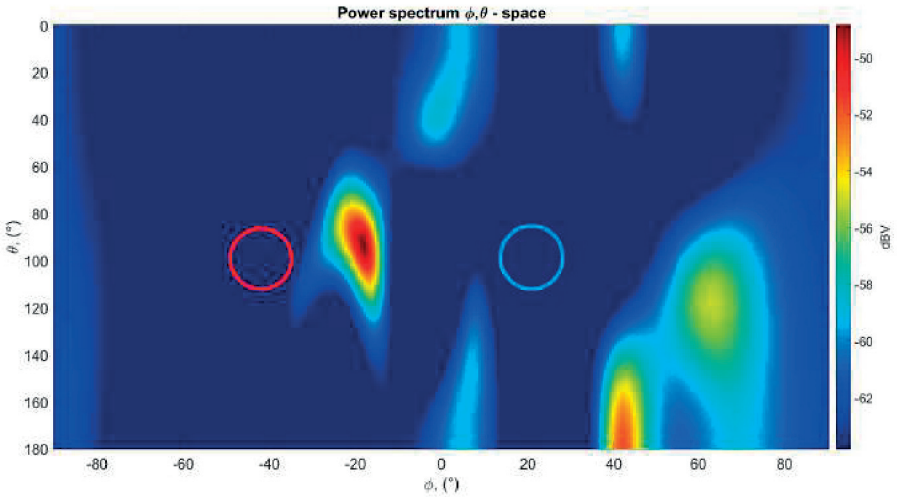

Figure 8.17: Pseudo power spectrum of the MUSIC algorithm.

Results with the 4×4 Rhomboid Array Configuration

Figures 8.18-8.20 shows the results obtained with 4×4 rhomboid configuration for test scenario two. The position of the first reflector is marked with a red circle and the position of the second reflector is marked with a blue circle.

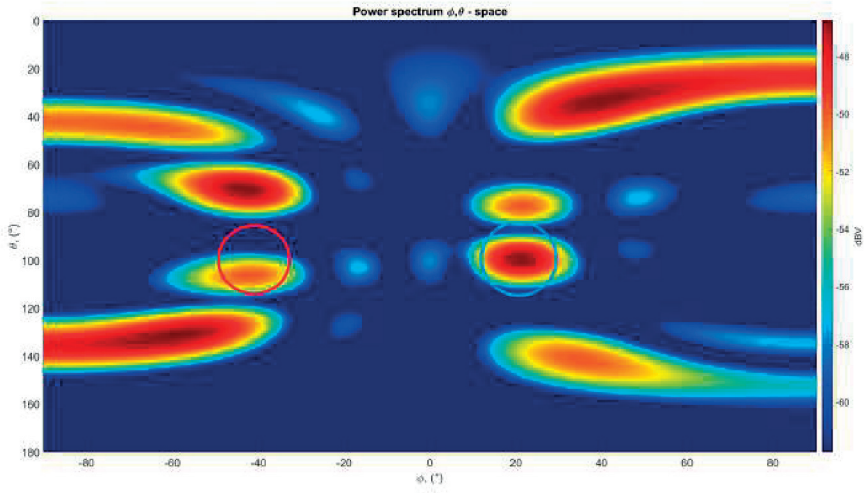

Figure 8.18: Power spectrum of the Sum-and-Delay beamformer.

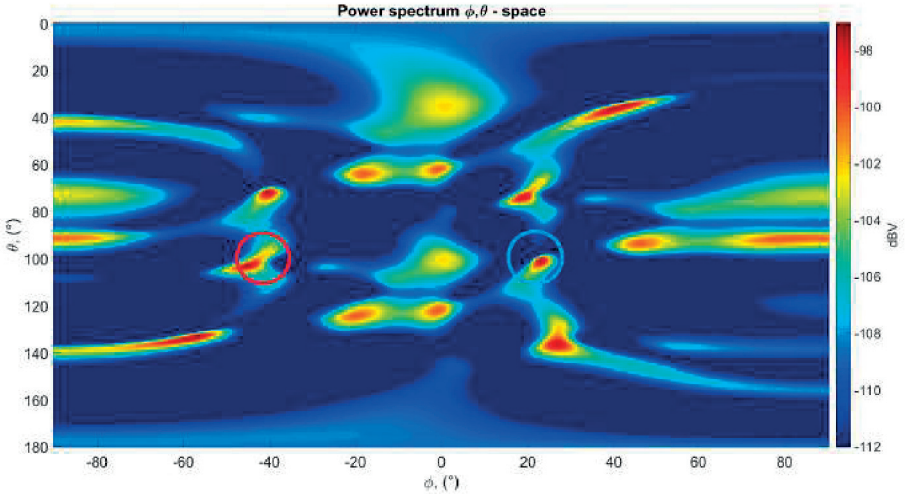

Figure 8.19: Pseudo power spectrum of the Capon/MVDR algorithm.

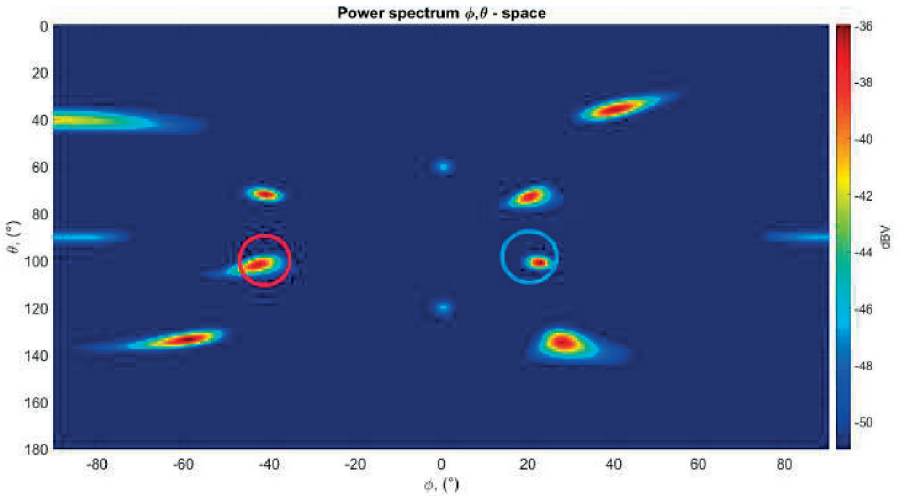

Figure 8.20: Pseudo power spectrum of the MUSIC algorithm.

Chapter 9
Discussion

This chapter presents a discussion of the simulation results, the measurement results and the effectiveness of the Direction-of-Arrival algorithms. The discussion goes through the strengths and weaknesses of the thesis work and aims to explain the differences between the simulation results and the actual measurement results. The chapter starts with Sec. 9.1 explaining the results from the CST simulation, followed by Sec. 9.2 with a discussion of the measurement results and a comparison with the simulation results. Finally, Sec. 9.3 describes the test scenario results obtained from the different DOA-algorithms.

9.1 Simulation Results

The aim was to create a patch antenna that radiates around the frequency $f = 24$ GHz, and from Figures 7.14 and 7.17 it can be seen that this is achieved successfully in the simulations. Both the single patch antenna and the patch antenna array radiates around the correct frequency with a reflection coefficient well below -10 dB, which is desirable. The single patch antenna has a much lower reflection coefficient ($S_{11} \approx$ -40.6 dB) than the antenna array ($S_{11} \approx$ -22.6 dB) and hence it radiates more power around its operating frequency (assuming similar radiation efficiency).

Both the single patch antenna and the antenna array have bandwidths of around 1 GHz, with the single patch antenna having a slightly smaller bandwidth than the array. Their fractional bandwidths, which are less than 20 %, shows that they are both narrowband antenna designs.

The impedance parameters are important when designing a patch antenna since it gives information on how to model the antenna system. The impedance consists of a real part and an imaginary part, $Z = R+jX$, where the real part is the resistance and the imaginary part is the reactance. The real part at the operating frequency shows which impedance transform one has to perform when designing the feeding network, in order to achieve maximum power transfer. A positive reactance means the antenna has inductive reactance and a negative reactance means the antenna has capacitive reactance. The most desirable solution is to have zero reactance $X = 0$ and a resistance of $R = 50\ \Omega$, since most standard RF cables have an impedance of 50 Ω. Figures 7.15 and 7.18 show that the real part of the impedance is around 105 Ω for the single patch antenna and around 58.8 Ω for

the antenna array at their respective operating frequencies. This was considered when designing the feeding network to ensure good impedance matching. In both cases the imaginary part of the impedance is negative and close to zero, thus showing a capacitive behaviour.

Since antenna elements will affect each other in antenna arrays, it is important to have low crosstalk between them in order to ensure good performance. Figure 7.19 shows that the crosstalk between two $\lambda/2$-spaced elements in the antenna arrays is around -29.2 dB for the operating frequency. For our applications, this is quite a good value and the crosstalk is low enough to ensure stable performance. In other applications, such as for phased arrays, the requirement can be much higher.

Figures 7.16 and 7.21 shows that the directivity for the patch antenna is 7.14 dBi and 11.8 dBi for the antenna array, respectively. The directivity for a patch antenna is usually between 5-8 dBi and for a 4×1 linear patch antenna array it should be around 11-14 dBi. The simulations seem to give accurate results.

9.2 Measurement Results

The connectors that were used for the antennas were ordinary SMA connectors, which were not optimized for 24 GHz frequency applications. The reason for this was that connectors that are suited for operation at 24 GHz are very expensive. Since many as 30 cables connectors were required, it was important to choose a cheaper alternative. The differences between the regular and the higher frequency connectors is in the insertion loss. Since the main aim for this prototype was to test the different DOA-algorithms, the extra power loss only contributed to a smaller maximum range, which should not affect the testing capability. A more important aspect is that the Tx feed lines should be of same length in order to get the correct phase information for the DOA-algorithms. Even if most of phase problems could be fixed by a calibration, the equal length made the calibration easier and more precise.

The measurement of the S-parameters, presented in Figure 8.4, resulted in three resonant frequencies rather than one. There can be many reasons for why this would occur. As mentioned before, the microstrip line did not end in the via and the last 0.1 millimeters had to be connected by soldering. This solution was not optimal and affects the impedance matching in the feeding network, which can be the cause for the multiple resonant frequencies. However, all the resonances are close to the operating frequency of 24 GHz and from Figure 8.4 it can be seen that the antennas reflect the least around this frequency, which is desired.

Figure 8.5 shows that the measured crosstalk between two $\lambda/2$-spaced elements in an antenna array is -27.7 dB at the smallest reflecting frequency $f = 24.1$ GHz, which is low enough to ensure good performance. Taking into account the problem of multiple resonances in the measured S11, the measured results appear to agree reasonably well with the simulated results.

9.3 Direction-of-Arrival Algorithms

The ultimate goal of this thesis was to test the performance of the DOA-algorithms based on the different configurations in order to verify the effects of the array patterns simulated in Sec. 6.1. Due to the lack of time, only two of the three antenna configurations were tested.

The first observation was that the 2×8 array was more sensitive to errors in the calibration, which caused the calibration to be recalculated several times to get the algorithms to work with the virtual array. The 4×4 array did not suffer to the same extent from these problems.

The algorithms seem to work very well for the 2×8 rhomboid array in the first test scenario, as seen in Figures 8.8-8.10; the results are accurate with the correct (ϕ, θ) angles identified in the spectrum and the methods seem to be working as intended. Likewise, the results for the 4×4 array, as seen in Figures 8.11-8.13. However, from the figures it can be seen that some false targets appear for the 4×4 array. For test scenario two with the 2×8 array, the Sum-and-Delay beamformer works well, which can be seen in Figure 8.15, but the Capon/MVDR and MUSIC methods fail as shown in Figure 8.16 and Figure 8.17. These two methods seem to provide quite inaccurate results, which can be due to an incorrect implementation. Errors could also arise from bad calibration in combination with distortions. For example, the received baseband signal was observed to be distorted during a part of the measurements; but without changing anything, just redoing the test seemed to have fixed the problem. In the case of the 4×4 array in test scenario two, seen in Figures 8.18-8.20, all three methods seem to work well, however, false targets appear once more.

The methods that involve the estimation of covariance matrix suffered from lack of robustness. When filtering was insufficient, which was the case when only a high pass filter or no filter was used, the covariance matrix was severly distorted and large errors occurred in the DOA-estimation. Since the Capon/MVDR algorithm is less sensitive to modeling errors, it is not as heavily affected as the MUSIC algorithm. Another problem is that Capon/MVDR and MUSIC algorithms are sensitive to coherent signals arising multipath propagation (for example, ground reflection). The low number of antennas can also be the reason why the artifacts occur since the DOFs are too few to be used effectively. Also, the crosstalk in the model is assumed to be zero, however, in reality it is not the case, as shown by the measured results in Figure 8.5.

The performance trade-offs between the different array configurations in the test scenario are clearly visible; higher resolution with false targets appearing in the grating lobes versus low resolution with no false targets (grating lobes). The resolution is poor in the 2×8 array, where the spectrum peak is smeared out. On the other hand, the 4×4 array has well performing resolution (more distinct and narrow peak). Nevertheless, in the case of the 4×4 array, the results are confusing due to the grating lobes giving false detections. The spectrum gives a total of eight hits in scenario two, when the actual number of targets is two, and as explained before this is due to the problem of ambiguity in the array factor.

9.3.1 Implementation of MIMO

The original goal of MIMO as described in Sec. 5.2, was to run TDMA in real time. This means that the switching between the two Tx-antennas takes place after each fast chirp, thus enabling real time MIMO measurements where the Doppler-shift also can be observed. Due to incorrectly working software for the frontend-board, this was not possible. The MIMO operation had to instead be conducted in time series; first a number of frames with fast chirps was sent by the first Tx antenna and received for a couple of seconds followed by the same measurement for the other Tx-antenna. The results can then be processed to synthesize a complete virtual array (with both real and virtual elements) for DOA-estimation. This approach limited our test cases to stationary scenes. The achieved results are good considering the many sources of errors present in the system. Several errors were present, such as the connectors being not specified for use at this frequency, which could introduce phase errors (apart from increased and uneven attenuation). The soldering and the not optimized antenna connections causes the S_{11}-parameter to be noisy, which can be seen in Figure 8.4. The different attenuation and phase between the TX-channels can be calibrated afterwords, making the design more tolerant to imperfections in the DOA-estimation. Finally, the antenna board was found to be not completely flat-surfaced and that is, together with the crude calibration, recognized to be the main error sources in the DOA-estimation.

9.3.2 Covariance Matrix Estimation Problems and Implications

This problem arises since the model used assumes that the signals in the baseband are the incoming signals, which is not always the case. The first step was to remove the low frequency noise shown in Figure 5.6. When doing testing with the manufactured array, it was seen that this step was not enough. Since all signals that are not originating from the same distance do not need to be considered, this insight needs to be somehow accounted for. In the processing of results, this was done by using a Butterworth bandpass filter, which filtered out all signals except the ones contained in the range bin of interest. However, this procedure distorts the power spectrum, thus the spectrum is called a pseudo power spectrum. The Capon/MVDR method seems to show the ground signal reflection to a greater extent, which can be seen in Figure 8.19 and Figure 8.20. However, this bandpass filtering approach is not a very efficient method and it only worked because the target scene was known in advance. For usage in an unknown scenario, this method needs to be improved. In the case of the MUSIC algorithm, the eigenvalues that contain the signal need to be estimated. It was found that the number of signals assumed should be larger than the number of targets in the test scenario, in order to achieve better estimation performance. In the results section, the number of eigenvalues that were assumed to be signals were iterated by how closely the estimated DOA(s) represent the actual test scenario.

Chapter 10
Conclusions

In this work, a two dimensional patch antenna array was designed for use with a FMCW-radar that implements MIMO operation for virtual array formation. The intended application of the radar system is people and traffic detection and measurement. To get the angular information of a target, different Direction-of-Arrival (DOA) algorithms were implemented and their performances were analyzed in two different scenarios for both accuracy and resolution capabilities. The evaluation was done on a custom-designed microstrip patch antenna array powered by a radar-frontend evaluation board. The measurements were successful and the implemented algorithms worked, though the ones using information from the covariance matrix, the Capon/MVDR and MUSIC algorithms, were found to be unreliable and need to be investigated further to be useful in a radar system. The conventional Sum-and-Delay beamformer performed very well, though for better resolution between two separate targets in close proximity of each other, a larger array than the 2x8 proposed in Figure 6.9 (with close enough spacing between the antenna array elements to remove the grating lobes, unlike the 4×4 array) could be implemented for better performance.

To conclude, using FMCW-radar for monitoring people and traffic can be done according to our tests, if the necessary tracking and target counting algorithms are added in combination with an array configuration with no grating lobe and high enough resolution.

Chapter 11
Further Work

The estimation of the covariance matrix can be improved by several methods to boost the performance of the Capon/MVDR and MUSIC algorithms. The information contained in the covariance matrix can be better structured by performing preprocessing schemes, which are often implemented when these methods are used. Two common ones are *spatial smoothing* and *backward-forward averaging*. In addition, the use of MUSIC and subspace algorithms require the number of signals to be known. In practice, the number of signals need to be estimated by another algorithm, e.g. via Akaike Information Criterion (AIC). The question is if these methods can be implemented, considering that the system should be low cost, easy to calibrate and integrated into a single chip. These are interesting topics that could be further investigated.

One other topic that can be investigated is if the array can be optimized to reduce the number of elements. This can be done by investigating the number of antennas that are needed to get an acceptable resolution in real scenarios as well as making the antennas more integrated with the output and input stages of the frontend, in order to lower the attenuation in the RF-chain.

Since MIMO operation could not be implemented as intended, Doppler measurements could not be conducted. Since Doppler measurements contain information of the speed of the measured targets, this could not be measured. This speed information can be exploited to filter out the stationary clutter by performing mean value subtraction. All stationary targets do not have the low frequency Doppler-shift, which means that the mean value is constant for each chirp for the entire chirp repetition interval. Removing the mean value will remove the signal from stationary targets, since it should be relatively constant in all chirps. The mean value subtraction will increase the SNR when there is a high amount of static clutter in the target scene, especially when measuring indoors. The drawback is that the stationary targets can not be seen, but to measure people and traffic, only moving target are usually of interest. This can be a interesting topic for further studies.

Some kind of tracking algorithm also needs to be implemented in order to to filter out hits from the background of noise, clutter and interference. One example is the Constant False Alarm Rate (CFAR) algorithm, which is a common form of adaptive algorithm used in radar systems. In addition to this, a tracking algorithm used to count and track people needs to be developed, if a full working product is to be considered.

References

[1] Applied Electronics Engineering. 2013. *Design of Microstrip antenna in CST microwave Studio*. [Online]. Available from: http://appliedelectronicsengineering.blogspot.se/2013/08/design-of-microstrip-antenna-in-cst.html [Accessed 2016-04-26]

[2] Balanis, C.A. 2005. *Antenna Theory: Analysis and Design*. 3rd ed. New Jersey: Wiley

[3] Bevelacqua, P.J. *Fractional Bandwidth (FBW)*. [Online]. Available from: http://www.antenna-theory.com/definitions/fractionalBW.php [Accessed 2016-06-01]

[4] Budge, M.C. and German, S.R. 2015. *Basic Radar Analysis*. Norwood: Artech House

[5] Capon, J. 1969. High resolution frequency-wavenumber spectrum analysis. *Proceedings of the IEEE*. [Online]. Vol. 57, No. 8, pp. 1408–1418. Available from: http://ieeexplore.ieee.org/xpl/login.jsp?tp=&arnumber=1449208&url=http%3A%2F%2Fieeexplore.ieee.org%2Fxpls%2Fabs_all.jsp%3Farnumber%3D1449208 [Accessed 2016-06-01]

[6] Charvat, G.L. 2014. *Small and short-range radar systems*. Boca Raton: CRC Press

[7] Chen, Z., Gokeda, G. and Yu, Y. 2010. *Introduction to Direction-of-Arrival Estimation*. Norwood: Artech House

[8] Computer Simulation Technology AG. 2016. *CST STUDIO SUITE*. [Online]. Available from: https://www.cst.com/Products/CSTS2 [Accessed 2016-04-26]

[9] Fang, D.G. 2009. *Antenna Theory and Microstrip Antennas*. Boca Raton: CRC Press

[10] Harter, M., Mahler, T., Schipper, T., Ziroff, A. and Zwick, T. 2013. *2-D antenna array geometries for MIMO radar imaging by Digital Beamforming*. [Online]. 2013 European Radar Conference (EuRAD), 9-11 October 2013, Nuremberg. pp. 383-386.

[11] Heinzel, G., Rüdiger, A. and Schilling, R. 2002. *Spectrum and spectral density estimation by the Discrete Fourier transform (DFT), including a comprehensive list of window functions and some new flat-top windows.* [Online]. Max-Planck-Institut für Gravitationsphysik (Albert-Einstein-Institut). Available from: `https://holometer.fnal.gov/GH_FFT.pdf` [Accessed 2016-05-23]

[12] Inras GmbH. 2015. *ADF-24G-TX2RX8-D03 Frontend (Preliminary User Manual).* Linz

[13] International Telecommunication Union. 2012. *ITU Radio Regulations, CHAPTER II – Frequencies, ARTICLE 5 Frequency allocations, Section IV – Table of Frequency Allocations.* [Online]. Available from: `http://www.itu.int/dms_pub/itu-s/oth/02/02/S02020000244501PDFE.PDF` [Accessed 2016-06-28]

[14] Krim, H. and Viberg, M. 1996. Two Decades of Array Signal Processing Research. *IEEE Signal Processing Magazine.* [Online]. Vol 13, No. 4, pp. 67-94.

[15] Li, J. and Stoica, P. 2009. *MIMO Radar Signal Processing.* New Jersey: Wiley

[16] National Aeronautics and Space Administration. 2016. *Deep Space Network (DSN).* [Online]. Available from: `http://www.nasa.gov/directorates/heo/scan/services/networks/txt_dsn.html` [Accessed 2016-06-26]

[17] Orfanidis, S.J. 2014. *Electromagnetic Waves and Antennas.* [Online]. New Jersey: Rutgers University. Available from: `http://www.ece.rutgers.edu/~orfanidi/ewa/` [Accessed 2016-06-01]

[18] Otto, T. *Principle of FMCW radar* [Online]. Available from: `http://www.slideshare.net/tobiasotto/principle-of-fmcw-radars` [Accessed 2016-06-01]

[19] Ridenour, L.N. 1947. *Radar System Engineering.* [Online]. New York: McGraw-Hill. Available from: `https://www.jlab.org/ir/MITSeries/V1-1.pdf` [Accessed 2016-05-09]

[20] Schmidt, R. 1986. Multiple Emitter Location and Signal Parameter Estimation. *IEEE Transactions on Antennas.* [Online]. Vol. 34, No. 3, pp. 276-280.

[21] Trees, H.L.V. 2002. *Optimum Array Processing: Part IV of Detection, Estimation and Modulation Theory.* Wiley-Interscience

[22] Wolff, C. *Radar Basics.* [Online]. Available from: `http://www.radartutorial.eu/index.en.html` [Accessed 2016-06-01]

LUND
UNIVERSITY

Series of Master's theses
Department of Electrical and Information Technology
LU/LTH-EIT 2016-531

http://www.eit.lth.se